Hydrodynamical simulations of the Galactic Center cloud G2 as an outflow

Alessandro Ballone

München 2016

Hydrodynamical simulations of the Galactic Center cloud G2 as an outflow

Alessandro Ballone

Dissertation
an der Fakultät für Physik
der Ludwig–Maximilians–Universität
München

vorgelegt von
Alessandro Ballone
aus Pescara, Italien

München, den 27.10.2016

Erstgutachter: Prof. Dr. Andreas Burkert
Zweitgutachter: Prof. Dr. Reinhard Genzel
Tag der mündlichen Prüfung: 16.12.2016

The scientist has a lot of experience with ignorance and doubt and uncertainty, and this experience is of very great importance, I think. When a scientist does not know the answer to a problem, he is ignorant. When he has a hunch as to what the result is, he is uncertain. And when he is pretty damn sure of what the result is going to be, he is still in some doubt. We have found it of paramount importance that in order to progress, we must recognize our ignorance and leave room for doubt. Scientific knowledge is a body of statements of varying degrees of certainty - some most unsure, some nearly sure, but none absolutely certain. Now, we scientists are used to this, and we take it for granted that it is perfectly consistent to be unsure, that it is possible to live and not know. But I dont know whether everyone realizes this is true. Our freedom to doubt was born out of a struggle against authority in the early days of science. It was a very deep and strong struggle: permit us to question - to doubt - to not be sure. I think that it is important that we do not forget this struggle and thus perhaps lose what we have gained.

Richard Feynman - "What Do You Care What Other People Think?"

[...] The early developmental stages of most sciences have been characterized by continual competition between a number of distinct views of nature, each partially derived from, and all roughly compatible with, the dictates of scientific observation and method. What differentiated these various schools was not one or another failure of method - they were all "scientific" - but what we shall come to call their incommensurable ways of seeing the world and of practicing science in it. Observation and experience can and must drastically restrict the range of admissible scientific belief, else there would be no science. But they cannot alone determine a particular body of such belief. An apparently arbitrary element, compounded of personal and historical accident, is always a formative ingredient of the beliefs espoused by a given scientific community at a given time.

Thomas Kuhn - "The Structure of Scientific Revolutions"

Contents

List of Figures

List of Tables

Zusammenfassung

Die Entdeckung der kleinen Gas- und Staubwolke G2 (Gillessen et al., 2012) in einem Abstand von wenigen Lichtmonaten vom Zentrum unserer Galaxie faszinierte von Anfang an viele Astronomen. Das innere Parsek des Galaktischen Zentrums beherbergt einen sehr dichten und jungen Sternhaufen, ein aus verschiedenen Phasen aufgebautes interstellares Medium und ein Schwarzes Loch mit einer Masse von mehreren Millionen Sonnenmassen. Als nächster Galaktischer Kern, stellt dieser ein einzigartiges Laboratorium dar um Massenakkretion auf Schwarze Löcher und Gasphysik unter sehr extremen Bedingungen zu studieren. Obwohl die letzten Jahrzehnte ein sehr detailliertes Bild des Galaktischen Zentrums und seiner Eigenschaften hervorgebracht haben, wird die Studie der zeitlichen Entwicklung der G2-Wolke als wichtiges Werkzeug angesehen, um viele unbekannte Parameter besser einzuschränken. Viele Modelle haben sich in den letzten Jahren diesem Ziel verschrieben und die Wolke selbst hat im Jahre 2014 ihr Perizentrum durchlaufen. Das Wesen dieses kleinen und faszinierenden Objektes ist hingegen weiterhin unklar. Zwei Modellklassen erscheinen möglich: G2 könnte einfach ein diffuser Gas- und Staubklumpen sein oder G2 könnte mit einem zentralen (evtl. stellaren) Objekt verknüpft sein.

Diese Dissertation konzentriert sich auf die zweite Möglichkeit. Dem Vorschlag von Murray-Clay & Loeb (2012) folgend könnte die Gaskomponente von G2 das Material im Ausfluss einer kompakten Quelle sein, die sich auf der beobachteten Bahn bewegt. Viele andere Studien haben sich ebenfalls auf diese Möglichkeit konzentriert und versucht die Eigenschaften von G2 mittels einfacher analytischer Berechnungen zu erklären. Viele dieser Abschätzungen vernachlässigen jedoch den Einfluss des externen, heißen Materials – welches auf das zentrale Schwarze Loch akkretiert wird – auf die Entwicklung von G2. Unser Ziel ist es die Hydrodynamische Entwicklung eines solchen Szenarios mit Hilfe des Gittercodes PLUTO (Mignone et al., 2007, 2012) zu überprüfen.

Eine erste eindimensionale Studie zeigte bereits, dass sich die Struktur des Ausflusses im zentralen Parsek der Galaxie von stellaren Winden unter typischen galaktischen Bedingungen unterscheidet. Der hohe Druck des umgebenden Akkretionsflusses begrenzt jeden Ausfluss stark (in diesem Szenario hat dies einen großen Einfluss auf die Größe von G2) und führt zu einer dünnen, dichten und effizient kühlenden Schale geschockten Gases (statt einer großen Blase heißen Plasmas).

Dieser vereinfachte Zugang ebnete den Weg für eine zweidimensionale hydrodynamische Studie in zylindrischen Koordinaten, welche viele zusätzliche (nicht-lineare) Prozesse berücksichtigt, die für die Entwicklung von G2 wichtig sind. Diese beinhalten ihre Ke-

plerbewegung auf einer sehr exzentrischen Bahn, die Dehnung aufgrund der Gezeitenwechselwirkung mit dem massereichen Schwarzen Loch, die Ausbildung von Rayleigh-Taylor-Instabilitäten und den Gasverlust aufgrund von Wechselwirkung mit dem Staudruck des umgebenden Mediums. In einem ersten Vergleich mit den beobachteten Eigenschaften der Gaskomponente von G2 fanden wir heraus, dass der Ausfluss eine relativ hohe Massenverlustrate ($\dot{M}_{\rm w} \approx 10^{-7} {\rm M}_{\odot}\ {\rm yr}^{-1}$) und niedrige Geschwindigkeit ($v_{\rm w} = 50\ {\rm km\,s^{-1}}$) aufweisen muss, wie man sie typischerweise bei jungen stellaren Objekten wie T Tauri Sternen findet (wie bereits von Scoville & Burkert, 2013 vorgeschlagen).

Dieses Resultat wurde durch 3D AMR (Adaptive Mesh Refinement) Simulationen bestätigt (mit einigen Unterschieden), welche auch einen realistischeren Vergleich mit Beobachtungen ermöglichen. Dies wird durch die Berechnung von simulierten Positions-Geschwindigkeits(PV)-Diagrammen mittels der Brackett-γ Rekombinationslinie realisiert (vergleichbar derer in Gillessen et al., 2012, 2013a,b; Pfuhl et al., 2015). Durch einen derartigen Vergleich mit PV-Diagrammen konnte auch gezeigt werden, dass ein gleich massereicher, aber schnellerer ($v_{\rm w} = 400\ {\rm km\,s^{-1}}$) Ausfluss prinzipiell G2 und das nachfolgende Gas (oftmals als der Schweif von G2 oder "G2t" bezeichnet) beschreiben kann. Eine "kompakte Quelle" in Form eines T Tauri Sternes hätte auch den Vorteil die beobachtete Kompaktheit der Staubkomponente von G2 zu erklären, welche im Widerspruch zur ausgedehnten Gaskomponente steht.

Eine Studie des Szenarios einer diffusen Wolke durch Schartmann et al. (2015) zeigt eine ähnlich gute Übereinstimmung mit den beobachteten PV-Diagrammen. Unsere 3D Simulationen sagen jedoch voraus, dass sich in unserem Szenario rund 5-10 Jahre nach dem Perizentrumsdurchgang die Quelle von dem zuvor ausgeworfenen Gas entkoppeln wird und eine "frische" G2-Wolke um die staubige Komponente herum bilden sollte. Dies könnte sich als der unwiderlegbare Beweis entpuppen, um das Rätsel der G2-Wolke zu lösen.

Abstract

The discovery of the little gas and dust cloud G2 (Gillessen et al., 2012) at few light months from the center of our Galaxy has, from the very beginning, caught the attention of the astronomical community. The inner parsec of the Galactic Center hosts, in fact, a very dense and young stellar cluster, a rich multiphase insterstellar medium and a supermassive black hole of few million solar masses. Being the closest galactic nucleus, this makes it a unique laboratory to study accretion onto black holes and gas physics under very extreme conditions. Although the last decades have revealed more and more details about the Galactic Center and its properties, the monitoring and study of G2's evolution and origin has thus been recognized as a very powerful tool to shed light on many of the current unknowns. Many models have focused on this task, in the last years, and meanwhile G2 has reached its pericenter in year 2014. Nonetheless, the nature of this little and fascinating object is still uncertain. A main dichotomy can be marked: G2 might simply be a diffuse clump of gas and dust or it might be related to a central (possibly stellar) object.

The work presented in this dissertation focuses on the second possibility. Following the original suggestion by Murray-Clay & Loeb (2012), G2's gaseous component could be the material outflowing from a compact source moving on the observed orbit. Several other studies have focused on this possibility, trying to explain G2's properties by means of simple analytical estimates. Many of these estimates neglect the impact of the external hot material - accreting onto the central supermassive black hole - on G2's evolution. Our goal is to test the hydrodynamics of such a scenario through simulations with the grid code PLUTO (Mignone et al., 2007, 2012).

A first preliminary set of one-dimensional simulations already showed that the structure of outflows in the central parsec of the Galaxy is different from the one of stellar winds in typical galactic conditions. The high pressure of the surrounding accretion flow is strongly confining any outflow (in this scenario, this has a strong impact on the size of G2) and shocking it in a very thin, dense and efficiently cooling shell (rather than in a large bubble of hot plasma).

This simplified approach was fundamental to guide us to first attempt a study, by means of numerical hydrodynamics with 2D cylindrical coordinates, of many of the other (non linear) processes involved in G2's evolution. These include its keplerian motion on a very eccentric orbit, its stretching by the gravitational tidal field of the supermassive black hole, the formation of Rayleigh-Taylor instabilities and their ram pressure stripping. In a first comparison with the observed properties of the gas component of G2, we found

that the outflow must have relatively high mass loss rates ($\dot{M}_{\rm w} \approx 10^{-7} {\rm M}_{\odot}\ {\rm yr}^{-1}$) and low velocities ($v_{\rm w} = 50\ {\rm km\,s}^{-1}$), typical of low-mass young stellar objects such as T Tauri stars (as already suggested by Scoville & Burkert, 2013).

This finding has been successively confirmed (though with some discrepancies) by 3D adaptive-mesh-refinement simulations, which also allowed a more realistic comparison to the observations, through the construction of mock position-velocity (PV) diagrams for the Brackett-γ recombination line emission (as those in Gillessen et al., 2012, 2013a,b; Pfuhl et al., 2015). Comparison to position-velocity diagrams has also showed that an equally massive but faster ($v_{\rm w} = 400\ {\rm km\,s}^{-1}$) outflow could, in principle, be able to simultaneously reproduce G2 and the gas following it on the same orbit (often called G2's "tail" or "G2t"). A "compact source" being a young and dusty T Tauri might also have the advantage of explaining the observed compactness of G2's dust component, as opposed to its extended gaseous one.

A study of the diffuse cloud scenario by Schartmann et al. (2015) can produce a similarly good comparison to the observed PV diagrams. However, our 3D simulations show that, in our scenario, in 5-10 years after pericenter the source decouples from the previously emitted gas and a new and "fresh" G2 should reform around the dusty one, later on. This might be the smoking gun needed to solve G2's puzzle.

Chapter 1

Introduction: The inner pc of our Galaxy

Being by far the closest galactic nucleus to the Earth, the center of the Milky Way offers a unique opportunity to test astrophysics in extreme conditions. In particular, the inner pc of the Galactic Center hosts a supermassive black hole (SMBH), a very young and dense stellar cluster with very peculiar properties and a widely variegated interstellar medium (ISM). In this Chapter every section will be dedicated to one of these constituents, in a sort of "zoom-in" towards the central SMBH.

1.1 The ISM: cold, warm and hot gas

The inner few parsecs of the Galaxy show a multicomponent ISM, including cold atomic and molecular gas, ionized gas with temperature of roughly 10^4 K and extremely hot (probably highly magnetized) ionized plasma. We will briefly describe these different components in the present section.

1.1.1 Cold gas: the circumnuclear disk/ring

The inner parsec is surrounded by a ring of clumpy molecular/neutral gas and dust visible in mm/submm and infrared ($\approx 0.75 - 300$ μm), often called "circumnuclear disk/ring" (CND/CNR; e.g., Gatley et al., 1986; Guesten et al., 1987; Jackson et al., 1993; Marr et al., 1993; Vollmer & Duschl, 2002; Shukla et al., 2004; Christopher et al., 2005; Montero-Castaño et al., 2009; Martín et al., 2012; Tsuboi et al., 2016; Moser et al., 2016). The CND extends up to few pc from SgrA*, but its inner edge is around 1.5 pc, hence it encloses the region this Chapter is dedicated to (see Fig. 1.1). Its mass is very uncertain and ranges from 10^4 $M_\odot$ (Mezger et al., 1989; Liu et al., 2013) to few $10^5 - 10^6$ $M_\odot$ (Christopher et al., 2005; Oka et al., 2011). Kinematically, the CND shows an overall circular rotation of ≈ 100 km s^{-1} (e.g., Marr et al., 1993; Christopher et al., 2005; Martín et al., 2012), but it is highly disturbed, showing holes and local indications of streamers from outside

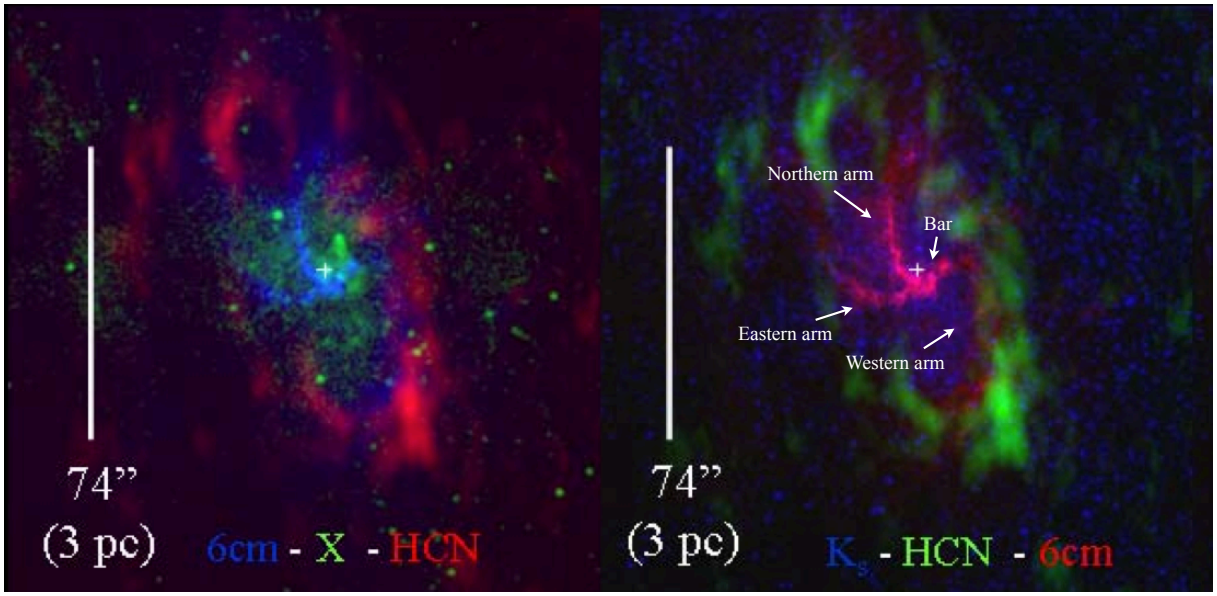

Figure 1.1: Multiwavelength image of the inner few parsecs of our Galaxy. Left: Color composite of the radio 6 cm (blue), HCN 1-0 rotational line ($\approx$ 3.385 mm, red) and X-ray emission (green). Right: 6 cm radio (red), K band ($\approx$ 2.2 μm, blue) and HCN 1-0 emission. In both panels, the white cross marks the position of SgrA*. In this plot, the HCN line is tracing the position of the molecular CND (Sec. 1.1.1), the radio emission is tracing the position of the minispiral (Sec. 1.1.2), the X-ray emission is tracing the hot plasma at temperatures $> 10^7$ K (Sec. 1.1.3) and the K band emission is mainly tracing the stars (Sec. 1.2). The figure has been adapted from Genzel et al. (2010).

and towards the inside (e.g., Christopher et al., 2005; Montero-Castaño et al., 2009; Oka et al., 2011; Martín et al., 2012; Liu et al., 2012, 2013). Hence, the CND might be feeding SgrA*, perhaps through the inner minispiral that seems to be associated to it (see Sec. 1.1.2). Given the latter indications and the uncertainties in its mass, it is not clear whether the CND is a stable (and potentially star forming) or transient structure (e.g., Morris & Serabyn, 1996; Yusef-Zadeh et al., 2008; Montero-Castaño et al., 2009; Oka et al., 2011; Liu et al., 2012; Requena-Torres et al., 2012).

In addition to the CND, more than 300 $M_\odot$ of atomic gas could exist inside the CND (e.g., Jackson et al., 1993; Goicoechea et al., 2013). Few $M_\odot$ of dust are also detected (e.g., Davidson et al., 1992; Kunneriath et al., 2012; Tsuboi et al., 2016) and are mainly associated to the minispiral (Sec. 1.1.2) and the young massive stars (Sec. 1.2.1). Detection of SiO and CS clumps with very high velocities also suggest the possibility of ongoing star formation at distances smaller than the inner edge of the CND (Yusef-Zadeh et al., 2013; Moser et al., 2016).

1.1.2 Warm ionized gas: the minispiral

Few tens $M_\odot$ of ionized gas are present inside the CND (Sec. 1.1.1), in clumpy filaments/arms observable in radio and infrared continuum and emission lines (see Fig. 1.1). These structures are referred to as the "minispiral" (e.g., Lo & Claussen, 1983; Ekers et al., 1983; Serabyn & Lacy, 1985; Roberts et al., 1996; Vollmer & Duschl, 2002; Paumard et al., 2004; Zhao et al., 2009, 2010; Irons et al., 2012; Kunneriath et al., 2012; Tsuboi et al., 2016; Moser et al., 2016). The minispiral shows three main arms, namely the Western, Eastern and Northern arms. In particular, the Western arm is believed to be the inner edge of the CND (Montero-Castaño et al., 2009; Zhao et al., 2009, e.g.,), but the other two arms also seem to lie in the same plane as the CND (e.g., Paumard et al., 2004; Zhao et al., 2009). The kinematics of the Eastern and Northern arms and their elongation towards SgrA* suggest that these two arms are indeed tidally stretched filaments streaming towards the center, possibly colliding in the so-called "bar" feature, as suggested in particular by Zhao et al. (2010) (but see Irons et al., 2012, for a different interpretation). The minispiral has typical densities of the order of 10^4 cm^{-3} and temperatures of roughly 10^4 K (Zhao et al., 2010; Kunneriath et al., 2012; Moser et al., 2016) and it is believed to be ionized by the ultraviolet (UV) photons emitted by the disk(s) of young stars (Sec. 1.2.1, Paumard et al., 2004; Martins et al., 2007; Zhao et al., 2010; Kunneriath et al., 2012).

Most of the minispiral is associated to dust, also observed in mid/far-infrared (MIR/FIR; e.g., Gezari et al., 1985; Lau et al., 2013). The cloud G2, presented in chapter 2 has roughly the same temperature and only one order of magnitude bigger density. Like the minispiral, it has a very radial orbit and it is associated to dust. Hence, there might be a connection between G2 and the minispiral, as suggested by Różańska et al. (2014).

1.1.3 The hot bubble

We will mention in Sec. 1.3.2 that a compact ($\approx$ 0.01 pc) X-ray component corresponds to SgrA* itself; such compact emission shows a significant flaring and it is believed to be directly associated to its hot accretion flow.

In addition to this, a more diffuse component with size of roughly 1 pc is also detected (see Fig. 1.1). This diffuse emission is believed to be mainly thermal and produced by very hot plasma with temperatures $> 10^7$ K and density of the order of 30 cm^{-3} at the Bondi radius, i.e., $\approx$ 0.05 pc (Baganoff et al., 2003; Yuan et al., 2003, however, this estimate is somewhat dependent on the model used to fit the observations). This hot gas might be produced by the shocked stellar winds from the O/WR stars in the disk(s) (Sec. 1.2.1). The latter hypothesis has been tested by several authors and in such a picture the powerful stellar winds are feeding hot gas into the Bondi radius at few 10^{-6} $M_\odot$ yr^{-1}, thus generating the accretion flow solution needed to match the observations of the smallest resolvable scales (e.g., Coker & Melia, 1997; Rockefeller et al., 2004; Quataert, 2004; Cuadra et al., 2006; Mościbrodzka et al., 2006; Xu et al., 2006; Cuadra et al., 2008; Wang et al., 2013; Russell et al., 2016). Such a conclusion is even strengthened by the most recent observations by Wang et al. (2013), showing an asymmetric, disk-like distribution of the central parsec

X-ray gas, aligned with the disk of young stars. However, another possibility is that such extended emission is instead generated by the superposition of compact objects, as maybe suggested by the hard X-ray spectrum, as detected by Chandra and NuSTAR (Muno et al., 2004; Perez et al., 2015).

1.1.4 Magnetic fields

Although magnetic fields have been widely investigated at distances from SgrA* of the order of 100 pc (see, e.g., the reviews from Bicknell & Li, 2001; Morris, 2006; Ferrière, 2009; Morris, 2014), not much can be directly inferred from observations concerning the inner parsec of the Galaxy. Emission models for the synchrotron emission of SgrA* (see Sec. 1.3.2) require magnetic fields of about 30-100 G near the event horizon of SgrA* (e.g., Falcke & Markoff, 2000; Mościbrodzka et al., 2009; Dexter et al., 2010). The lucky discovery of the magnetar[1] PSR J17452900 at about 0.12 pc from SgrA*[2] allowed an estimate of the magnetic field strength in the hot plasma at this distance of $B \approx 10$ mG (Eatough et al., 2013). These estimates are roughly (within approximately 1 order of magnitude) consistent with a magnetic field in equipartition with the thermal and gravitational energy of the hot gas, hence suggesting a relatively ordered magnetic field on large scales. Estimates like the one in Eatough et al. (2013) are assuming that the observed polarization of the radio magnetar emission is produced by Faraday rotation due to material along the line of sight, i.e., the "Faraday screen", and inferring the magnetic fields of the screen by the rotation measure of the polarization vector. However, the rotation measure depends on the combination of the magnetic field and density of the screen, hence these estimates are strongly relying on assumptions or estimates concerning the latter, which always lead to a relatively high degree of uncertainty. Anyway, magnetic fields of this intensity could be important for the evolution of the interstellar medium, particularly of cold gas embedded in the hot plasma (as for the case of G2, see chapter 2), in certain cases reducing the formation of instabilities and the impact of thermal conduction (hence, helping their survival) or decelerating them through an additional magnetic drag force (see Sec. 2.2.1 and, e.g., McCourt et al., 2015).

1.2 The young stars

A nuclear star cluster (NSC) resides at the center of our Galaxy, as in the case of many other galaxies (e.g., Böker et al., 2002; Côté et al., 2006; Graham & Spitler, 2009). The NSC of the Milky Way is mainly composed of old stars (Genzel et al., 2010, and references therein), but the inner parsec is populated by many massive and young stars. We can split

[1] Magnetars are neutron stars, emitting in radio as normal pulsars, but also producing very strong and characteristic X-ray and gamma ray flares due to their extremely strong magnetic field.

[2] Interestingly, the discovery of PSR J1745-2900 was actually triggered by a monitoring of SgrA* by the X-ray telescope SWIFT (http://swift.gsfc.nasa.gov/), to find signals coming from the passage of the cloud G2 (see chapter 2).

the young stars in the inner pc in two main populations: a disk of young stars, with inner edge around 0.05 pc, and the S-stars.

1.2.1 The disk(s) of young stars

More than a hundred young massive stars have been currently detected in the inner parsec of our Galaxy, both with the VLT (Paumard et al., 2006; Bartko et al., 2009) and the Keck Telescope (Lu et al., 2009; Do et al., 2013; Yelda et al., 2014). Most of these stars are classified as O-type (many of them even in a Wolf-Rayet phase) and have an age of few Myr (4-8 Myr: Paumard et al. 2006; 2.5-6 Myr: Do et al. 2013, Lu et al. 2013). These stars have powerful winds (Martins et al., 2006) that can form bow-shocks in their interaction with the surrounding gas (e.g., Tanner et al., 2005; Sanchez-Bermudez et al., 2014; Yusef-Zadeh et al., 2015) and are believed to be responsible for the feeding of SgrA*, at least close to the Bondi radius (see Sec. 1.1.3). When looking at their kinematics, the young

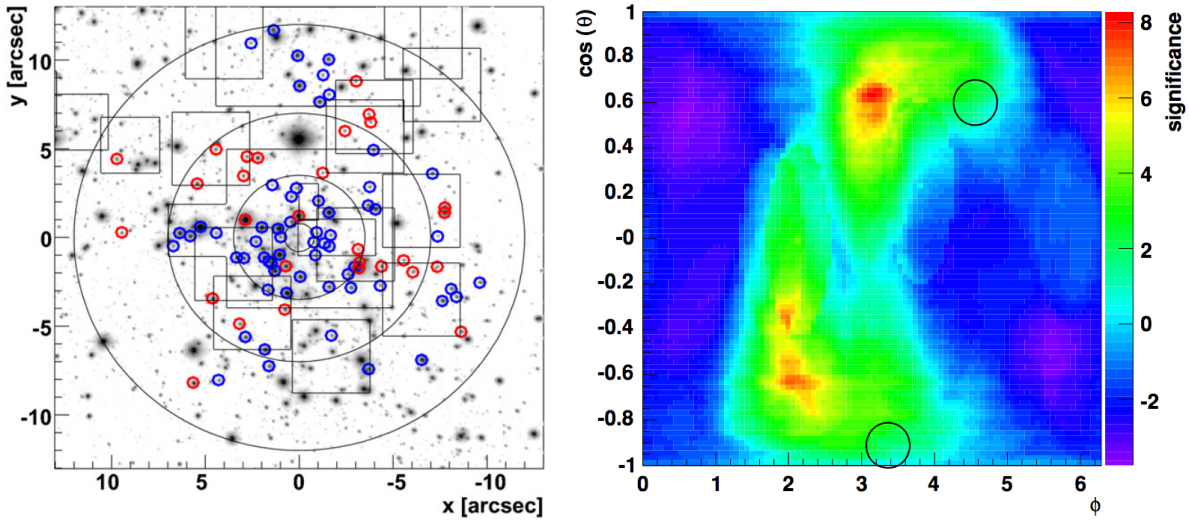

Figure 1.2: The disks of young stars. Left: SINFONI image of the sample of 90 O/WR stars in the inner 0.5 pc (≈ 13 arcsec) of our Galaxy. Blue circles show clockwise orbits, while red circles show counterclockwise orbits. The figure is taken from Bartko et al. (2009). Right: Distribution of orbital normal vectors in the sky for 82 young stars between 3.5 and 15 arcsec from the central supermassive black hole. The sky map is obtained through a cylindrical equal area projection, where the sky "sphere" is parametrized with the usual spherical coordinates θ and ϕ (we refer to Bartko et al., 2009, for the chosen conversion between the orbital elements of the stars and these coordinates). The significance is expressed in standard-deviations of the distribution. The upper right excess shows the stars in the clockwise disk, while the lower left excess represents the stars in the counterclockwise one. The disks positions from Paumard et al. (2006) are shown by the black circles for comparison. The figure is taken from Bartko et al. (2010).

stars show a rotation pattern opposite to the rotation of the Galaxy (Genzel et al., 2000; Tanner et al., 2006; Paumard et al., 2006), initially believed to be consistent with a thin rotating disk (Levin & Beloborodov, 2003). Nowadays, this disk is often referred to as the "clockwise (CW) disk". More sophisticated statistical analysis of the orbital angular momentum distribution by Lu et al. (2009), Bartko et al. (2009), Bartko et al. (2010), Do et al. (2013) and Lu et al. (2013) confirmed this finding, showing that at least half of the young stars lie in the CW disc (though a recent analysis by Yelda et al., 2014, suggest a smaller fraction of 20%), but also that the disk has a significant thickness (opening angle of roughly 10°) and possibly a warp. The single orbits are also close to circular, with eccentricities $e < 0.5$. Some of the previously mentioned studies also suggest the presence of a "counterclockwise (CCW) disk", inclined by roughly 60° with respect to the CW one (see Fig. 1.2, Paumard et al., 2006; Bartko et al., 2009, 2010).

The young age of the disk and indications of a top-heavy initial mass function (Paumard et al., 2006; Bartko et al., 2010; Do et al., 2013; Lu et al., 2013) - suggesting a rapid star formation episode - led to the so-called "paradox of youth". At 1 pc distance from SgrA*, the Roche density is of the order of 10^7 cm^{-3}. This means that any molecular cloud, whose typical densities are below this limit, would be tidally disrupted by the SMBH (but see Shukla et al., 2004; Montero-Castaño et al., 2009). Yet, "standard" dynamical friction is not able to bring such stars from larger distances to the present position, within the lifetime of the disk. The formation of the CW disk remains an open question, with many non-standard processes invoked to explain it: these include fragmentation - by gravitational instability - of an accretion disk around SgrA* (Nayakshin, 2006; Nayakshin et al., 2007), fragmentation of gas streamers by the infalling and disruption of a molecular cloud (Bonnell & Rice, 2008; Mapelli et al., 2008; Hobbs & Nayakshin, 2009; Alig et al., 2011; Mapelli et al., 2012; Lucas et al., 2013; Alig et al., 2013; Trani et al., 2016) or a tidal disruption of an infalling stellar cluster (Gerhard, 2001; McMillan & Portegies Zwart, 2003; Kim et al., 2004; Fujii et al., 2008, 2010). Reviewing these processes is beyond the purpose of this introduction, hence we refer to the recent review by Mapelli & Gualandris (2016).

1.2.2 The S-stars

Inside the inner edge (0.05 pc) of the CW disk, there is a second population of stars, with somewhat different properties, named S-stars (Schödel et al., 2003; Ghez et al., 2003, 2005a; Eisenhauer et al., 2005; Gillessen et al., 2009b). The first, main difference resides in their orbital properties. In particular, Gillessen et al. (2009b) derived orbital solutions for the 28 brightest S-stars and used them to evaluate the mass of the central SMBH (see Sec. 1.3.1): 6 of these have orientations and eccentricities that are compatible with those of the CW disk; 22 are, instead, isotropically distributed (see Fig. 1.3) and have very high eccentricities, $n(e) \propto e^{2.6\pm0.9}$ ($n(e)$ being the probability distribution of finding an S-star with eccentricity e). This means that the eccentricities of the S-star cluster are even larger than those of a two-body relaxed system, with "thermal" distribution $n(e) \propto e$.

Concerning their age, Eisenhauer et al. (2005) showed that the S-stars have spectral properties of B-type stars, hence giving a possible range for their ages of 6-400 Myr. This

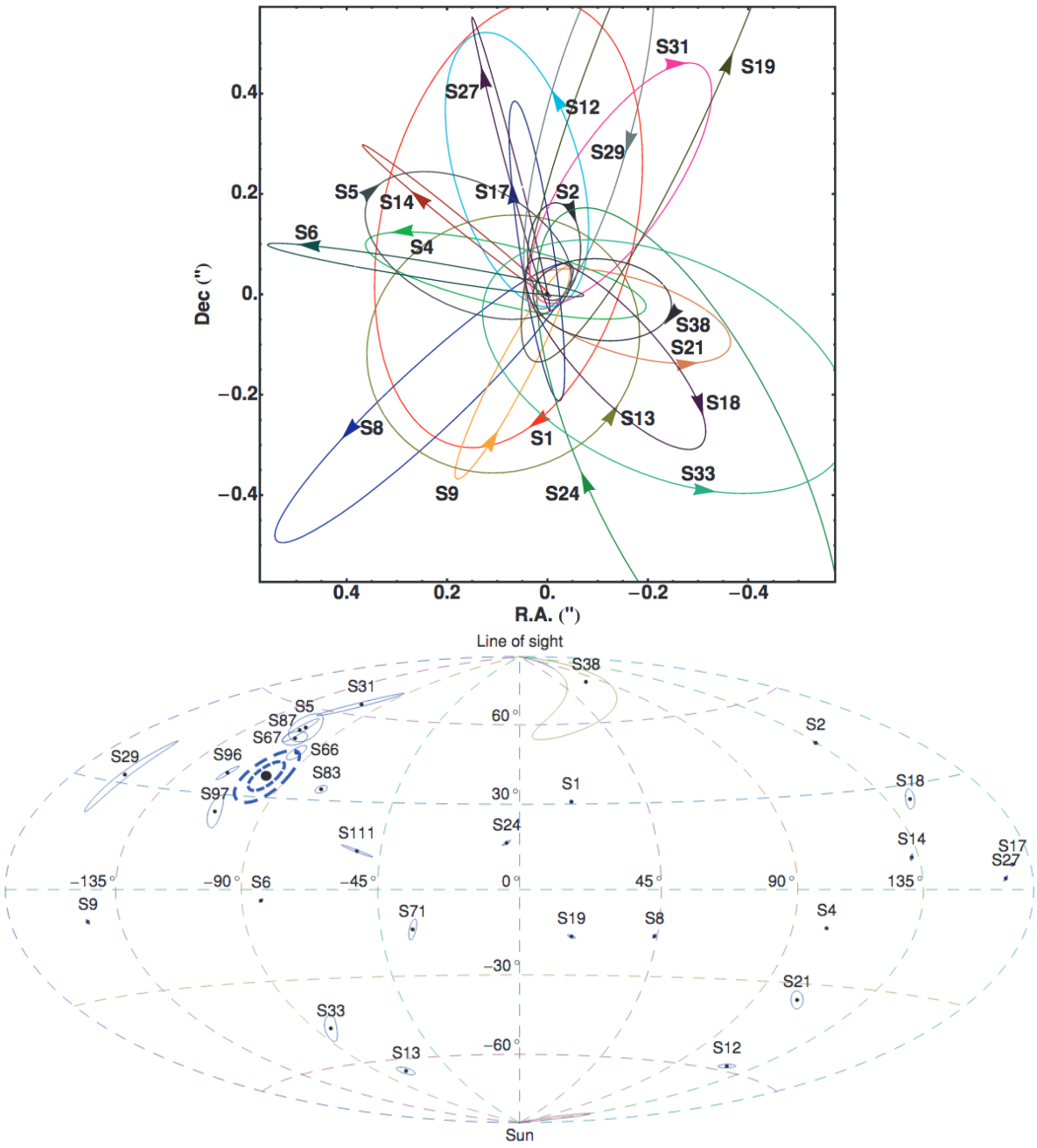

Figure 1.3: The S-stars. Upper: Representation of the best-fit orbits of some of the S-stars, as derived by Gillessen et al. (2009a). Lower: Orbital angular momenta of the S-stars. The horizontal dimension represents the orbital longitude of the ascending node, the vertical dimension represents the orbital inclination. The solid contours correspond to the 1σ statistical fit uncertainty. As visible, some of the S-stars cluster around the clockwise disk (black filled circle and dashed contours, Sec. 1.2.1), according to the detection by Paumard et al. (2006). Both panels are taken from Gillessen et al. (2009a).

has also been confirmed by the detailed analysis of the spectrum of S2/S-02 by Martins et al. (2008), who classified it as a B0-2.5 V star with mass of roughly 20 $M_{\odot}$. As we will mention in Sec. 1.3.1, given its brightness ($K \approx 14$), short orbital period (≈ 16 yr) and small pericenter distance ($\approx 1800\ R_S$), S2/S-02 is crucial for the SMBH's mass estimation. S2/S-02 is also a perfect candidate for a monitoring by the IR interferometer GRAVITY[3] at VLT, to study orbital perturbations induced by general relativity effects and/or other bodies (see Sec. 1.3.1.

As in the case of the CW disk (see Sec. 1.2.1), explaining the formation of the S-star cluster is also challenging. One possibility is the disruption of stellar binaries in the disk and the following capture of one of the two components on a highly eccentric orbit. In this case, dynamical processes such as precession and Kozai-Lidov resonance induced by an anisotropic gravitational potential (Kozai, 1962; Lidov, 1962) might successively lead to the observed isotropic distribution of the orbital inclinations. Another possibility is that the S-stars formed in a disk configuration, but their orbits were moved to random orientations by the interaction with a massive object, e.g., an intermediate mass black hole (IMBH). Again, for details about the possible formation processes, we refer to Mapelli & Gualandris (2016).

1.3 SgrA*: the central supermassive black hole

1.3.1 A strong proof for the existence of supermassive black holes

The first speculations about the existence of black holes go back to the late 18th century, when John Michell and Pierre-Simon Laplace estimated the density of an object whose escape velocity is equal to the speed of light (see Montgomery et al., 2009, for a short but interesting historical review). In a classic Newtonian framework, any photon emitted by such an object would not be able to escape its gravitational field, hence making the object dark to any observer. A similar argument is valid also in the framework of General Relativity: the metric for spherically symmetric objects in vacuum (Schwarzschild, 1916) has a singularity at a particular distance from the object, the Schwarzschild radius (R_S); when the object is compact enough to have its Schwarzschild radius outside its physical surface, the vacuum assumption of the metric is valid and the Schwarzschild radius represents the event horizon, i.e., the distance inside which no information can propagate outwards. Event horizons can also be defined for more sophisticated metrics (Reissner, 1916; Kerr, 1963; Newman et al., 1965).

Indirect evidence for the existence of black holes with few solar masses are obtained by the observation and study of X-ray binaries, one of the most well-known examples being Cygnus X-1 (e.g., see Orosz et al., 2011). The recent detections by the Laser Interferometer Gravitational-Wave Observatory (LIGO)[4] collaboration is also interpreted as the emission

[3] https://www.eso.org/sci/facilities/develop/instruments/gravity.html
[4] http://www.ligo.org/

of gravitational waves from merging binaries of black holes with few tens of solar masses (Abbott et al., 2016a,b).

Nowadays many indications support the existence of a second class of black holes, with much larger masses of $10^5 \lesssim M_{\rm SMBH}/M_\odot < 4\times10^{10}$. Initially, accreting supermassive black holes have been singled out to explain the enormous amount of energy coming from active galactic nuclei (AGN; e.g., Salpeter, 1964; Lynden-Bell, 1969). More recently, the presence of SMBHs in local (active and inactive) galactic nuclei has become clear and the study of dynamics of gas and stars in their vicinity allow a constraint of their masses and sizes up to few parsecs distances (but X-ray spectra and variability also allow to probe accretion onto such objects up to few gravitational radii). A discussion of these methods is beyond the purpose of the present dissertation, hence we refer to the recent reviews by Kormendy & Ho (2013) and Peterson (2014) and to the references therein.

The first indication of a supermassive dark object in the Galactic Center came from the measurement of radial velocities of ionized gas in the inner parsec (see Sec. 1.1) by Wollman et al. (1977), Lacy et al. (1980) and Lacy et al. (1982). These works already allowed to estimate a 'dark' mass of few 10^6 $M_\odot$ in the inner pc. First dynamical estimates for the inner early and late type stars (see Sec. 1.2) by Krabbe et al. (1995), Genzel et al. (1996) and Haller et al. (1996) confirmed the mass estimate and brought the constraint for the size of the supermassive object down to 0.1 pc. A big step forward came with the determination of stellar proper motions with the use of speckle imaging and adaptive optics on the last generation telescopes New Technology Telescope (NTT), Very Large Telescope (VLT) and Keck. The tracking of the inner stars, particularly the S-stars with shorter orbital periods (see Sec. 1.2 and Fig. 1.4 for the orbit of the star S2/S-02) allowed to estimate similar enclosed masses up to the pericenter distance of the inner S-stars, i.e. $\approx 5\times10^{-4}$ pc $\approx 1000R_S$ (Genzel et al., 1997; Eckart & Genzel, 1997; Ghez et al., 1998; Schödel et al., 2003; Ghez et al., 2005a; Eisenhauer et al., 2005; Ghez et al., 2008; Gillessen et al., 2009b,a; Boehle et al., 2016). In particular, the last mass estimates are $4.30\pm0.20\pm0.30\times10^6 M_\odot$ by Gillessen et al. (2009b) and $4.02\pm0.16\pm0.04\times10^6 M_\odot$ by Boehle et al. (2016) (where the first errors are due to the statistical fitting and the second ones are related to systematics), which are consistent with each other.

The inferred density of SgrA* is excluding the possibility of such gravitational field being generated by a cusp of dark stellar remnants or by a fermion ball, possibly composed of neutrinos or any light enough fermion (see Genzel et al., 2010, and references therein). Additionally, the spectral properties of SgrA* can probably rule out the existence of a physical hard surface, rather suggesting the existence of an event horizon. In fact, as suggested by Broderick & Narayan (2006) and Broderick et al. (2009), material reaching and hitting the surface should shock and emit all its energy as black-body radiation in the infrared (IR) to a level that is not observed for the current quiescent level of emission from SgrA* (see Sec. 1.3.2). Finally, in the near future, the IR interferometer GRAVITY will hopefully be able to detect second order relativistic effects on the orbits of the S-stars (e.g., Zucker et al., 2006; Meyer et al., 2012; Zhang et al., 2015) or gravitational lensing from the SMBH (e.g., Bozza & Mancini, 2009). Another strong indication of SgrA* being a very compact object comes from its size and properties in the radio/submm bands. In

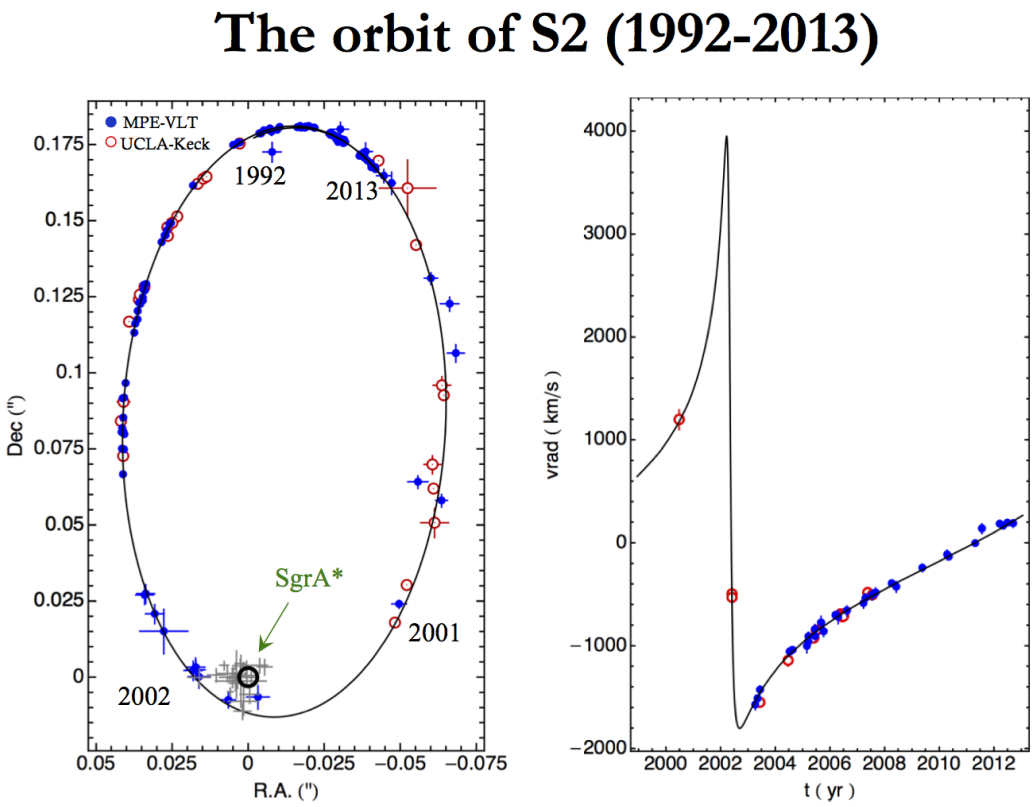

Figure 1.4: The orbit of the star S2/S02, as observed by NTT, VLT (in blue) and Keck (in red). Left panel: orbit in the sky plane. Right panel: line-of-sight velocity as a function of time. The solid lines show the best fitting Keplerian orbit, with SMBH mass of $4.3 \times 10^6\ M_\odot$. Adapted from Gillessen et al. (2009b).

particular, the Event Horizon Telescope[5] (EHT; Doeleman, 2010), consisting of the most up-to-date Very Long-Baseline Interferometry (VLBI) arrays, will allow the imaging of the radio emission from material at few R_S from the SMBH and to test its properties and those of the surrounding plasma in the general relativity regime. The emission properties in these and other bands will be discussed in the next Section.

1.3.2 Emission properties of SgrA* and accretion

SgrA* is spending most of its time in a "quiescent/steady state", with a bolometric luminosity of roughly 10^{36} erg s^{-1}, peaking mainly in the millimeter/submillimeter bands. As shown in Fig. 1.5, its radio spectrum follows approximately a power-law, $L_\nu \approx \nu^{1/3}$, up to

[5]http://www.eventhorizontelescope.org/

217 GHz, (Bower et al., 2015, and references therein). A flat (or slightly decaying) spectrum is observed at submillimeter frequencies (Marrone et al., 2006; Bower et al., 2015), followed by a decaying spectrum in the mid-infrared (MIR) (where we usually have upper limits; Genzel et al., 2010, and references therein) and the near-infrared (NIR) (Do et al., 2009; Dodds-Eden et al., 2011; Witzel et al., 2012). This is usually called the "submillimeter bump". A quiescent emission is also observed in X-ray, at a level of few 10^{33} erg s^{-1} at $2 - 10$ keV (Baganoff et al., 2003; Xu et al., 2006; Wang et al., 2013).

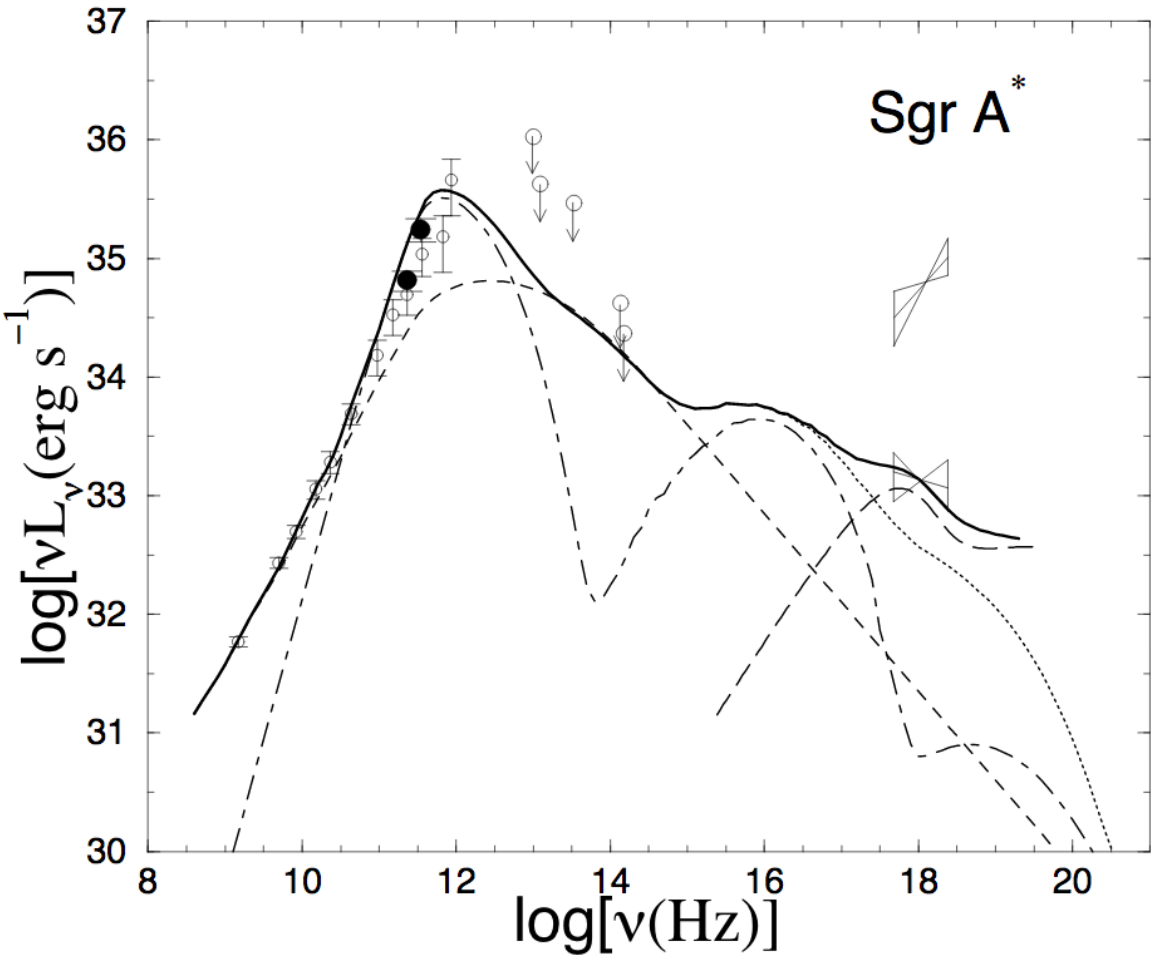

Figure 1.5: Observed broad-band spectrum of SgrA*. The circles show the quiescent radio and infrared emission, while the two "bow ties" show the quiescent and flaring states in the X-ray. A model for the RIAF is overplotted, where the spectrum is composed by synchrotron and inverse Compton emission (dotted line) by thermal (dotted-dashed line) and nonthermal electrons (short-dashed line) and bremsstrahlung emission from the outer part of the accretion flow (long-dashed line). The figure is taken from Yuan et al. (2003).

On top of the quiescent emission, flares are observed in all bands, roughly releasing

another 10^{36} erg s^{-1}, mostly in the X-ray (e.g., Nowak et al., 2012; Ponti et al., 2015; Li et al., 2015; Yuan & Wang, 2016) and the NIR (e.g., Genzel et al., 2003a; Ghez et al., 2004; Yusef-Zadeh et al., 2010; Witzel et al., 2012). The flares are lasting $10^2 - 10^4$ s, with a frequency of roughly one per day for X-ray flares and few per day in the NIR, i.e. any NIR flare has an X-ray counterpart, but not vice versa.

The emission properties of SgrA* allow to exclude the presence of a geometrically thin and optically-thick accretion disk (of the type modeled by Shakura & Sunyaev, 1973), since this would produce several orders of magnitude too high IR fluxes (Falcke & Melia, 1997) and it would lead to the eclipse of the S-stars (Sec. 1.2.2; see, Cuadra et al., 2003). Consequently, nowadays many analytical models of radiatively inefficient accretion flows (RIAFs) are used to fit the broadband quiescent spectrum, such as the Bondi-Hoyle accretion (Melia et al., 2001), the advection dominated accretion flow (ADAF; e.g., Narayan et al., 1995; Özel et al., 2000), the convection dominated accretion flow (CDAF; e.g., Quataert & Gruzinov, 2000), models with outflows as the advection-dominated inflow-outflow solution (ADIOS; e.g., Blandford & Begelman, 1999; Yuan et al., 2003) or even jet models (JDAF; Falcke & Markoff, 2000; Yuan et al., 2002). All these models roughly consider a geometrically thick and optically thin accretion flow and/or some sort of mass loss. This is consistent with most of the magnetohydrodynamic (MHD; some of them in the framework of general relativity, GRMHD) simulations focusing on the inner few tens of R_S of the accretion flow and including magnetic fields (for recent work focused on SgrA*, see, e.g., Mościbrodzka et al., 2009; Dodds-Eden et al., 2010; Dibi et al., 2012; Drappeau et al., 2013; Mościbrodzka & Falcke, 2013; Mościbrodzka et al., 2014; Chan et al., 2015b,a; Ressler et al., 2015; Ball et al., 2016).

The luminosity in the radio and infrared bands is then synchrotron emission produced by a combination of thermal and non-thermal electrons in the inner few R_S from SgrA*, while the X-ray emission could arise either from Compton scattering of the synchrotron photons by the hot electrons or from the outer parts of the accretion flow up to the Bondi radius. In this framework, flares might be explained by events of local acceleration of electrons in the accretion flow or at the base of the jet/outflow by shocks, magnetic reconnection or turbulence (e.g., Markoff et al., 2001; Yuan et al., 2004; Dodds-Eden et al., 2010; Chan et al., 2015a; Dibi et al., 2016). Other possibilities are hot spots in the accretion flow (e.g., Broderick & Loeb, 2005; Eckart et al., 2006), accretion instabilities (Tagger & Melia, 2006), expanding plasma blobs (Yusef-Zadeh et al., 2010; Trap et al., 2011) or tidal disruption of small objects, such as asteroids or planetesimals (Kostić et al., 2009; Zubovas et al., 2012; Hamers & Portegies Zwart, 2015). As previously mentioned, EHT will allow to image the event horizon of SgrA* in radio/submm frequencies, hence hopefully allowing to disentangle between the different models for the quiescent and variable emission and to understand the structure of the innermost accretion.

Such radiatively inefficient accretion flows with outflows/jets are also often used to explain the spectral properties of galactic black holes (i.e., X-ray binaries; e.g., Done et al., 2007; Yuan & Narayan, 2014) and are typically able to describe low (sub-Eddington) accretion rates. SgrA* is often classified as a low-luminosity active galactic nucleus (LLAGN) and does indeed lie on a fundamental plane in the X-ray luminosity - Radio luminosity -

Mass space, along with galactic and extragalactic low-power black holes (Merloni et al., 2003; Falcke et al., 2004). SgrA* has, however, the advantage of being the closest SMBH, offering us the possibility to study the accretion at extremely different scales, spanning 8 orders of magnitude (and more) in Schwarzschild radii. Interestingly, in this region the accretion rate decreases significantly towards the SMBH, being equal to $10^{-2}\ M_\odot\ \mathrm{yr}^{-1}$ in the central molecular zone (CMZ) at $\approx$ 200pc from SgrA*, $10^{-3} - 10^{-4}\ M_\odot\ \mathrm{yr}^{-1}$ at the position of the central nuclear disk (CND) and minispiral (at around 1 pc from SgrA*, see Sec. 1.1), few $10^{-6}\ M_\odot\ \mathrm{yr}^{-1}$ at the Bondi radius (0.05 pc $\approx 10^5 R_S$) and $10^{-9}\ M_\odot\ \mathrm{yr}^{-1}$ at few R_S (see Genzel et al., 2010, and references therein).

Concerning the past activity of SgrA*, some indications can be inferred by X-ray emission from surrounding molecular clouds. This has been interpreted as reflection by Compton scattering of X-ray photons coming from SgrA*. From these observations, many studies have inferred a much higher luminosity of the central object sometimes within the past few hundreds years (e.g., Revnivtsev et al., 2004; Ponti et al., 2010; Clavel et al., 2013; Zhang et al., 2015).

The Galactic Center offers a unique opportunity to understand the feeding of supermassive black holes on spatial and temporal scales that are hard to probe for any other galactic nucleus. Though SgrA* is currently inactive, the current properties and history of its accretion, when tied to those of active galactic nuclei, might hopefully shed light on the cycle of evolution and activity of SMBHs, that is believed to be fundamental for the formation and evolution of galaxies. The mass of central SMBHs is, in fact, found to correlate with the mass/luminosity (Magorrian et al., 1998; Laor, 2001) and velocity dispersion (Gebhardt et al., 2000; Ferrarese & Merritt, 2000) of the spheroidal component of galaxies. This seems to suggest a common formation or co-evolution between the two (for some first speculative models see, e.g., Silk & Rees, 1998; King, 2003). Black hole activity also seems to be needed to reconcile the dark matter halos mass function and the galaxy luminosity function at high masses (e.g., Croton et al., 2006). Hence, SMBHs' histories might be effected by large scale feeding (possibly, through mergers; e.g., Peng, 2007). The SMBH-galaxy connection is, however, still a matter of debate, so we refer to the review by Kormendy & Ho (2013).

The cloud G2, presented in chapter 2 and subject matter of this dissertation, is connected to all the components described in this chapter. Its orbit has a very high eccentricity, as in the case of the S-stars, but its orbital plane roughly corresponds to the plane of the clockwise disk of O/WR stars. It is composed of dust and ionized gas, that might be produced by the winds of the young stars or be connected to the ionized gas in the minispiral. Additionally, it is interacting with the accretion flow towards SgrA*, particularly

at distances from SgrA* ($\approx 1000 R_S$) where the properties of the latter are not very well constrained. Finally, it might significantly feed SgrA* in the near future. This chapter showed how atypical the Galactic Center environment is, compared to the rest of the Milky Way. Hence, the discovery and study of G2 could help the astronomical community to test physics under non-standard and extreme conditions and to clarify many aspects of the evolution of quiescent galactic nuclei, such as the Galactic Center.

Chapter 2

The Galactic Center cloud G2

In this chapter we will present the state-of-the-art understanding of the Galactic Center cloud G2. Section 2.1 will focus on the current observational evidence, while Section 2.2 will present the most up-to-date models for G2's evolution, nature and origin.

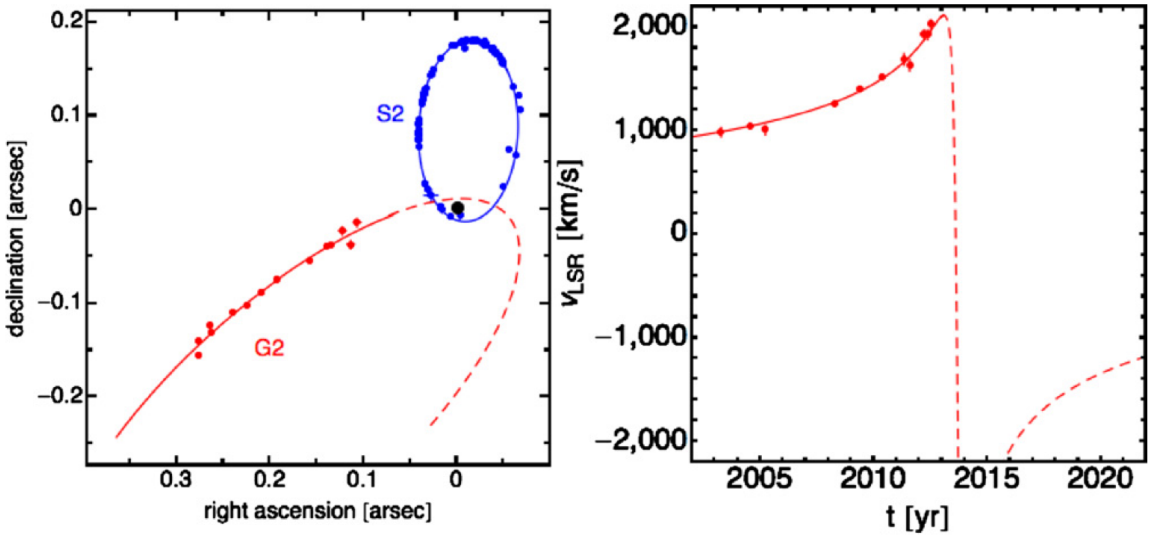

Figure 2.1: Astrometric data in L' and Brγ (left) and line of sight velocity Brγ data (right) allow to tightly constrain G2's orbit (red). In the left panel, the orbit of the S2 star is plotted in blue (from Gillessen et al., 2013a).

2.1 G2: an observational perspective

In year 2012, Gillessen et al. (2012) discovered a small cloud, later named "G2", at few thousands Schwarzschild radii from SgrA* and approaching it with extremely high velocities (of the order of thousands km/s; see Fig. 2.1).

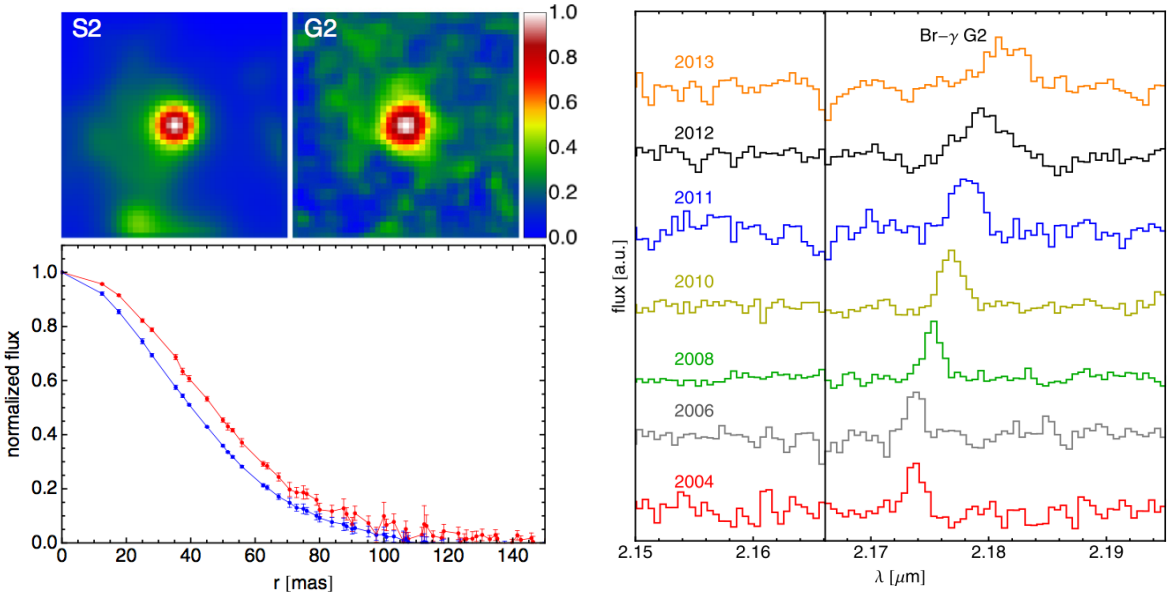

Figure 2.2: Top left: emission of S2 and G2 at the wavelength of G2's Brγ line as measured with SINFONI, averaged over the years 2008, 2010, 2011, 2012 and 2013. Bottom left: comparison of the two radial flux profiles (S2 in blue, G2 in red), showing that G2 appears more extended than the unresolved S2 star. Right: series of spectra around G2's Brγ line obtained by SINFONI. The vertical line marks the wavelength of the Brγ line in the rest frame. The line shift and broadening shows G2's motion along the orbit and its tidal stretching, respectively (taken from Gillessen et al., 2013b).

These authors first presented a series of observations, from year 2004 to year 2012, where G2 is visible both by the NIR imager NACO[1] and the NIR integral field spectrograph SINFONI[2] at the VLT. NACO shows an unresolved component in the L' ($3.490-4.110$ μm) and M' ($4.485-5.075$ μm) bands, but no counterpart in the K_s band ($2.005-2.355$ μm), excluding that such emission comes from a massive star (as the S-stars, see Sec. 1.2.2); thus, it has been interpreted as dust emission with a black body temperature of $T_{\rm BB} \approx 550$ K. On the other hand, SINFONI shows G2 in the Brγ, Paα and HeI recombination lines. As visible in Fig. 2.2, the line emission appears to be marginally resolved in the orbital direction showing an increasing spatial extent and a broadening in the velocity space from roughly 120 km s^{-1} in 2004, 2006 and 2008 (close to the instrumental line width) to around 500 km s^{-1} in 2013 (Gillessen et al., 2013a,b). Its Brγ luminosity is roughly constant with time, $L_{\rm Br\gamma} \approx 2 \times 10^{-3} L_\odot$, maybe showing a slight increase at the pericenter passage, as recently found by Pfuhl et al. (2015). If the Brγ luminosity comes from a diffuse gas cloud which is fully ionized by the ultraviolet (UV) radiation field produced by the nearby young and massive stars, then its temperature will be $T_e \approx 10^4$ K. Under the assumption of

[1]http://www.eso.org/sci/facilities/paranal/instruments/naco/
[2]http://www.eso.org/sci/facilities/paranal/instruments/sinfoni/

case-B recombination and of a homogeneous sphere of radius $R_c \approx 1.9 \times 10^{15}$cm, these authors derived a mass of $M_{\rm G2} \approx 1.7 \times 10^{28}$ g ≈ 3 Earth masses and a uniform density of $\rho_c \approx 6.1 \times 10^{-19}$ g cm^{-3}.

The astrometric and spectral information allowed a precise derivation of G2's orbit: G2 lies on a very eccentric orbit ($e \approx 0.98$) and reached its closest approach to SgrA* in early 2014, with a pericenter distance of approximately 2400 Schwarschild radii (R_S). Interestingly, G2's orbital plane roughly coincides with the one of the clockwise disk of young massive stars (see Sec. 1.2.1) and its apocenter position is well within the disk; this seems to indicate a connection between G2 and this stellar cluster. The latest derived orbital parameters are listed in Table 2.1 (values from Gillessen et al., 2013b).

Orbital parameter	Brγ derived orbit (Gillessen et al., 2013b)
a (mas)	1048 ± 247
e	0.9762 ± 0.0074
i (°)	118.1 ± 2.0
Ω (°)	81.9 ± 4.3
ω (°)	97.2 ± 2.2
t_0 (yr)	2014.25 ± 0.06
P (yr)	391 ± 66
p_0 (R_S)	2400

Table 2.1: Orbital parameters for G2 as derived by Gillessen et al. (2013b). a is the semi-major axis, e the eccentriciy, i the inclination, Ω the longitude of the ascending node, ω the argument of periapsis, t_0 the time of pericenter passage, P the orbital period, p_0 the pericenter distance.

These findings are roughly confirmed by Phifer et al. (2013) and Witzel et al. (2014). In the former work, Phifer et al. (2013) present a monitoring of G2 from 2006 to 2012 in L' and K' bands with the NIR imager NIRC2[3] and in Brγ with the integral field spectrograph OSIRIS[4] at the Keck Observatory. These authors obtained similar eccentricity and time of pericenter passage for G2's orbit and confirm the line broadening and the constant luminosity in Brγ. Additionally, NIRC2 allowed an even more stringent upper limit for G2's K' magnitude to ≈ 20 mag, further excluding a K' band counterpart (however, see Eckart et al., 2013). Additional observations by NIRC2 in 2014, presented by Witzel et al. (2014), showed that the dust component has also a constant magnitude with time ($m_{L'} \approx 14$) and that it remained compact during the pericenter passage.

Integral field spectrographs allow to get a spectrum for any pixel of the image: this allowed Gillessen et al. (2012), Gillessen et al. (2013a), Gillessen et al. (2013b) and Pfuhl et al. (2015) to obtain position-velocity (PV) diagrams of G2. Fig. 2.3 shows a series of PV diagrams from 2008 to 2014. Such diagrams clearly show that G2 has been consistently moving along the derived orbit, they show its broadening in both position and velocity and

[3]http://www2.keck.hawaii.edu/inst/nirc2/
[4]http://www2.keck.hawaii.edu/inst/osiris/

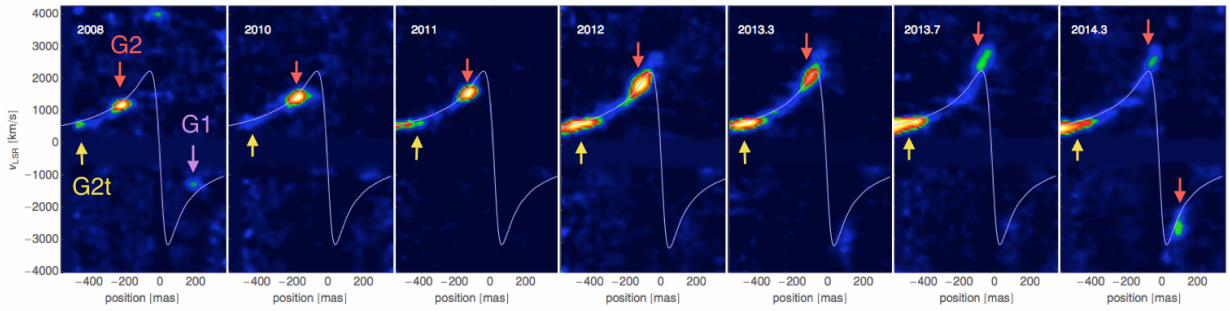

Figure 2.3: Series of PV diagrams for 2008, 2010, 2011, 2012, April 2013, September 2013 and April 2014. The scaling is adjusted in each observed diagram individually to optimally show the structure of the gaseous emission; hence, the diagrams cannot be compared photometrically. The white solid line describes the Brγ orbit of Gillessen et al. (2013b). The arrows highlight the position of G2 (red), G2t (yellow) and G1 (purple). The 2014.3 panel clearly shows G2 splitting in a redshifted and a blushifted part, tracing its pericenter passage as an extended object (adapted from Pfuhl et al., 2015).

that it has passed pericenter in early 2014 (as previously predicted) as an extended object: in fact, already from the beginning of 2013, a second emission spot appeared simultaneously on the blueshifted side of G2's orbit and it became as bright as the redshifted spot in April 2014 (though, this result was not confirmed by Valencia-S. et al., 2015). This is a further indication of G2 being extended in its gas component and getting stretched by the tidal force of the central SMBH.

PV diagrams also show that G2 is connected by some more tenuous material to another bright spot, often called "G2t", following G2 on the same orbit. G2t is also partially detected in the L' band with NACO (Pfuhl et al., 2015). Furthermore, a careful inspection of previous PV diagrams from years 2004, 2006 and 2008 showed a weak precursor of G2 on the blueshifted side of the diagrams (Pfuhl et al., 2015). Such emission seems to be associated to the previously discovered gas/dust cloud G1 (Clénet et al., 2004b,a, 2005; Ghez et al., 2005b), whose orbit can be matched by a G2-like orbit after a drag force is applied to it (Pfuhl et al., 2015; McCourt & Madigan, 2016; Madigan et al., 2016). G2 might then be part of a streamer of clumps.

Several observational programs are currently monitoring its evolution[5], also in other bands, mainly focusing on the interaction of this object with the extreme gravitational field of the $4.31 \times 10^6\ M_\odot$ supermassive black hole (SMBH) and with the hot and dense plasma accreting onto it (see chapter 1). For example, increased emission in X-ray (Gillessen et al., 2012) and radio wavelengths (Narayan et al., 2012a; Sądowski et al., 2013a,b; Crumley & Kumar, 2013; Abarca et al., 2014) has been predicted by modeling of the interaction of G2 with the outer accretion flow (see Sec. 2.2), but no consistent back reaction from either the accretion flow or SgrA* has been detected so far (Haggard et al., 2014; Chandler &

[5]https://wiki.mpe.mpg.de/gascloud/FrontPage

Sjouwerman, 2014; Bower et al., 2015; Borkar et al., 2016). G2's partial or total disruption might also significantly affect the accretion rate onto SgrA* or affect the statistics and properties of flares from SgrA*: in a recent work, Ponti et al. (2015) showed that there has been a recent (starting from late summer 2014) increase in the rate of X-ray bright flares, that might have been induced by G2's pericenter passage. However, these results are still under debate (see, e.g., Mossoux et al., 2016) and further monitoring of SgrA* is needed to draw any strong conclusion.

These observations are performed with the most up-to-date instruments, pushing them to the limits of their capabilities; nonetheless, given the very small scales, there are still some uncertainties on the several physical processes that are involved. Trying to theoretically model the origin and fate of G2 has hence turned out to be challenging, but in the last two years several studies have tried to shed light on this so far peculiar object and we will review them in the next section.

2.2 G2: theory

At first, it is interesting to understand the importance of all the possible physical processes affecting G2's evolution. We will hence provide a few estimates of the different corresponding timescales and compare them. Some of these estimates can also be found in Burkert et al. (2012), Schartmann et al. (2012) and Anninos et al. (2012).

The first important timescale is related to G2's orbital evolution. Two timescales can be chosen, namely the orbital timescale $\tau_{\rm orb}$ and the free-fall timescale $\tau_{\rm ff}$. The former is a measure of the "dynamical lifetime" of the cloud, while the latter can provide an idea of how much time the cloud is spending on a certain position of the orbit (it is then expressing the concept behind the 2nd Kepler's law; the free-fall is also a reasonable assumption, given the high eccentricity of G2's orbit). Both timescales are somewhat meaningful: every physical process is acting all along G2's orbit, thus it makes sense to compare its timescale to the orbital timescale. However, the timescale of a process is describing its effectiveness depending on the position of G2, hence it is probably reasonable to compare this to a "local" dynamical timescale. In the case of G2, $\tau_{\rm orb} \approx 400$ yr, while

$$\tau_{\rm ff} \approx \frac{\pi}{2} \frac{d_{\rm SMBH}^{3/2}}{\sqrt{2GM_{\rm SMBH}}} \approx 1.5 \left(\frac{d_{\rm SMBH}}{10^{16}\ {\rm cm}} \right)^{3/2}\ {\rm yr}, \tag{2.1}$$

where $d_{\rm SMBH}$ is the distance of G2 from SgrA* and $M_{\rm SMBH} = 4.31 \times 10^6\ M_\odot$ is the mass of SgrA* (see Sec. 1.3; Gillessen et al., 2009a).

The first physical process that needs to be considered is the tidal stretching of the cloud. This is purely due to the strong gravity of the black hole, which produces an acceleration at the outer rim of the cloud

$$|a_{\rm ts}| = 2R_c G \frac{M_{\rm SMBH}}{d_{\rm SMBH}^3}, \tag{2.2}$$

where $R_c = 1.9 \times 10^{15}$ cm is G2's radius, as derived from the observations (see Sec. 2.1). The relative timescale for G2's "spaghettification" (i.e., for G2 to get stretched to twice its size) is then

$$\tau_{\rm ts} \approx \left(\frac{2R_c}{|a_{\rm ts}|}\right)^{1/2} = \frac{d_{\rm SMBH}^{3/2}}{\sqrt{GM_{\rm SMBH}}} \approx 1.3 \left(\frac{d_{\rm SMBH}}{10^{16}\ {\rm cm}}\right)^{3/2}\ {\rm yr}. \tag{2.3}$$

This value is similar to the free-fall time and much shorter than the orbital time, hence fully explaining the increase in size and velocity gradient observed in the cloud.

In this respect, one can also estimate the role of a central object with mass m in opposing the tidal force of SgrA* and binding G2. This corresponds to saying that its binding acceleration is bigger than the tidal one, i.e. $|g_{\rm m}| > |a_{\rm ts}|$. This implies

$$\frac{R_c}{d_{\rm SMBH}} < \left(\frac{m}{2M_{\rm SMBH}}\right)^{1/3}. \tag{2.4}$$

If we use an (extremely conservative, see Sec. 2.1 and Gillessen et al., 2012) upper limit for m of 8.62 $M_\odot$, we get that

$$\frac{R_c}{d_{\rm SMBH}} < 10^{-2}, \tag{2.5}$$

which does not hold over most of the orbit of G2 - except, maybe, close to apocenter - and, certainly, it does not close to pericenter, i.e. for the period of the last available observations. Vice versa, considering that the estimated radius of G2 is of the order of its pericenter distance from SgrA* (see Sec. 2.2.1), m should be of the order of the mass of the SMBH to be effective enough to oppose the strong tidal field felt by the cloud[1].

Another interesting timescale is the cooling time of the cloud, defined as

$$\tau_{\rm cool} = \frac{3k_{\rm B}T_c}{2n_c\Lambda_{cool}}, \tag{2.6}$$

where k_B is the Boltzmann constant and $\Lambda_{\rm cool}$ is the cooling rate. If we assume $T_c = 10^4$ K and $n_c \approx 5 \times 10^5$ cm^{-3} as derived by the observations (see Sec. 2.1) and $\Lambda_{\rm cool} = 10^{-22}$ erg cm^3 s^{-1}, which is roughly the value for 10^4 K and solar metallicity (see, e.g., Sutherland & Dopita, 1993), $\tau_{\rm cool} \approx 1.3 \times 10^{-3}$ yr, which is extremely short. Under the assumption of balance between heating and cooling from the surrounding ionizing photons (see 2.1), the cloud can then be considered isothermal.

Other important physical processes affecting G2's evolution might be related to its interaction with the surrounding hot accretion flow (see sections 1.1.3 and 1.3.2). In order

[1]To be precise, Eq. 2.2 is an approximation, valid as long as $R_c << d_{\rm SMBH}$, based on the McLaurin/Taylor expansion of the exact acceleration $-GM_{\rm SMBH}/(d_{\rm SMBH} \pm R_c)^2$ felt by the leading and trailing parts of the cloud. However, the goal of our calculation is to provide an order of magnitude estimate, hence our conclusion about the mass of the embedded object is still to be considered correct, even when the size of G2 is similar to its distance to SgrA*.

to perform a few additional estimates, we can assume that the density and temperature profiles for the accretion flow are

$$n_{\rm at} = 930 \left(\frac{1.4 \times 10^4 \ R_{\rm S}}{d_{\rm SMBH}} \right) \ {\rm cm}^{-3} \approx 1658.15 \left(\frac{10^{16} \ {\rm cm}}{d_{\rm SMBH}} \right) \ {\rm cm}^{-3}, \tag{2.7}$$

$$T_{\rm at} = 1.2 \times 10^8 \left(\frac{1.4 \times 10^4 \ R_{\rm S}}{d_{\rm SMBH}} \right) \ {\rm K} \approx 2.14 \times 10^8 \left(\frac{10^{16} \ {\rm cm}}{d_{\rm SMBH}} \right) \ {\rm K}, \tag{2.8}$$

where $R_{\rm S} = 2GM_{\rm SMBH}/c^2$ is the Schwarzschild radius of the SMBH (c being the speed of light). These profiles correspond to the radiatively inefficient accretion flow (RIAF) analytical approximation of Yuan et al. (2003) (see Sec. 1.3.2), matching the current *Chandra* X-ray observations (Baganoff et al., 2003) and radio rotation measure data (Bower et al., 2003), under the assumption of hydrostatic equilibrium with the Newtonian potential of the SMBH (see also Burkert et al., 2012; Schartmann et al., 2012; Anninos et al., 2012).

The first estimate can involve a comparison between the thermal pressure $P_{\rm th}$ and the ram pressure $P_{\rm ram}$ of the accretion flow. Under the simplified assumptions of a static surrounding, the latter is given by $\rho_{\rm at} v_{\rm G2}^2$, hence

$$\frac{P_{\rm ram}}{P_{\rm th}} = \frac{\mu m_{\rm H} v_{\rm ff}^2}{k_{\rm B} T_{\rm at}} \approx \frac{2\mu m_{\rm H} G M_{\rm SMBH}}{k_{\rm B} T_{\rm at} d_{\rm SMBH}} \approx 4, \tag{2.9}$$

where μ is the mean molecular weight, $m_{\rm H}$ is the hydrogen mass and the $v_{\rm G2}$ has been approximated as $v_{\rm ff} = (2GM_{\rm SMBH}/d_{\rm SMBH})^{1/2}$, i.e., the velocity of a body falling from infinity. In this case, and for our choice of the temperature profile, the ratio of the two pressures does not depend on the distance from SgrA*. We will see that this is not strictly exact for the actual orbit of G2 (see Fig. 5.1 and Burkert et al., 2012), but it proves that the two pressures are comparable. Hence, they can both have an impact on the evolution of the cloud.

One first thing to check is, however, how fast the cloud reacts to the changes in pressure along the orbit. For this purpose, we will use the thermal pressure (but an equivalent argument can apply to the ram pressure, too). To get an estimate of this, we can calculate the sound crossing time of the cloud

$$\tau_{\rm sc} = \frac{R_c}{c_{s,c}} = R_c \sqrt{\frac{\mu m_{\rm H}}{k_{\rm B} T}}, \tag{2.10}$$

where $c_{s,c}$ is the sound speed in the (isothermal) cloud. As we showed before, the cooling time of G2 is extremely short and we can assume that G2 reacts isothermally to any thermodynamic modification. If its temperature is $T_c = 10^4$ K, then $\tau_{sc} \approx 52$ yr. It is then interesting to compare the sound crossing time to the rate of change of the external pressure along G2's orbit. The corresponding timescale can be approximated by

$$\tau_P = \frac{P_{\rm at}}{\dot{P}_{\rm at}} = \frac{P_{\rm at}}{v_{\rm ff} dP_{\rm at}/d(d_{\rm SMBH})} \approx 0.66 \left(\frac{r}{10^{16} \ {\rm cm}} \right)^{3/2} \ {\rm yr}. \tag{2.11}$$

This is much shorter than the sound crossing time, for most of G2's orbit. Hence, the cloud will always be immediately compressed under the external pressure. This timescale is also comparable to the free-fall and tidal stretching timescale, within a factor of roughly two.

The cloud might also be subject to hydrodynamical instabilities. The timescale for the Rayleigh-Taylor instability might be approximated by

$$\tau_{\rm RTI} = \left(\frac{2\pi}{R_c} \frac{GM_{\rm SMBH}}{d^2_{\rm SMBH}} \frac{\rho_c - \rho_{\rm at}}{\rho_c + \rho_{\rm at}} \right)^{-1/2}. \tag{2.12}$$

The Atwood number $(\rho_c - \rho_{\rm at})/(\rho_c + \rho_{\rm at})$ is always close to one even at G2's pericenter, hence

$$\tau_{\rm RTI} \approx 0.23 \frac{d_{\rm SMBH}}{10^{16}\ {\rm cm}}\ {\rm yr}, \tag{2.13}$$

which is shorter or comparable to the free-fall timescale.

The Kelvin-Helmholtz instability timescale can be expressed, instead, as

$$\tau_{\rm KHI} = \left(\frac{2\pi}{R_c} \right)^{-1} \left(\frac{2GM_{\rm SMBH}}{d_{\rm SMBH}} \right)^{-1/2} \left(\frac{\rho_c}{\rho_{\rm at}} \right)^{1/2} = 0.54 \left(\frac{d_{\rm SMBH}}{10^{16}\ {\rm cm}} \right)\ {\rm yr}, \tag{2.14}$$

again shorter or comparable to the free-fall timescale. Hydrodynamical instabilities can then be important for G2's evolution. On the other hand, magnetic fields - that are not considered here - might suppress them.

One last process we might consider here is evaporation by thermal conduction. As shown by Burkert et al. (2012) and Anninos et al. (2012), G2 might be in a saturated state and its evaporation timescale is (Cowie & McKee, 1977)

$$\tau_{\rm evap} \approx 9 \times 10^{-13} (2.73\sigma_0)^{3/8}_0 R_{\rm c,cm} \frac{\rho_c}{\rho_{\rm at}} T^{-1/2}_{\rm at,K}\ {\rm yr} \approx 15.62 \left(\frac{d_{\rm SMBH}}{10^{16}\ {\rm cm}} \right)^{3/2}\ {\rm yr}, \tag{2.15}$$

where we adopted a saturation parameter $\sigma_0 = 100$ (see Burkert et al., 2012). This timescale is longer than then the free-fall time, but shorter than the orbital time. This means that thermal conduction is not extremely efficient, as long as G2 formed at apocenter or along its first "plunge", but it could become important over one or more orbital periods. However, thermal conduction is strongly dependent on microphysics and magnetic fields, hence such estimate is to be taken with a grain of salt (even more than in the other cases).

In summary, we showed that G2

- is strongly effected by the tidal field of SgrA* and no central object with reasonable mass can keep it compact;
- is isothermal and is always confined by the external thermal and ram pressures of the accretion flow;

- might be subject to hydrodynamical instabilities, unless magnetic fields act to suppress them;
- is perhaps not subject to heat conduction.

Of course, there are two major caveats for the present estimates. First, all the considered processes are highly non-linear, they are simultaneously acting on G2 and affecting each other. Second, for the sake of simplicity, many of the performed estimates are considering G2 as a diffuse cloud, with fixed density and radius, which the estimates themselves show not to be the case.

Hence, more detailed studies, possibly involving simulations, are fundamental. In the next two subsections, we will review all the work done to understand G2 and its future evolution. This theoretical effort can be divided in two main subcategories, based on G2's nature: G2 might simply be a cloud of gas and dust (Sec. 2.2.1) or it could be related to a central object embedded in it (Sec. 2.2.2).

2.2.1 G2 as a diffuse cloud

Origin and pre-pericenter evolution

Several studies have been carried out for the diffuse cloud scenario proposed by Gillessen et al. (2012) (see Sec. 2.1), focusing on the origin and pre-pericenter evolution of G2 and on its interaction with SgrA*'s accretion flow. Burkert et al. (2012) performed some first analytical estimates; in addition to those provided in this dissertation, they showed that the cloud must have formed in rough pressure equilibrium with the environment: in fact, a too underpressured cloud would have imploded very fast, while a too overpressured one would probably look too extended in the observations. Furthermore, these authors also showed that cloud ablation and deceleration due to ram pressure interaction with the atmosphere should all be minor effects before pericenter. However, thermal conduction might set an upper limit to the lifetime of such a cloud of the order of 100 yr, above which the cloud should be evaporated (but see before). As showed before, when G2 approaches pericenter, the tidal force of the SMBH becomes extremely important and reduces the cloud to a long and thin "spaghetto". Burkert et al. (2012) and Schartmann et al. (2012) also were the first to present some 2D hydrodynamic simulations, by means of the Eulerian code PLUTO, studying the properties and evolution of a diffuse cloud. Attempting a first rough comparison with the observed PV diagrams, these studies found that G2 might have formed very recently, in 1995, in pressure equilibrium with the surrounding atmosphere, modeled as a hot and dense accretion flow, with density and temperature profiles equal to those in Eq. 2.7, and 2.8. These authors also tested a different model, consisting of a large spherical shell forming close to G2's apocenter; such a gas configuration is able to roughly reproduce the observations for both G2 and its tail G2t. In following studies, Anninos et al. (2012) (left panel in Fig. 2.4) and Saitoh et al. (2014) repeated the compact diffuse cloud simulations of Burkert et al. (2012) and Schartmann et al. (2012) with different techniques. Anninos et al. (2012) used a 3D cartesian grid moving along with G2 (upper panel of Fig.

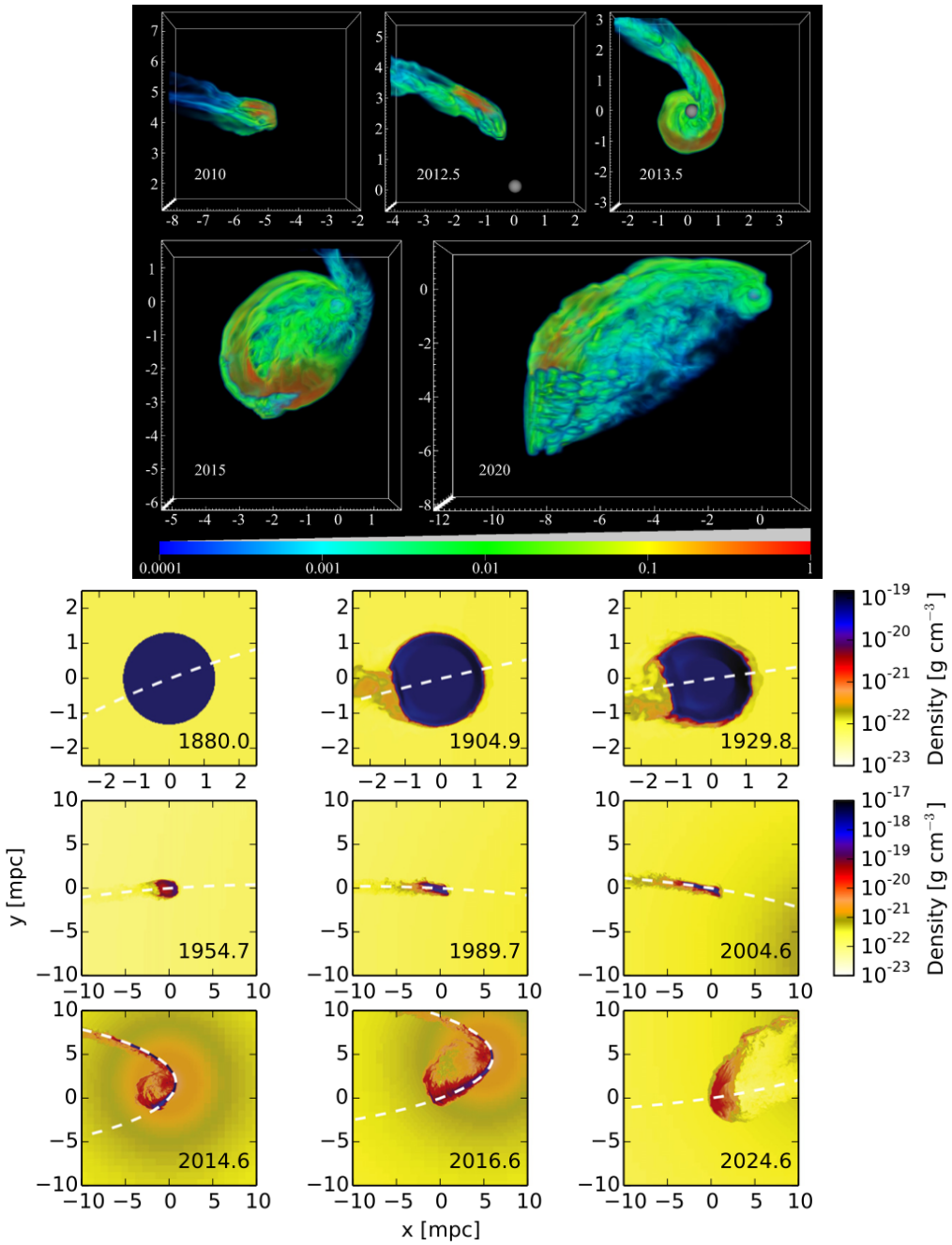

Figure 2.4: Evolution of G2 as a diffuse cloud in hydrodynamical simulations. Upper panel: 3D volume rendering of the cloud tracer for one of the models in Anninos et al. (2012). Lower panel: Density cuts through the orbital plane for one of the 3D simulations in Schartmann et al. (2015).

2.4), while Saitoh et al. (2014) used smoothed-particle hydrodynamics (SPH); they studied the effects of the equation of state and of the atmosphere's structure on the evolution of the cloud, basically confirming what was previously obtained with 2D simulations for the early evolution. Recent 3D adaptive-mesh refinement simulations have also been presented by Schartmann et al. (2015) (lower panel in Fig. 2.4); by means of a more realistic construction of mock PV diagrams, these authors revised the previous finding of G2 needing to be formed recently and close to pericenter. Indeed, in order to best match the observed size of G2, the cloud should have been formed much earlier (i.e., before 1900), well within the disk of young stars, suggesting that G2 might be connected to the O-WR stars (see Sec 1.2.1).

The connection with the clockwise disk of young stars is also appealing to explain the low angular momentum of G2. As suggested by Burkert et al. (2012), the wind velocities of some of these stars (particularly the LBV) are similar to their orbital velocities (see Sec. 1.2.1); hence, G2 might be produced by the cooling of wind shells, in their downstreaming parts. Indeed, the simulations of these stellar winds by Cuadra et al. (2006) and Cuadra et al. (2008) show the formation of a relatively high number of cold clumps at temperatures of the order of 10^4 K. The collision of stellar winds might also generate low angular momentum clumps: as shown by Calderón et al. (2016), the non linear thin shell instability (NTSI) (Vishniac, 1994) can trigger clump formation in the slab formed by the collision of two stellar winds and the produced clumps can have a large spectrum of masses; in particular, the binary system IRS 16 SW (Martins et al., 2006; Pfuhl et al., 2014) is a suggestive candidate for G2's formation, when considering its position compared to G2's apocenter and its wind parameters. Another interesting possibility has been suggested by Guillochon et al. (2014a): with the help of 3D AMR simulations, these authors show that G2 might be a clump condensing due to cooling in a streamer of gas. In their model, the streamer is produced by the tidal stripping of the outer envelope of a late-type giant star, in a close encounter of such a star with the central SMBH. This scenario has the advantage of providing a possible explanation for the existence of G2, G2t and G1 simultaneously, if they are causally connected to each other.

Pericenter and post-pericenter evolution

The pericenter passage of G2 is of particular interest, since it is the moment of maximum "stress" for G2. In this part of the orbit, the orbital velocity, the external density and temperature and the tidal force are the highest of the whole orbital evolution.

The previously mentioned simulations by Schartmann et al. (2012), Schartmann et al. (2015), Anninos et al. (2012) and Guillochon et al. (2014a) show that at pericenter G2 is a very elongated "spaghetto" (see Fig. 2.4); however, G2 always expands in its post-pericenter evolution, particularly in the direction perpendicular to the orbit. In this kind of simulations, a part of G2 is also ablated in the process and gets funneled towards SgrA*, in a nozzle-like mode. The accretion rates at few hundred Schwarzschild radii, concerning the cloud material, derived by Schartmann et al. (2012), Anninos et al. (2012) and Saitoh et al. (2014) are all between $4 \times 10^{-8} M_\odot$ yr^{-1} and $10^{-7} M_\odot$ yr^{-1}, i.e. below or comparable with the estimated quiescent accretion rate. The previous works have a quite

idealized atmosphere and all neglect any possible rotation of the accretion flow. Abarca et al. (2014) attempted a study of the effect of a more realistic accretion flow on the pericenter passage of G2: these authors performed hydrodynamic simulations of a diffuse cloud interacting with a thick accretion disk, based on the "magnetically arrested disk" (MAD) model (i.e., an accretion disk where the magnetic field strongly resists the inflow of material towards the central object) of Narayan et al. (2012c): these authors show that, depending on the orientation of G2's orbit compared to the rotation of the accretion flow, the evolution of G2 immediately after pericenter could produce, in some more extreme cases, different signatures in the observed PV diagrams. Recent simulations by McCourt et al. (2015) of clouds in a wind tunnel, however, show that the addition of magnetic fields to the hydrodynamical interaction between G2 and its environment could help avoiding the disruption of the cloud, inhibiting mixing of the cloud with the surrounding. At the same time, magnetic fields could induce a more efficient drag force, which could allow G2 to significantly deviate from its pre-pericenter orbit. As mentioned in Sec. 2.1, the effects of the drag force of the accretion flow on the post-pericenter evolution of G2 have also been studied by Pfuhl et al. (2015), McCourt & Madigan (2016) and Madigan et al. (2016), in the attempt of connecting the orbit of G2 to that of its possible precursor G1. Following the finding of McCourt et al. (2015), Pfuhl et al. (2015) tested the evolution of G2 as a point particle feeling a Keplerian potential plus a drag force due to the MHD interaction with a static ADAF-like atmosphere. Successively, McCourt & Madigan (2016) and Madigan et al. (2016) added the rotation and the inflow motion of the accretion flow, respectively. These authors find that the two orbits can be reconciled when taking these effects into account. However, such models work under the assumptions of a constant cross section for the test clouds along the orbit, which is very idealized given the strong tidal force of SgrA*.

Large effort has been put also in explaining and predicting the emission properties from G2 and its interaction with the accretion flow close to pericenter. The simulations by Anninos et al. (2012) and Saitoh et al. (2014) were used to estimate the recombination line emission. Integrating the cooling rate of the gas particles during their run, Saitoh et al. (2014) found that the bolometric and Brγ luminosity should have strongly peaked around pericenter, with an increase of more than two orders of magnitude from 2008 to 2014, which is not observed. Similar results occur for certain models of Anninos et al. (2012): as shown in Fragile et al. (2014), all their isothermal models have an increase of luminosity of roughly one order of magnitude towards pericenter; however, simulations where a significant heating of G2 is allowed show an almost flat light curve, as is the case for the observations. The same trend has been found by Schartmann et al. (2015), in the case of their lower resolutions run: as a consequence, these authors argue that a higher mixing (corresponding to heating of the cloud) or some phenomenon preventing the collapse of G2 in the direction perpendicular to its orbit might help to mitigate the steep rise of G2's luminosity close to pericenter. The latter hypothesis is compatible with the work by Shcherbakov (2014): in this work, the author performed 1D radiative transfer calculations with the CLOUDY code to study the photoionization of a cloud (with different shapes and sizes) under the exposure to the radiation field from the surrounding stars. The model that best reproduces

G2's size, mass and luminosity evolution is the "magnetically arrested" cloud, in which a magnetic field induces an additional pressure and opposes the tidal gravitational force, hence reducing the compression of the cloud in the direction perpendicular to the orbit. As a final interesting remark on the Brγ emission, all the models discussed in Fragile et al. (2014) and Schartmann et al. (2015) show a sudden drop of luminosity after pericenter. This is also visible in the simulations by Guillochon et al. (2014a). Hence, unless some important additional ingredient is missing in these simulations, G2 should disappear from PV diagrams some time after pericenter.

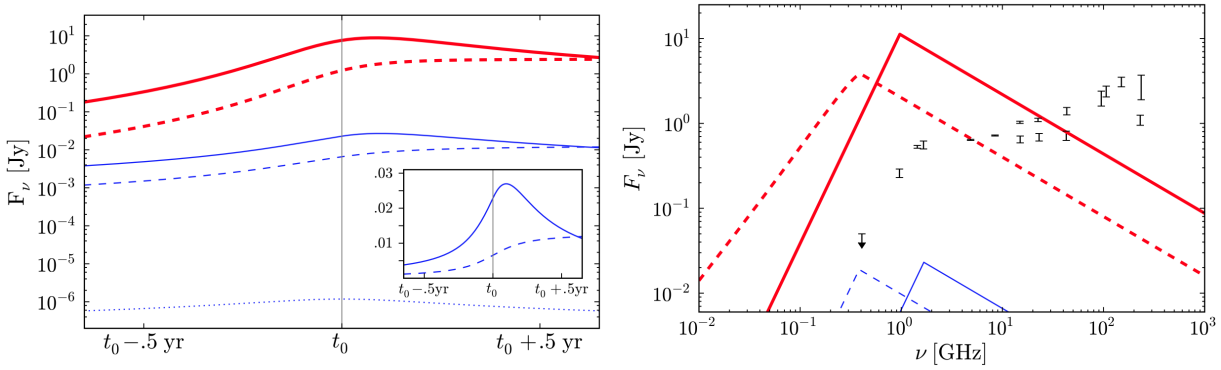

Figure 2.5: Estimates for the radio emission from G2's bow shock. The blue lines correspond to the stellar wind calculation of Crumley & Kumar (2013), the red lines basically correspond to the estimates in Sądowski et al. (2013b) for a diffuse cloud. Solid and dashed lines correspond to different assumptions on the location of the emitting electrons accelerated in the outer shock propagating in the environment, while the blue dotted line represents the emission from the inner shocked wind. Left: Evolution of the radio flux at 1.4 GHz around the pericenter passage of G2's bow shock (t_0). Right: Spectra for the bow shock, at time $t_0 + 0.05$ yr. The data points represent observations for the quiescent radio emission of SgrA*. The figure is taken from Crumley & Kumar (2013).

Moving to other observational bands of the electromagnetic spectrum, some authors focused on the radio emission of the bow shock that should form in the accretion flow at G2's passage. In fact, for many of the assumed temperature profiles of the accretion flow, G2 should move subsonically close to its apocenter, but become slightly supersonic during its motion towards pericenter (see, e.g., Burkert et al., 2012). By means of particle-in-cell simulations, Narayan et al. (2012b) calculated the energy spectrum of electrons accelerated in the shock by Fermi-like, shock-drift acceleration mechanisms. According to their estimates, synchrotron emission from these electrons would have led to a significant increase of the radio emission below 100 GHz ($\approx 1-20$ Jy at 1.4 GHz), compared to SgrA*'s quiescent level. These results are also compatible with the somewhat more sophisticated calculation presented in Sądowski et al. (2013b) (see Fig. 2.5). Sądowski et al. (2013b) also predicted a peak of the radio emission occurring roughly 4 months before G2's pericenter, while Sądowski et al. (2013a) revised these estimates to 6-8 months before. However,

as mentioned in Sec. 2.1, no significant increase of the emission has been detected in the radio band. This might have to do with the assumptions made by these authors, in particular concerning G2's cross section. In fact, similar estimates for the model presented by Shcherbakov (2014), having a factor of ten smaller radius for G2, have a significantly smaller predicted emission, compared to Narayan et al. (2012a) and Sądowski et al. (2013b), and fall below the observed quiescent level. Concerning X-ray emission, Gillessen et al. (2012) estimated emission from the shock propagating inside G2 after its interaction with the accretion flow, estimating a luminosity of the order of 10^{34} erg s^{-1}, i.e. roughly a factor of 3 larger than the quiescent X-ray luminosity of SgrA* (see Sec. 1.3.2). Shcherbakov (2014), instead, predicted a luminosity of 2×10^{33} erg s^{-1} (comparable or slightly below the quiescent emission) from the electrons accelerated in the external shock. Again, as discussed in Sec. 2.1, also the X-ray observations showed no significant increase in the emission of SgrA*, hence invalidating the estimate by Gillessen et al. (2012). This might be the proof that the hydrodynamical interaction is somehow less significant than expected. However, it must also be stressed that some of these estimates often strongly depend on the details of the assumed structure of the accretion flow, which is however poorly constrained at these distances from the SMBH.

Finally, Bartos et al. (2013) predict that G2 might have roughly 10 encounters with stellar BHs around (±6 months) its pericenter, for the currently estimated populations of stellar BHs in the Galactic Center. If G2 is a cloud, these events - or encounters with other "dark objects" - might have been detectable with the Chandra X-ray telescope (or, under some extreme cases, by NuSTAR). Similar results, in terms of number of encounters, are found by de la Fuente Marcos & de la Fuente Marcos (2013), even though these authors tend to estimate a possible lower resulting X-ray variability of the inner region of the Galactic Center, compared to Bartos et al. (2013). Anyway, as already mentioned, no significant X-ray anomaly has been detected in the last years, also invalidating the latter (admittedly very optimistic) estimates.

2.2.2 A central object in G2

A significant contribution to the investigation of G2 being related to a central object has been given by the work presented in Ballone et al. (2013) and Ballone et al. (2016) and it is part of the present dissertation. Hence, we will not include these works in the current Section, but rather refer to the following Chapters 5 and 6 for their fully detailed presentation and discussion.

Origin and pre-pericenter evolution

The second subset of theoretical work on G2 involves a connection with a central source on G2's orbit. The first model of this type was presented by Murray-Clay & Loeb (2012), suggesting that G2 is actually the outflow generated by the photoevaporation of a proto-planetary disk around a low mass young star. The photoevaporation is supposed to be driven by the extremely high flux of ionizing photons emitted by the surrounding massive

stars. Such a model requires a young star on G2's orbit, which is not extremely probable, considering that only 2 of the S-stars have eccentricities $\gtrsim 0.95$ (Gillessen et al., 2009a). However, given G2's orbital plane, Murray-Clay & Loeb (2012) assumed that its possible source originally formed in the clockwise disk of young stars and that it has later been scattered by two-body encounters with the massive stars in the disk. Their calculation gives a probability of $\approx 0.1\%$ of observing a source with a protoplanetary disk at its first pericenter, which makes this possibility unlikely but possible. The idea of a photoevaporating disk has also been tested by Miralda-Escudé (2012), who suggested that the disk might be formed by the interaction of a star with a stellar black hole: such a scattering event could simultaneously bring the star on a highly eccentric orbit and produce a disk around the star, if the latter is an old, low-mass one. The probability of such an event is also roughly the same as in the case of Murray-Clay & Loeb (2012). Other works focus on the possibility of a T Tauri star. These stars are known to be both accreting and having outflows and they are very young stellar objects, making them compatible with the age of the stars in the clockwise disk (4-8 Myr, Paumard et al., 2006; Bartko et al., 2009) (see also Sec. 1.2.1). Through the support of some analytical estimates, Scoville & Burkert (2013) suggested that G2 (or, at least, its Brγ component) might actually be the shocked outflow of a T Tauri star interacting with the external accretion flow (see left panel of Fig. 2.6). This hypothesis has been later tested in the published material presented in this dissertation and also through the numerical simulations in De Colle et al. (2014) (see right panel of Fig. 2.6). Later, Zajaček et al. (2014) and Zajaček et al. (2016) tested outflows and bow shocks to explain some of the dust and Brγ properties of G2, also in the presence of an isotropic outflow from SgrA*. Another scenario related to a central source has been presented by Mapelli & Ripamonti (2015), where G2's Brγ emission is produced by the outflow from a photoevaporating planet or planet "embryo". A following study by Trani et al. (2016) showed indeed that the semi-major axis and eccentricity of planets captured by gravitational field of the SMBH can match those of G2, if the planet is escaping a star with orbital properties similar to those of the S-stars (see Sec. 1.2.2). Somehow different is the idea presented by Meyer & Meyer-Hofmeister (2012), which suggested that G2 might have been the product of a recent nova outburst, happening around year 2000. In such a model, different parts of the dense shell produced in the outburst would have different orbital properties, hence explaining G2 and possibly also G2t. However, the source would be nowadays orbitally decoupled from G2 and the tail. Finally, Witzel et al. (2014) suggested that G2 might be the byproduct of a stellar binary system merger. Indeed, following work by Prodan et al. (2015) and Stephan et al. (2016) showed that the Kozai-Lidov mechanism in the three-body system binary-SBMH, coupled to dissipative processes (e.g., tidal friction), might trigger such mergers. Such a scenario works in explaining the G2's dust component, but it is not fully clear how it can explain the extended gas.

Pericenter and post-pericenter evolution

As in the case of some work on the diffuse cloud, also many of the models involving a central source predict increased Brγ luminosity close to pericenter. This might simply

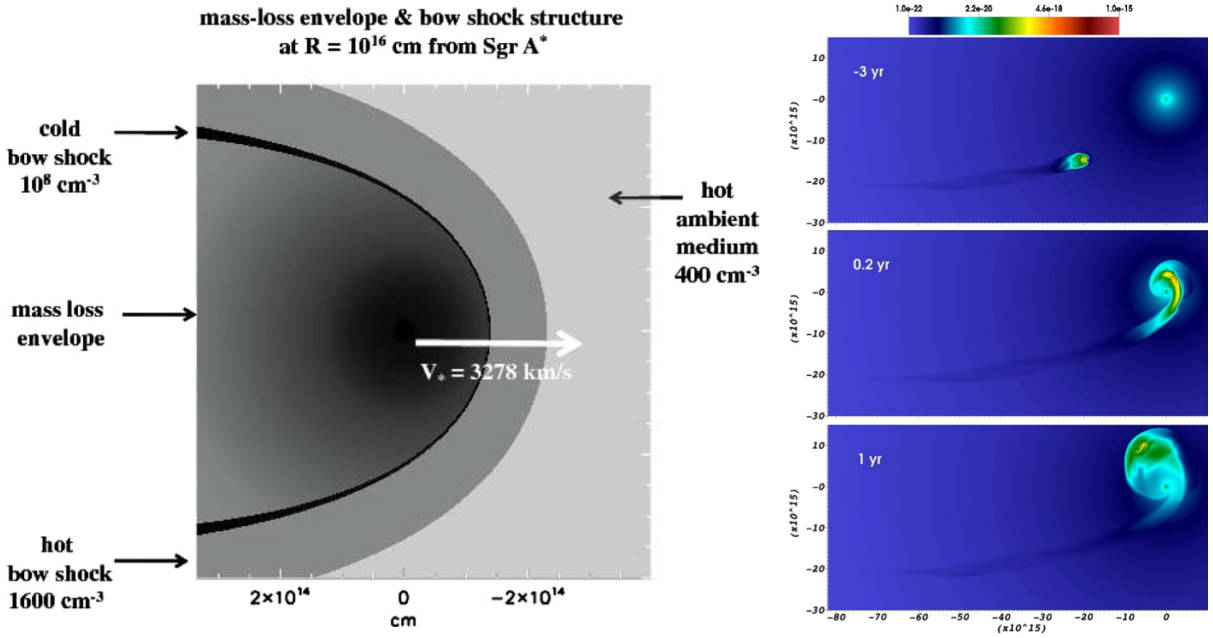

Figure 2.6: Density structure for an outflow from a central source on G2's orbit. Left: results of the analytic calculation in Scoville & Burkert (2013), for a distance of 10^{16} cm from SgrA*. This panel clearly shows the different components of the interacting outflow, as also described in Section 4.1. Right: Density cuts along the orbital plane, for the 3D simulation in De Colle et al. (2014) with the outflow starting 19 yr before pericenter.

happen because of increased mass-loss due to tidal stripping of the central object from the gravitational field of the SMBH, as described by Murray-Clay & Loeb (2012) and Mapelli & Ripamonti (2015). In other cases, a rise in the Brγ luminosity curve is predicted by the interaction with the accretion flow. In these cases most of the luminosity should come from the shocked outflowing material, which should increase its density - hence, its emission measure - as the outflow encounters increasingly high thermal and ram pressures and tidal force in its approach to pericenter (i.e., the same effect present in the hydrodynamical simulations discussed in Sec. 2.2.1). This is a result of all the calculations by Scoville & Burkert (2013), De Colle et al. (2014), Zajaček et al. (2016) (and of those presented in Chapters 5). It must be stressed, however, that such estimates assume that all the material is totally ionized and that there is an ionization-recombination equilibrium. Scoville & Burkert (2013) showed that a constant luminosity can be obtained if the main source of ionization is rather collision of the stellar wind material from the inside, as it crosses the inner shock. In that case, the number of ionizations and the corresponding number of recombinations would be simply proportional to the outflow mass-loss rate, leading to a constant Brγ luminosity if the latter is constant with time.

Consistently with the observations, an increase of the Brγ linewidth is predicted by Zajaček et al. (2016), in the case of a simple analytical bow-shock. In this model, the line

broadening is due the increased velocity spread in the shock, as it encounters higher and higher external ram pressure. However, we will show in Chapter 5 and 6 that the same can be simply obtained by stripping and tidal forces, as the outflow moves along its orbit, as in the case of the diffuse cloud scenario.

As a final remark, Crumley & Kumar (2013) and Zajaček et al. (2016) estimated the radio emission coming from the bow-shock propagating in the external accretion flow. In both cases, the estimated spectra and luminosity curves are well below the detection limits (see blue lines in Fig. 2.5). We must mention that this difference to the previously mentioned estimates by Narayan et al. (2012a) and Sądowski et al. (2013b) has, however, nothing to do with the nature of the source, but simply with the assumed cross section for the objects. In fact, in the work by Crumley & Kumar (2013) and Zajaček et al. (2016) the cross section is calculated through the analytic solution for the bow-shock geometry by Baranov et al. (1971) and it is significantly decreasing as the source moves towards pericenter (similarly to what happens in the simulations presented in this dissertation), while, as mentioned before, the diffuse cloud estimates rely on the assumption of a constant, larger cross section.

Chapter 3

A brief excursus on computational hydrodynamics

Being G2 a gas cloud, it seemed a natural choice to use the hydrodynamical approach to evaluate its evolution, as in the case of many other studies discussed in Chapter 2.

In this chapter we will introduce the equations of hydrodynamics (Sec. 3.1) and we will provide basic notions of the philosophy of grid codes (Sec. 3.2 and 3.3).

3.1 The equations of hydrodynamics

In order to mathematically define the evolution of a fluid, two main approaches can be used, depending on the frame of reference used. In the so-called *Lagrangian* approach, any fluid element is followed in its motion. The frame of reference is then said to be "advected" with the flow of the fluid. In the so-called *Eulerian* approach, instead, the fluid elements are not moving: this means that the equations follow the rate of change of the fluid properties over *control volumes* V_c that are fixed in space. For our hydrodynamic simulations we used the Eulerian grid code PLUTO (Mignone et al., 2007, 2012), so we will focus on the latter approach. The equations of hydrodynamics are a set of partial differential equations (PDEs) that can be expressed as

$$\frac{\partial \mathbf{U}}{\partial t} = -\nabla \cdot \mathbf{T}(\mathbf{U}) + \mathbf{S}(\mathbf{U}) \tag{3.1}$$

where $\mathbf{U}$ is an array of variables, $\mathbf{T}(\mathbf{U})$ is a second order tensor and $\mathbf{S}(\mathbf{U})$ can represent any sink/source term. In the simple hydrodynamic case,

$$\mathbf{U} = \begin{bmatrix} \rho \\ \rho\mathbf{v} \\ E \end{bmatrix}, \mathbf{T}(\mathbf{U}) = \begin{bmatrix} \rho\mathbf{v} \\ \rho\mathbf{v} \otimes \mathbf{v} + P\mathbf{1} \\ (E+P)\mathbf{v} \end{bmatrix}^T \tag{3.2}$$

where ρ is the density, $\mathbf{v}$ is the velocity vector, E is the total energy density, P is the pressure and $\mathbf{1}$ is the 3x3 unit tensor. The equations are actually "closed" by the equation

of state for ideal gases, relating E and P,

$$E = \frac{P}{\gamma - 1} + \frac{|\mathbf{v}|^2}{2\rho}, \tag{3.3}$$

with γ being the gas adiabatic index. Such system of equations can be thought as the conservation laws for mass, momentum and energy. The left hand side is the variation of any of the three quantities in time, within the control volume. The right hand side of the equation expresses the net flux of the respective quantity into or out of the control volume. An exact derivation of this form of the equations requires the use of Reynolds transport theorem and is beyond the purpose of the present dissertation. To understand it one could think, for example, that in any control volume V_c - fixed in space and conserving its volume - the rate of change in mass $\int_{V_c} \rho dV$ must be equal to the net amount of mass flowing into or out of the volume $\int_{S_c} \rho \mathbf{v} \cdot \mathbf{n} dS$, where S_c is the surface enclosing V_c and $\mathbf{n}$ is the versor (field) perpendicular to S_c. The Gauss divergence theorem allows to express the second integral as $\int_{V_c} \nabla \cdot (\rho \mathbf{v}) dV$. The integral disappears in Eq. 3.1 due to the fluid assumption; a "volumetric" conservation law becomes a local one, as long as the control volume V_c can be considered arbitrarily small. We will see in Sec. 3.2 that the idea of thinking about the divergence term of Eq. 3.1 in terms of fluxes across surfaces is fundamental for their numerical solution through the Godunov method.

As mentioned before, $\mathbf{S}(\mathbf{U})$ represents additional sink/source terms. For many astrophysical problems, such term might represent external gravitational forces, energy loss or gain (i.e., cooling or heating) by radiation, local injection of energy and/or momentum by stellar feedback, etc. $\mathbf{U}$, $\mathbf{T}(\mathbf{U})$ and $\mathbf{S}(\mathbf{U})$ can also be adapted to account for the presence of magnetic fields (ideal or non-ideal MHD equations), to include the effects of viscosity (Navier-Stokes equations) or thermal conduction or to extend the equations to a special relativity framework.

3.2 The numerical solution of the equations

3.2.1 The discretization

In order to numerically solve the aforementioned set of equations, a discretization of both the spatial and temporal coordinates must be made. In grid codes, every spatial coordinate is then arranged in a grid of cells, filling the entire computational domain. In the Eulerian framework, every cell is then to be considered as a control volume (as defined in Sec. 3.1). In many codes - such as PLUTO - different orthogonal curvilinear coordinate systems (cartesian, cylindrical, spherical) or different dimensionalities (1,2,3 dimensions) can be chosen, depending on the symmetries of the problem. For example, a planar collision can be approximately studied with 1D cartesian coordinates, a spherically symmetric collapse with 1D spherical coordinates, etc. For the sake of simplicity, the following discussion

of the solution of the equations can be reduced to one dimension[1]. In this case, the i-th grid cell will have its center in x_i and its lower and upper boundaries in $x_{i-1/2}$ and $x_{i+1/2}$, respectively (its width, then, being $\Delta x_i = x_{i+1/2} - x_{i-1/2}$). The mesh spacing can be uniform, but also non uniform (e.g., logarithmically stretched) or "adaptive" (see Sec. 3.3). The temporal coordinate is also divided in a grid. However, in order to guarantee the stability of the numerical solution, the n-th time increment (often called time step, $\Delta t = t_{n+1} - t_n$) must be calculated "on the fly", according to the Courant-Friedrichs-Lewy (CFL) criterion (see Sec. 3.2.2).

3.2.2 The Godunov scheme

The solution of the equation must be numerically obtained through the evaluation of the different terms in the PDEs, given the discretization made. Most of the numerical methods are based on either approximating the derivatives at a specific position in space and/or time (the corresponding family of methods is said to be based on "finite differences") or on considering the integral form of the PDE and its solution in the volume surrounding each position (these methods are of the "finite volume" type)[2]. The numerical solution of the divergence term in the right hand side of Eq. 3.1 is actually based on the second idea, according to the Godunov scheme. As anticipated, in order to give an idea of the basic principles of this scheme, we will reduce our description to one dimension only (with generic variable x). In this case, the divergence term $\partial T(U)/\partial x$ can be represented by the operator

$$L(\mathbf{U}) = \frac{1}{\Delta V}(A_+\mathbf{F}_+ - A_-\mathbf{F}_-), \tag{3.4}$$

where ΔV is the cell "volume" in that direction (i.e., $x_{i+1/2} - x_{i-1/2}$ in the cartesian, $(r^2_{i+1/2} - r^2_{i-1/2})/2$ in cylindrical and $(r^3_{i+1/2} - r^3_{i-1/2})/3$ in the spherical coordinate systems), $A_\pm$ are the right (+) and left (-) interface surfaces (i.e., 1 in the cartesian, $r_{i\pm1/2}$ in cylindrical and $r^2_{i\pm1/2}$ in the spherical coordinate systems)[3] and $\mathbf{F}_\pm$ is an expression for the flux across the right and left interfaces. The computation of $\mathbf{F}_\pm$ consists in providing a solution to the Riemann problem, i.e., finding, for example, $\mathbf{F}_+(x,t)$, given the initial condition

$$\mathbf{F}_+(x,t_0) = \begin{cases} \mathbf{F}_{+,left}, & \text{if } x < x_+, \\ \mathbf{F}_{+,right}, & \text{if } x > x_+, \end{cases} \tag{3.5}$$

[1]This is due to the linearity of the mathematical operators in the equations. Many codes are based on the splitting of the latter in the different dimensions. This might consist, for example, in separating the divergence in its partial derivatives in every coordinate and successively update the solution along the different "directions". Unsplit methods are, however, possible.

[2]In a discretized framework, the control volumes are not arbitrarily small, but have, indeed, a finite volume.

[3]The connection between $A_\pm$ and the Jacobian determinant for the transformation of coordinate systems is evident.

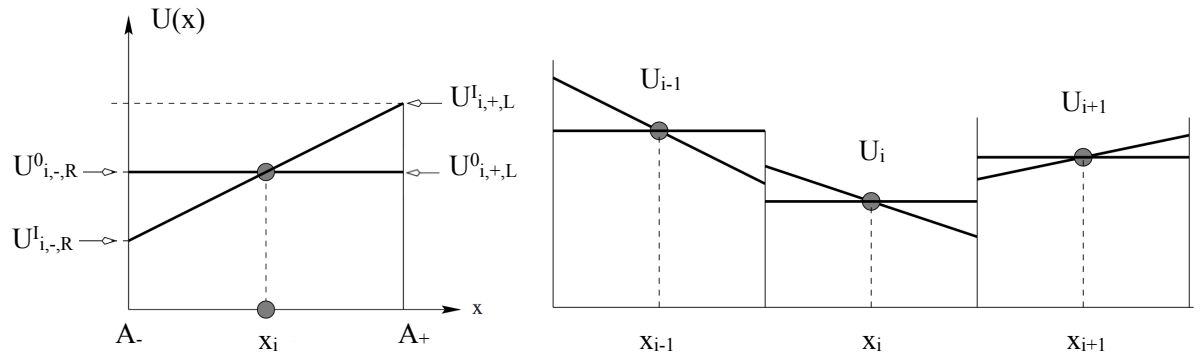

Figure 3.1: Schematic example of a piecewise reconstruction, in a 1D case. Left panel: constant (superscript 0, first-order scheme) and linear (superscript 1, second-order scheme) reconstructions for U, i.e., one of the elements of the conservative array $\mathbf{U}$. The subscript $\pm$ characterize the left and right interfaces of the cell at position x_i, while the subscripts L, R characterize the left and right value of the reconstructed U for any interface. Right panel: constant and linear reconstruction for three consecutive cells at positions x_{i-1}, x_i and x_{i+1}. We can notice the "upwind-bias" of the second-order scheme; in fact, the linear interpolation for the reconstruction of U is based on the most adjacent point on the left, in this case assumed to be the upstream side of the flow. Both panels are taken and adapted from Toro (1997).

where the *left* and *right* subscripts refer to the values of the flux on both sides of the considered interface.

The numerical solution of the Riemann problem requires several steps. First of all, $\mathbf{F}_{left}$ and $\mathbf{F}_{right}$ must be evaluated. This procedure is usally called "reconstruction" (see Fig. 3.1). The simplest possible assumption is that the flux is piecewise constant in every volume. This might mean, for example, that $\mathbf{F}_{+,left}$ can be directly calculated from $\mathbf{U}$ in the considered volume and $\mathbf{F}_{+,right}$ is calculated from $\mathbf{U}$ in the following volume (we remind the reader that the fluxes are basically the elements of $\mathbf{T}(\mathbf{U})$). In this case, the Godunov scheme is first-order. However, the piecewise functional form of $\mathbf{F}_{left}$ and $\mathbf{F}_{right}$ in every cell/volume can be more complex, e.g., linear (second-order schemes), parabolic (third-order schemes), etc. These higher-order functional forms are usually obtained by the interpolation of $\mathbf{U}$ in adjacent volumes, under some limiting procedure to avoid numerical issues (usually called "slope limiting"). Most of the times, such interpolation is also considering the propagation of the flow, i.e., it is somewhat "biased" upon the upstream volumes/cells (if the flow is propagating towards the right, the upstream side is the one on the left): in this case, the scheme is also called "upwind-biased" (see right panel of Fig. 3.1). This need is related to the correct propagation of the information across the computational domain and it is required to ensure the accuracy and stability of the solution. Additionally, a better stability of the solution is also reached by calculating the flux from the *primitive* variables $\mathbf{V} = (\rho, \mathbf{v}, P)^T$, rather than from the *conservative* variables $\mathbf{U}$. The evaluation of the flux

for every cell also urges the definition of $\mathbf{U}$ (or $\mathbf{V}$) in a certain number (depending on the order of the Godunov scheme) of "ghost" cells surrounding the computational domain. This is done through the definition of so-called "boundary conditions" (BCs). Several kind of standard BCs can be defined according to the expected or required properties of the flow and the geometry and symmetries of the problem (typical BCs are outflowing, inflowing, reflecting, periodic, etc.). Anyway, after evaluating $\mathbf{F}_{left}$ and $\mathbf{F}_{right}$ the Riemann problem can be solved to obtain $\mathbf{F}_{\pm}$; however, the exact solution involves the decay of a set of nonlinear waves and it can be hard and computationally expensive. Several approximate methods have been developed to achieve this task, called "Riemann solvers". Reviewing them is beyond the purposes of the present dissertation and we refer to the book by Toro (1997) and, concerning the code PLUTO, to Mignone et al. (2007, 2012).

As correctly pointed out by the recent review by Teyssier (2015), given the amount of approximations involved, any Godunov scheme has some numerical diffusion, essentially due to the overpropagation of certain wave-modes in the numerical solution of the Riemann problem ("advection error"). In general, higher resolution (i.e., smaller cells) can reduce it, but never remove it completely. However, the numerical diffusion often allows the numerical solution to be stable and reduces the impact of certain numerical pathologies (see, e.g., Quirk, 1994). Additionally, no real physical system is totally non-diffusive. So, one can think of numerical diffusion as a representation of various physical diffusion mechanisms on scales equal or smaller than the chosen resolution (e.g., Fierlinger et al., 2016).

The discretization of the left hand side of Eq. 3.1 is usually easier and based on finite differences. The simplest case is the forward Euler discretization, where the time derivative is approximated as

$$\frac{\mathbf{U}_{n+1} - \mathbf{U}_n}{\Delta t}, \tag{3.6}$$

where $\mathbf{U}_n$ is the solution at time t_n. A more sophisticated possibility consists in using the Runge-Kutta (RK) scheme, that is based on successive increment of the solution to reduce the numerical error. For example, the second-order RK scheme updates the solution in the following way:

$$\begin{aligned} \mathbf{U}_* &= \mathbf{U_n} + \Delta t L(\mathbf{U}_n), \\ \mathbf{U_{n+1}} &= \frac{1}{2}(\mathbf{U_n} + \mathbf{U}_* + \Delta t L(\mathbf{U}_*)). \end{aligned} \tag{3.7}$$

As we clarified before, the Godunov schemes (and hydrodynamics) are strongly related to the propagation of waves. Hence, a necessary condition for the stability of the solution is to avoid waves to propagate more than the size of the considered volumes[4]. This is obtained by imposing the CFL condition (Courant et al., 1967)

[4]For a more rigorous discussion about stability of finite difference schemes, such as those used for the temporal evolution, we refer to the von Neumann stability analysis (see Crank et al., 1947; Charney et al., 1950)

$$\Delta t = C_a min\left(\frac{min(\Delta_x)}{|max(w)|}\right), \tag{3.8}$$

where w is any signal velocity (typically, the sound speed c_s of the fluid) and C_a is a constant value smaller than 1, called "Courant number", and it is dependent on the used numerical schemes (however, the smaller, the better for the stability of the solution).

From the previous discussion, it is quite evident that high temporal and spatial resolutions are important ro reduce numerical errors. Additionally, spatial resolution might be needed to ensure the correctness of the solution. For example, slabs, filaments and clumps in the gas can undergo collapse that needs to be properly sampled by the spatial grid. However, higher resolution means a higher number of operations, so it comes with a computational cost. Hence, in certain cases, it might be convenient to adjust the spatial resolution depending on how "critical" a certain region of the computational domain is (see Sec. 3.3.2 for a more explicit definition of what "critical" means).

3.3 The adaptive mesh refinement (AMR)

3.3.1 The strategy

As already mentioned, the most recently developed Eulerian grid codes are equipped with adaptive mesh refinement (AMR) techniques. An adaptive refinement allows the code to focus on and dedicate more computational effort only for regions of the computational domain where numerics or physics require higher spatial resolution. Few different refinement strategies are possible, but we will focus here on describing the "patch-based" strategy used by PLUTO and many other codes[5]. In this case, the refinement is performed "on the fly", at every timestep. First, the solution is calculated and updated in every cell of the initial "coarse" grid; after doing this, the code checks, for every grid cell, whether a certain refinement condition is satisfied. Those cells satisfying the criterion are split in sub-cells and the code then recalculates the numerical solution in the newly constructed "patches" of the domain, where the resolution has been increased. This procedure can be repeated $\eta+1$ times, so that at the end of any "coarse" timestep, a grid with η hierarchic refinement levels is defined (the "coarse" grid is defined to have level equal to 0). The splitting for level l must satisfy the condition $\Delta x_{l+1}/\Delta x_l = r_l$, where r_l is the "refinement ratio" and it must be an integer, so to have cells with equal size in a certain direction. An example is given in the left panel of Fig. 3.2, for a 2D cartesian grid[6], with maximum refinement level $l = 2$ and $r_{1,2} = 2$.

[5]Other popular strategies are the "octree-based" for structured grids or "Delaunay tesselation" or "Voronoi tasselation" for moving grids.

[6]The refinement can in principle be implemented for different coordinate systems and grids other than the cartesian grid.

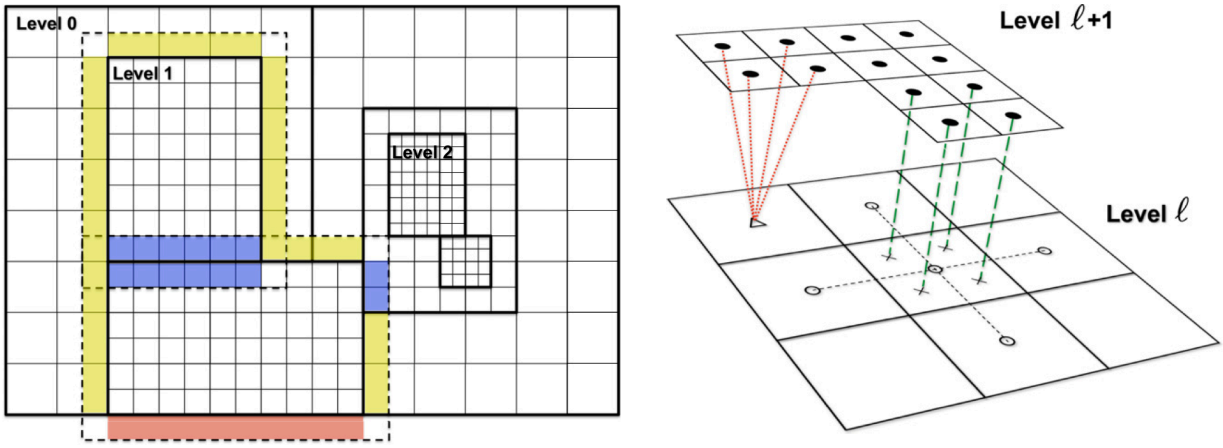

Figure 3.2: Examples of adaptive mesh refinement. Left panel: 2D AMR cartesian grid, with maximum refinement level $l = 2$ and refinement ratios $r_{1,2} = 2$. The colored cells show boundaries for two patches in level 1, with same resolution of the level (blue), lower resolution (yellow) and "ghost" cells outside the computational domain. Right panel: 2D sketch for "prolongation" (green dashed lines) and "restriction" (red dotted lines) operations (see text) between two levels with $r_l = 2$. Both panels are taken from Mignone et al. (2012).

A similar procedure must be followed also for the timestep: in fact, when moving from level l to level $l + 1$, the CFL condition requires that the timestep is also reduced. As a consequence, Δt_l is subdivided in several Δt_{l+1}. However, according to the CFL condition, Δt does not depend on the cell size only, but also on signal velocities (for the simple hydrodynamic case considered here, this velocity is mainly represented by the sound speed). Hence, the ratio $\Delta t_l / \Delta t_{l+1}$ is not necessarily an integer. Time synchronization between all the refinement levels is however ensured by always adding a last small timestep smaller than the CFL one. Of course, at the end of a certain timestep, cells that fulfill the refinement criterion will be resampled and "moved" to the following level, but certain patches might also stop fulfilling the refinement criterion and can be, at that point de-refined. Every refinement and de-refinement requires the variable $\mathbf{U}$ to be assigned to the cells of the new level, through "prolongation" and "restriction" operations, respectively. As shown in the right panel of Fig. 3.2, prolongation (green dashed lines) is usually performed through linear interpolation from surrounding cells of level l (empty circles) - also in this case, with some slope limiting, to avoid artificial local extrema -, so to get new values in the center of the new cells of level $l + 1$ (crosses). In general, restriction (red dotted lines) is instead obtained averaging $\mathbf{U}$ over the cells of level $l + 1$ that are composing the new cell in level l (empty triangle).

3.3.2 Typical refinement criteria

As anticipated in Sec. 3.2, resolution is very important both for numerical and physical reasons. Refinement criteria can then be divided in these two main categories.

Refinement criteria that are concerned with the accuracy usually focus on regions of the computational domain with strong gradients in $\mathbf{U}$. Discontinuities are usually tracing shocks, colliding flows, collapsing regions, etc. From a numerical point of view, discontinuities are the regions accumulating higher errors, due to the discretization and to the nature of the Godunov method (truncation and advection errors). Several refinement criteria are then based on calculating first or second derivatives of $\mathbf{U}$ (or any of its elements), by means of local finite differences with respect to adjacent cells. When the value of the derivative (or of a particular combination of derivatives)[7] is bigger than a certain refinement threshold set by the user, the code refines the cell (the threshold being problem dependent).

A bigger number of refinement criteria are, instead, based on the physical condition of the considered region. The most simple possibilities consist in checking whether any variable becomes higher or lower than a certain threshold value (for example, high density or low temperature/pressure regions might be corresponding to local collapse); similarly, the code might be checking any of the source terms and compare it to some critical value. More sophisticated choices calculate combinations of the variables, in particular some meaningful physical lengthscale (e.g., the Jeans length), compare it to the resolution and refine in order to be able to "resolve" it (according to arguments of the type of the Nyquist sampling criterion). Positional or geometrical criteria might also be implemented, to give a higher resolution to specifically localized (fixed or moving) regions of the domain.

Computational fluid dynamics is a large branch of physics, in the present days. This Chapter was not intended to give an exhaustive explanation of how grid codes work. However, for a review on grid-based hydrodynamics in astrophysics we might refer the reader to the recent article by Teyssier (2015). Nonetheless, we believe this chapter is providing the reader with the fundamental information needed to understand the discussion of the numerical results presented in the next chapters.

[7] One of these criteria, based on the first or second derivative error norm, is implemented in PLUTO.

Chapter 4

The physics of winds in the Galactic Center

In this chapter we provide some qualitative and quantitative considerations, which will be helpful in understanding the structure and evolution of our simulated outflows, as well as their emission properties.

4.1 The structure of winds in high pressure ambient media

When spherical stellar winds interact with the warm gas composing the typical interstellar medium (ISM) ($n_{\rm ISM} \approx 1$ cm^{-3}, $P_{\rm ISM} \approx 10^{-12}$ dyn cm^{-2}), they are well described by the model of Weaver et al. (1977). Their structure consists of a *free-wind region* ((a) in Fig. 4.1), where the wind mass loss rate $\dot{M}_{\rm w}$ and the wind velocity $v_{\rm w}$ are constant with distance from the star (radius) r, so that the gas density

$$\begin{aligned} \rho_{\rm w}(r) &= \frac{\dot{M}_{\rm w}}{4\pi v_{\rm w} r^2} \approx \\ &\approx 4.47 \times 10^{-16} \left(\frac{\dot{M}_{\rm w}}{10^{-7}{\rm M}_\odot/{\rm yr}}\right) \left(\frac{v_{\rm w}}{50 \text{ km/s}}\right)^{-1} \left(\frac{r}{1 \text{ AU}}\right)^{-2} {\rm g \ cm^{-3}} \end{aligned} \tag{4.1}$$

scales with $1/r^2$.

An inner shock (R_1 in Fig. 4.1) is separating the *free-wind region* from a large and almost isobaric region of *shocked stellar wind* ((b) in Fig. 4.1). A contact discontinuity (R_C in Fig. 4.1) separates the wind material from a dense shell of swept-up ambient medium ((c) in Fig. 4.1) whose outer boundary is an external shock (R_2 in Fig. 4.1) propagating into the unperturbed ISM ((d) in Fig. 4.1). After a phase of adiabatic expansion, the thickness of this outer shell reduces and the density increases substantially because radiative cooling occurs in this region on a relatively short timescale.

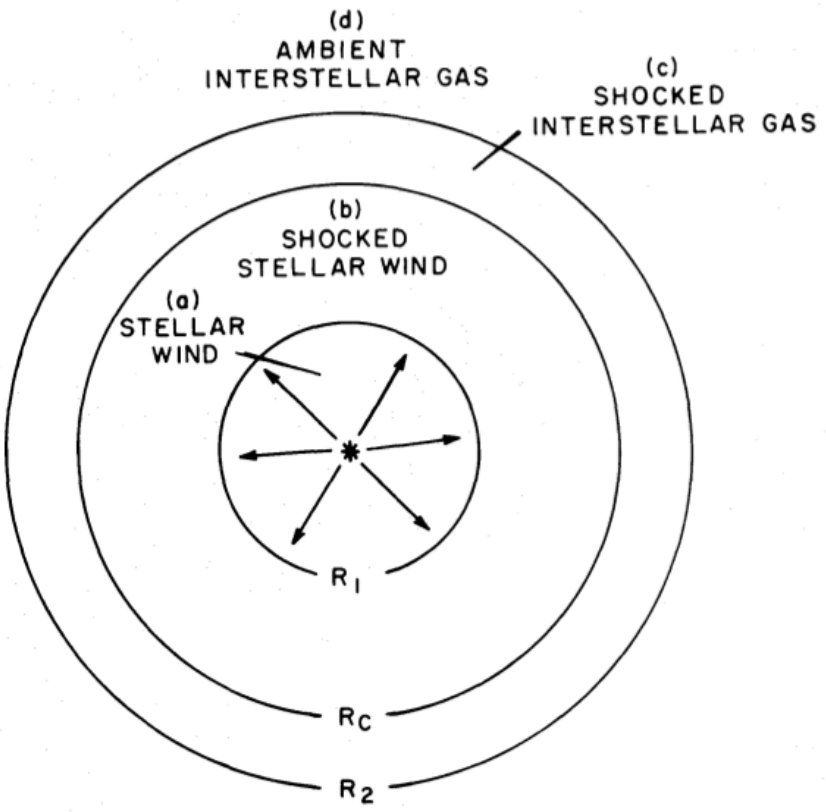

Figure 4.1: Sketch of the structure of typical stellar winds in low pressure ISM (from Weaver et al., 1977).

In our work, the wind interacts with the very hot and dense atmosphere present in the Galactic Center (see Sec. 1.1.3 and Baganoff et al., 2003; Yuan et al., 2003; Xu et al., 2006). This atmosphere has extremely high thermal pressures, ranging from roughly 10^{-7} dyn cm^{-2} at 0.05 pc to roughly 5×10^{-4} dyn cm^{-2} at around 1000 Schwarzschild radii from SgrA* and sound-speed c_s ranging from $\approx$ 500 km/s to $\approx$ 3000 km/s (see profiles in Sec. 2.2). Furthermore, in all the proposed scenarios for G2's origin related to outflows, given G2's observed size and mass, the suggested mass loss rates and velocities are always typical of relatively weak winds (weak in terms of their power, which is given by $L_w = 0.5\dot{M}_w v_w^2$). As a result, the structure of winds in the proximity of Sgr A* is different from that of Weaver et al. (1977).

4.1.1 Weak stellar winds in high pressure media: a 1D study

In order to understand the structure and evolution of G2 as a weak stellar wind from a central source, we performed a series of 1D simulations in spherical coordinate r, to test

the impact of the external pressure on the structure of the outflow. This study required a systematic variation of the different involved parameters, hence the best solution was to just simplify the problem and choose 1D spherical coordinates (neglecting possible processes related to the directional motion of the source or the formation of instabilities that cannot be modeled in one dimension, see sections 2.2 and 4.1.2). Spherical coordinates are the most natural choice to study a spherical outflow. This study was fundamental to guide us to the 2D and 3D simulations described in chapters 5, 6 and 7.

Simulation setup

Simultaneously resolving the size of a star and the dynamics of its wind is currently computationally impossible, since this would involve too many order of magnitudes different physical scales (hence, needing very high resolutions). The usual approach, in astrophysics, is then to define an input region in the computational domain - usually much larger than the size of the source - where the outflow is injected. In many simulations, the outflow is injected in this region as a source term $\mathbf{S}(\mathbf{U})$ (see Sec. 3.1); most of the time, the mechanical luminosity of the outflow is injected in the input region as internal energy. In this approach, the hotter input material has an accelerated expansion until the velocity converges to a terminal velocity, with its geometrical dilution (see, e.g., Rozyczka, 1985). In this case, the calculation of the source term is quite straightforward as long as the pressure of the external medium is negligible compared to the ram pressure of the outflow. If this is true, the terminal velocity is reached quickly and a stationary wind, with basically constant velocity, is set at very small distances from the input region. However, as discussed in Sec 2.2, G2 is interacting with a high pressure external medium. We then preferred to follow another approach, consisting in resetting $\mathbf{U}$, and specifically its density and velocity, in the input region (for a similar approach, see, e.g., Falle, 1975). Though this approach is qualitatively equivalent to the previous one, it is somewhat conceptually different: in this case, in fact, we have an injection of momentum, rather than of internal energy and, given the resetting of $\mathbf{U}$, the input region is rather to be considered as a "boundary region" of the computational domain. In this case, the outflow is injected from an inner boundary with radius $r_{\rm inb}$ with a constant velocity $v_{\rm w}$ and density $\rho_{\rm w}$ set to satisfy

$$\dot{M}_{\rm w} = 4\pi r_{\rm inb}^2 \rho_{\rm w} v_{\rm w}. \tag{4.2}$$

In particular, the models in Fig. 4.2 and 4.4 have $r_{\rm inb} = 2.1 \times 10^{14}$ cm and a resolution of $\Delta r = 3 \times 10^{12}$ cm, while those in Fig. 4.3 and 4.5 have an inner boundary of $r_{\rm inb} = 5 \times 10^{15}$ cm and a resolution of $\Delta r = 3.3 \times 10^{14}$ cm. The equation of state is adiabatic, with an adiabatic index of $\Gamma = 5/3$.

Results

Fig. 4.2 shows the one dimensional density profiles of three models with $\dot{M}_{\rm w} = 10^{-7} {\rm M}_\odot$ yr^{-1} and $v_{\rm w} = 10, 50, 100$ km s^{-1}, expanding in a surrounding medium with thermal pressure $P_{\rm amb} = 10^{-7}$dyn cm^{-2}. As in the classic model of Weaver et al. (1977), our winds have

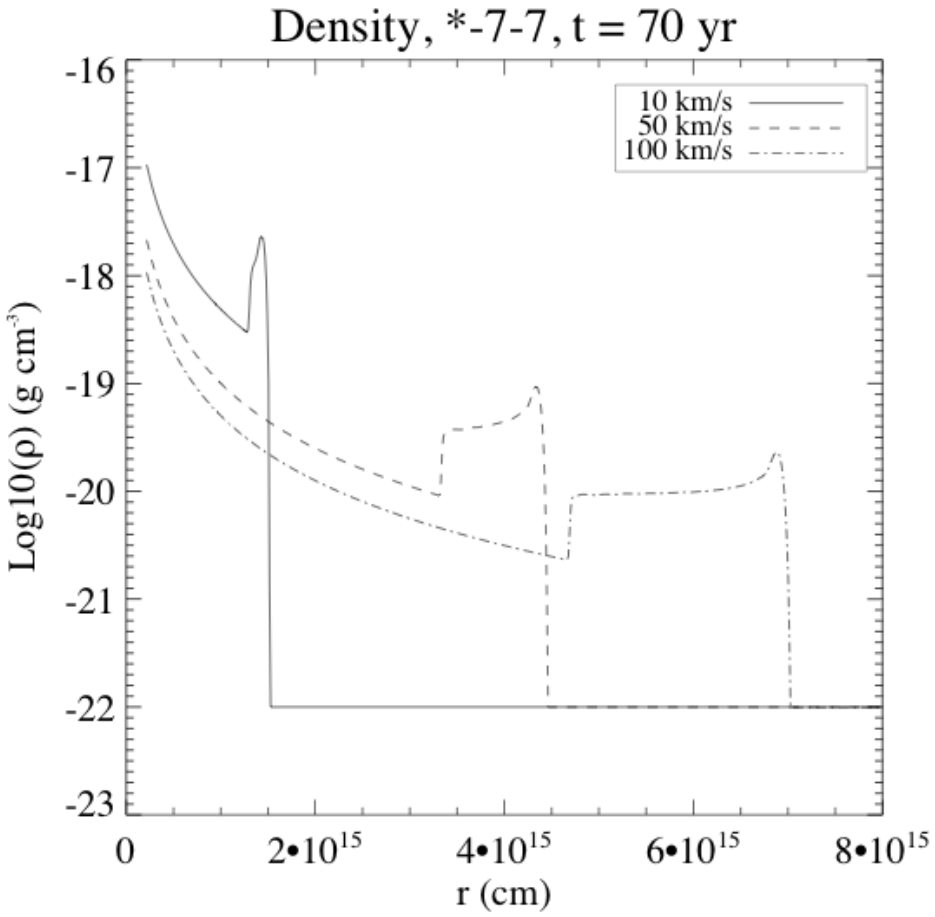

Figure 4.2: Density profiles, after 70 yr of evolution, for our 1D models with $\dot{M}_{\rm w} = 10^{-7} {\rm M}_{\odot}\ {\rm yr}^{-1}$ and $v_{\rm w} = 10, 50, 100\ {\rm km\,s}^{-1}$ (solid, dashed and dash-dotted lines, respectively), expanding in an ambient medium with thermal pressure $P_{\rm amb} = 10^{-7}$ dyn cm^{-2}.

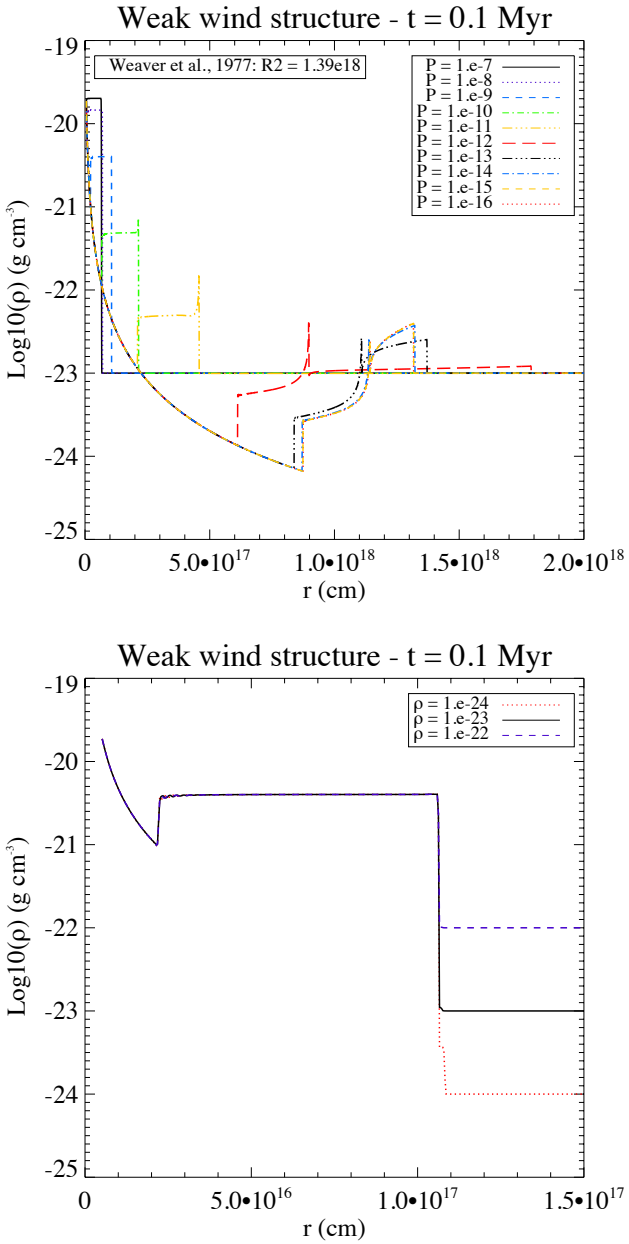

Figure 4.3: Effect of the external pressure on the wind structure. Upper panel: density profiles, after 0.1 Myr, for a series of 1D simulations of a stellar wind with $\dot{M}_{\rm w} = 10^{-7} {\rm M}_{\odot}$ yr^{-1} and $v_{\rm w} = 10$ km s^{-1}. The external pressure for each model varies by one order of magnitude, from 10^{-16} to 10^{-7} dyn cm^{-2} (see legend), while the external density is fixed to 10^{-23} g cm^{-3}. The structure of our models converges for very low pressures. Lower panel: density profile, after 0.1 Myr for the same wind parameters as in the left panel and $P_{\rm amb} = 10^{-9}$ dyn cm^{-2}. The external density is $\rho_{\rm amb} = 10^{-24}, 10^{-23}, 10^{-22}$ g cm^{-3} (red dotted, black solid and blue dashed lines, respectively). For this high pressure, the structure of the wind is just set by the latter and it is unaffected by the external density.

a *free-wind region*, with density scaling as $1/r^2$ (see Eq. 4.1), and an inner shock separating it from the shocked wind material. This inner shock reaches its *stagnation radius* $r_{\rm stag}$ when the wind ram pressure $\rho(r)v_{\rm w}^2$ becomes equal to the external ambient medium pressure $P_{\rm amb}$, so

$$\begin{aligned} r_{\rm stag} &= \sqrt{\frac{\dot{M}_{\rm w} v_{\rm w}}{4\pi P_{\rm amb}}} \approx \\ &\approx 6.3\times10^{13} \left(\frac{\dot{M}_{\rm w}}{10^{-7}{\rm M}_\odot/{\rm yr}}\right)^{1/2} \left(\frac{v_{\rm w}}{50\ {\rm km/s}}\right)^{1/2} \left(\frac{P_{\rm amb}}{6.2\times10^{-4}{\rm dyn/cm^2}}\right)^{-1/2} {\rm cm}, \end{aligned} \tag{4.3}$$

where "standard" values for the wind parameters (see Chapter 5 and 6) and a reference value for the hot environment thermal pressure at G2's pericenter are adopted. Due to the high pressure, the stagnation radius is very small and the *shocked wind* material forms a dense shell. Another main difference with respect to the classic wind structure is that the considered winds have subsonic expansion velocities. Hence, in the ideal case of a source at rest, in addition to the dense wind shell a very weak sound wave propagates outward, with no significant reaction of the ambient medium on the wind.

In Fig. 4.3 the effect of the external thermal pressure on the structure of the wind is visible. In the left panel, a model with $\dot{M}_{\rm w} = 10^{-7}{\rm M}_\odot\ {\rm yr}^{-1}$ and $v_{\rm w} = 10\ {\rm km\,s}^{-1}$ has been evolved for 0.1 Myr in different $P_{\rm amb}$ ranging from 10^{-16} to 10^{-7} dyn cm^{-2}. This figure nicely shows the effect of $P_{\rm amb}$ on the inner shock $R_1 = r_{\rm stag}$ and on the contact discontinuity R_C. Eq. 4.3 is strictly valid only for high pressures and, indeed, the position of the inner shock and of the contact discontinuity does not depend on the density of the ambient medium (see lower panel of Fig. 4.3). However, when the external pressure decreases, the structure gets instead independent of the outer pressure: an outer shock $R_{2,\rm lpr}$ forms, with distance from the source

$$R_{2,\rm lpr}(t) \propto (L_{\rm w}/\rho_{\rm amb})^{1/5} t^{3/5} \tag{4.4}$$

(see Weaver et al., 1977), where $L_{\rm w}$ is again the wind mechanical luminosity. The position of the contact discontinuity, for the case of negligible external pressure, is simply $R_{\rm C,lpr} = 0.86 R_{2,\rm lpr}$ (Weaver et al., 1977).

As already mentioned, in the case of high external pressure, no outer shell of shocked ambient medium forms and $R_{\rm C,hpr}$ sets the outer boundary of the wind structure. In such extreme cases, the evolution of $R_{1,\rm hpr}$ and $R_{\rm C,hpr}$ is easily understandable for the adiabatic case. In fact, as shown in Fig. 4.4, $R_{1,\rm hpr}$ stalls when the wind ram pressure equals the external thermal pressure (see Eq. 4.3). After the stalling of $R_{1,\rm hpr}$, the evolution of $R_{\rm C,hpr}$ - when there are no radiative energy losses - can be understood by assuming that all the mechanical luminosity of the wind is converted, across $R_{1,\rm hpr}$, in internal energy of the dense shocked wind. I.e.,

$$L_{\rm w} = \frac{1}{2}\dot{M}_{\rm w} v_{\rm w}^2 \approx 4\pi P_{\rm amb} R_{\rm C,hpr}^2 \dot{R}_{\rm C,hpr}, \tag{4.5}$$

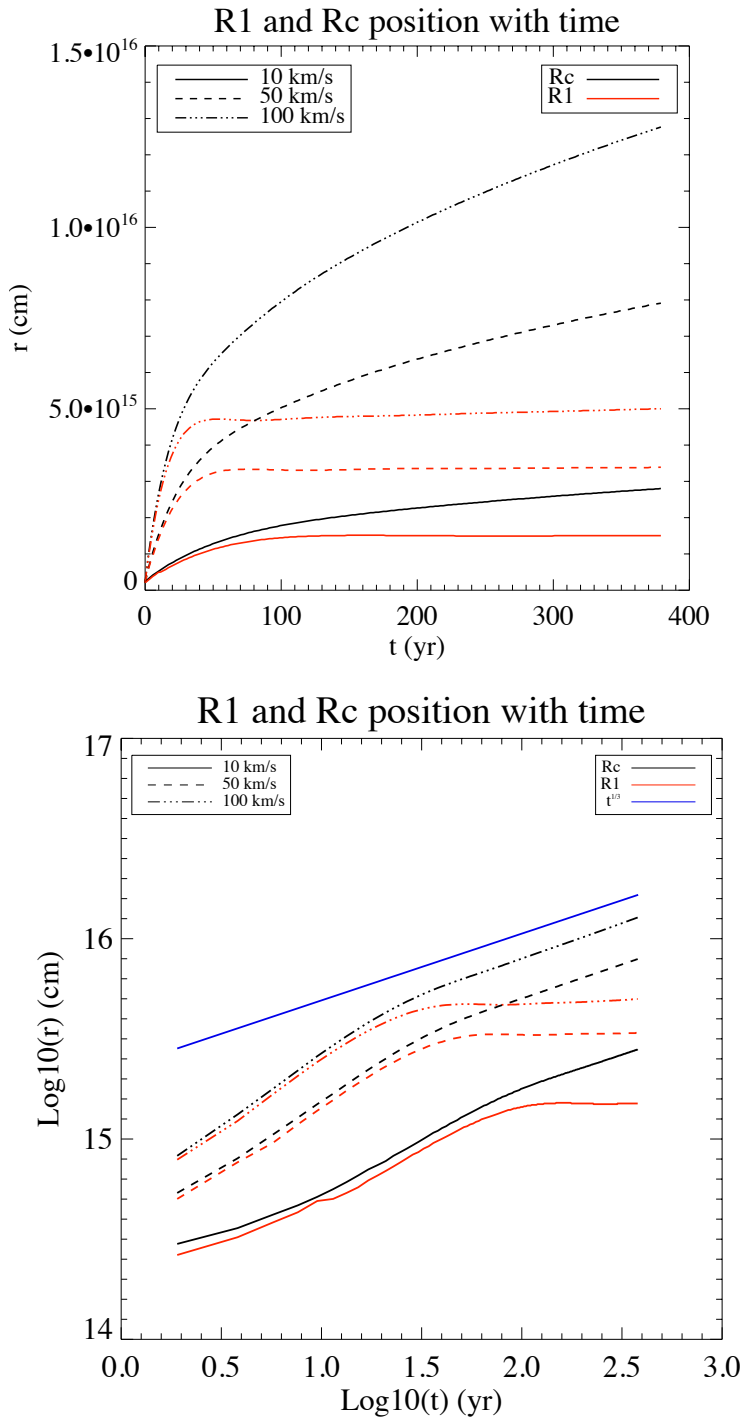

Figure 4.4: Upper panel: Time evolution of the inner shock ($R_{1,\rm hpr}$) and the contact discontinuity ($R_{\rm C,hpr}$) for our 1D models with $\dot{M}_{\rm w} = 10^{-7} {\rm M}_{\odot}$ yr^{-1} and $v_{\rm w} = 10, 50, 100$ km s^{-1}), expanding in an ambient medium with thermal pressure $P_{\rm amb} = 10^{-7}$ dyn cm^{-2}. Lower panel: same as the left panel, but in logarithmic scale. A $R \propto t^{1/3}$ (blue solid) line is overplotted for reference.

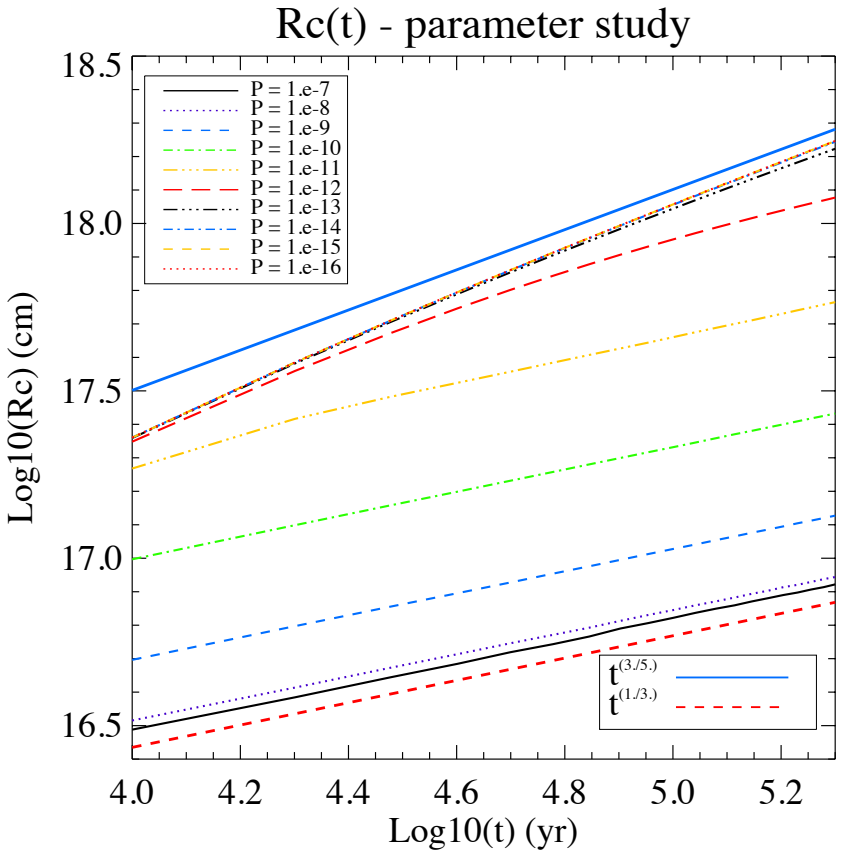

Figure 4.5: Time evolution of the contact discontinuity ($R_{\rm C,hpr}$) for our 1D models with different $P_{\rm amb}$ (same as in Fig. 4.3, see legend). A $R \propto t^{1/3}$ (blue solid) and a $R \propto t^{3/5}$ (red short-dashed) lines are overplotted for reference.

and $R_{\rm C,hpr} \propto t^{1/3}$, as already shown by Parker (1963) (see right panel of Fig. 4.4). The transition between the two regimes $R_{\rm C,lpr} \propto t^{3/5}$ and $R_{\rm C,hpr} \propto t^{1/3}$ is also shown in Fig. 4.5, showing the time evolution of R_C for all the models in the left panel of Fig. 4.3.

We must, however, stress that when the outer pressure is very high, the shell of shocked wind material is very dense and this leads its radiative cooling to become very efficient. The shell should then rapidly lose its internal energy and become very thin. Hence, the evolution of $R_{\rm C,hpr}$ predicted by Eq. 4.5 is not anymore realistic. Still, the present study is of theoretical interest, since it clarifies what different physical mechanisms are involved in the evolution of winds expanding in extremely high pressure ambient media, as in the case of the accretion flow in the inner parsec of the Milky Way.

4.1.2 Other relevant physical processes

When considering the case of a wind moving on an orbit similar to G2's, further processes are effecting its structure, that are not captured by the simple simulations described in the previous Sec. 4.1.1 and that could be visible in the 2D and 3D simulations described in chapters 5 and 6.

For example, when the motion of the outflow, with respect to the external medium, is considered, its orbital velocity $\vec{v}_*$ must be added to the expansion velocity. This means that when the source moves faster than the sound speed $c_{\rm s,atm}$ of the outer medium, the outflow becomes supersonic in its leading part, even for very low $v_{\rm w}$. This might be the case for G2, particularly close to pericenter (see Fig. 5.1 and Burkert et al., 2012; Scoville & Burkert, 2013). Hence, in this case, a bow shock might form in the front part of the outflow, with Mach number $M = (v_{\rm w} + |\vec{v}_*|)/c_{\rm s,atm}$.

The motion of the outflow also gives an additional "non-thermal" contribution to $P_{\rm amb}$ in Eq. 4.3, with a different intensity depending on the angle $\theta = \arcsin(\vec{v}_{\rm w}/\vec{v}_*)$. For the relatively high densities expected for the accretion flow around G2 (see Eq. 2.7 and, e.g., Burkert et al., 2012), such a ram pressure $\approx \rho_{\rm amb} v_*^2$ might also lead to significant stripping of the outer layers of the outflow, as described in more detail in chapter 7.

It is also worth to mention that the dense *shocked wind* shell is strongly subject to the Rayleigh-Taylor instability (RTI). In fact, in the frame of reference of the contact discontinuity between the wind material and the hot atmosphere, there is a static dense medium (the *shocked wind* shell) and a lighter one (the atmosphere) accelerated towards it. According to linear stability analysis, the Rayleigh-Taylor instability grows exponentially with time as $\exp(t/\tau)$, where $\tau = (Aak)^{-1/2}$. $A = (\rho_h - \rho_l)/(\rho_h + \rho_l)$ is the Atwood number (and ρ_h and ρ_l are the densities of the heavier and lighter media, respectively), a is the acceleration perpendicular to the layer separating the two fluids and $k = 2\pi/l$ is the wavenumber of the perturbation. Taking values from our 1D model with $\dot{M}_{\rm w} = 10^{-7} {\rm M}_\odot\ {\rm yr}^{-1}$, $v_{\rm w} = 50\ {\rm km\,s^{-1}}$, $P_{\rm amb} = 10^{-7}$ dyn cm^{-2} and $\rho_{\rm amb} = 10^{-22}$ g cm^{-3} - somewhat representatives of the parameters considered in chapters 5 and 6 -, and assuming that the dominant wavenumber k is set by l equal to the width of the *shocked wind* shell, we performed a order-of-magnitude estimate. This shows that τ is ≈ 0.3 yr, i.e., roughly three orders of magnitude smaller than G2's orbital period (i.e., 400 yr) and almost always smaller than the free-fall time (see Sec. 2.2). The 2D and 3D simulations will indeed show that the shocked material is very unstable.

Finally, one should also consider the effect of the strong gravity G2 is subject to. In fact, near G2's closest approach to the SMBH, the tidal force becomes dominant (see Sec. 2.2). The tidal force further modifies Eq. 4.3 and it leads to the stretching of the shocked wind material, dramatically effecting the global structure of the outflow near G2's pericenter.

In summary, the shape of stellar winds changes significantly when these are located in a high-pressure environment. Some further remarks about the present discussion can be

found in chapters 5 and 6, as well as in Parker (1963), Koo & McKee (1992), van Marle et al. (2006), Christie et al. (2016), and Ballone et al. (2013, 2016).

4.2 Ionization of the outflow

In this section we try to make a very crude estimate of the contribution of the free-flowing region to the total luminosity of any wind in the Galactic Center. The following calculation is based on the assumption that the ionization of the gas is entirely due to UV photons from the nearby young stars (see Sec. 2.1 and Gillessen et al., 2012). Unfortunately, the flux of ionizing photons reaching G2 is not well known, so we decided to stick to a very simplified analytical calculation, which is mainly intended to show how the contribution of the free-flowing region can be severely dependent on the different assumptions. A more realistic answer requires the full integration of radiation in the hydrodynamical simulation. However, the current simulations were already extremely time consuming and a further coupling with a radiative transfer scheme would make them unfeasible.

The derivation is based on equating the rate of UV ionizing (Lyman continuum) photons isotropically penetrating a spherical ("naked" free-flowing) region, whose density scales as $1/r^2$, to the rate of recombinations occurring within the latter. This is, of course, a very rough approximation, given the anisotropic nature of the flux of ionizing photons, emitted by the young stars surrounding G2, and of the pressure contributions (particularly the ram and tidal ones) shaping the free-wind region (for a discussion of the physics of stellar winds in the Galactic Center, see Sec. 4.1). The inferred equation is

$$\phi \left(\frac{R_{\rm out}}{D} \right)^2 \approx \int_{R_{\rm in}}^{R_{\rm out}} \alpha_{\rm rec} n_{\rm e} n_{\rm i} 4\pi r^2 dr \tag{4.6}$$

where ϕ is the rate of emitted ionizing photons and D is the distance of G2 from the ionizing source. However, the value of these two latter quantities is not very well constrained and one must assume there is more than one emitting source. In the following, $\phi/4\pi D^2$ will simply be the flux of ionizing photons on G2 and we will consider different numbers used in previous calculations by different authors. $R_{\rm out}$ and $R_{\rm in}$ are respectively the outer and inner radius of the ionized volume of the spherical region. $\alpha_{\rm rec}$ is the total recombination coefficient and we assumed $\alpha_{\rm rec} = 2.59 \times 10^{-13}$ cm^{3}s^{-1}, i.e. the value for case B recombination for pure hydrogen at $T = 10^4$ K (Osterbrock & Ferland, 2006, page 22). $n_{\rm e}$ and $n_{\rm i}$ are the number densities of the electrons and ions - respectively - in the gas and r is the distance from the source. For a $1/r^2$ density profile,

$$n_{\rm e} n_{\rm i} \approx \frac{\rho^2}{\mu_{\rm e}\mu_{\rm i} m_{\rm H}^2} \approx \frac{\dot{M}_{\rm w}^2}{16\pi^2 v_{\rm w}^2 \mu_{\rm e}\mu_{\rm i} m_{\rm H}^2 r^4}, \tag{4.7}$$

where $\dot{M}_{\rm w}$ and $v_{\rm w}$ are the mass-loss rate and velocity of the wind, respectively, $\mu_{\rm e} = 1.17$ and $\mu_{\rm i} = 1.29$ are the electron and ion mean weight (for solar metallicity) and $m_{\rm H}$ is the hydrogen mass.

So, substituting $n_e n_i$ in Eq. 4.6 and solving the integral, we can get the inner radius R_{in} for which there is a balance between the rate of incoming ionizing photons and the rate of recombinations:

$$R_{in} = \left[\frac{\phi}{D^2} \frac{4\pi v_w^2 \mu_e \mu_i m_H^2 R_{out}^2}{\alpha_{rec} \dot{M}_w^2} + \frac{1}{R_{out}} \right]^{-1}. \tag{4.8}$$

We then assume that the outer radius R_{out} is just the stagnation radius given by the atmosphere's thermal pressure only (we hence neglect any anisotropic pressure contributions)

$$R_{out} = \left[\frac{\dot{M}_w v_w}{4\pi P_{amb}} \right]^{1/2}. \tag{4.9}$$

Substituting Eq. 4.9 in Eq. 4.8, we get

$$R_{in} = \left[\frac{\phi}{D^2} \frac{v_w^3 \mu_e \mu_i m_H^2}{\alpha_{rec} \dot{M}_w P_{amb}} + \left(\frac{4\pi P_{amb}}{\dot{M}_w v_w} \right)^{1/2} \right]^{-1}. \tag{4.10}$$

For typical assumptions on the density and temperature of the atmosphere (see, e.g., Burkert et al., 2012, and Eq. 2.7 and 2.8), the ambient pressure varies with radius and so do the inner and outer radii:

$$\begin{aligned} R_{in} \approx 3 \times 10^{15} \Bigg[& 1.691 \times 10^{-2} \frac{\phi_{50}}{D_{pc}^2} \frac{v_{w,50}^3 d_{BH,peri}^2}{\dot{M}_{w,-7}} + \\ & + 44.099 \left(\frac{1}{\dot{M}_{w,-7} v_{w,50}} \right)^{1/2} \frac{1}{d_{BH,peri}} \Bigg]^{-1} \text{cm}, \end{aligned} \tag{4.11}$$

where we expressed the rate of ionizing photons in units of 10^{50} s^{-1}, D in units of pc, the wind's mass-loss rate $\dot{M}_w$ in units of 10^{-7} $M_\odot$ yr^{-1}, its velocity v_w in units of 50 km s^{-1} and the distance from SgrA* $d_{BH,peri}$ in units of the pericenter distance.

We performed the calculation for $v_w = 50$ km s^{-1} and $\dot{M}_w = 10^{-7}, 10^{-6}$ $M_\odot$yr^{-1}, assuming five different fluxes of UV photons:

- In the first case, which we will call **SB**, we assumed the numbers used by Scoville & Burkert (2013), i.e. $\phi_{50} = 1$ and $D_{pc} = 1$. This assumption is equivalent to having a single O5 star at a constant distance of 1 pc.

- In the second case, **MLlow**, we took numbers from Murray-Clay & Loeb (2012) for the entire central parsec; these numbers are (more or less) matching the values provided in Martins et al. (2007) and Genzel et al. (2010). In particular, they assume $\phi_{50} = 10^{0.8} \simeq 6.31$ for $D_{pc} = 1$. This is a lower estimate for the UV flux given by these authors.

- Murray-Clay & Loeb (2012) also took into account the concentration of the S-stars (of spectral class B) within the very central region of the Galactic Center. They estimate these stars to produce a total $\phi_{50} = 0.2$, but for a region of $D_{\rm pc} \simeq 6 \times 10^{-3}$. This is their higher estimate and and we refer to it as **MLhigh**.

- In the fourth case, **Sh04**, we assumed the flux used by Shcherbakov (2014) for the position of the cloud in the year 2004. We consider the values derived by this author as the most reasonable ones, since they are obtained calculating the contribution of the main Wolf-Rayet stars in the young cluster, exactly taking into account their positions, from Paumard et al. (2006) and Lu et al. (2009), and their temperatures and luminosities, from Martins et al. (2007). In 2004, $F_{\rm UV} = 3 \times 10^4$ erg s^{-1} cm^{-2}. If we crudely divide this value by the ionization energy of the hydrogen atom, we get the number flux of ionizing photons $\phi_{50}/D^2_{\rm pc} \simeq 131$.

- In the last case, **Sh14**, we assumed the flux assumed by Shcherbakov (2014) at G2's pericenter, namely $F_{\rm UV} = 5.7 \times 10^4$ erg s^{-1} cm^{-2}. Close to pericenter, the flux increases due to the contribution of the S2 star. Dividing by the ionization energy of the hydrogen atom, we get $\phi_{50}/D^2_{\rm pc} \simeq 249$.

In Fig. 4.6 we plot the results of our simple analytical calculation. As visible in the central panel, the size of $R_{\rm in}$ first increases with G2 getting closer to SgrA* and then decreases at smaller distances. This is the result of two competing effects, i.e. the decrease of available ionizing photons and the increasing density (and number of recombinations) in the outer layer of the free-wind region with the shrinking of the stagnation radius. These two different branches are mathematically visible in Eq. 4.8 and 4.11, as asymptotic branches $\propto R_{\rm out}^{-2} \propto d_{\rm BH}^{-2}$ for large distances and $\propto R_{\rm out} \propto d_{\rm BH}$ for small ones (see also the upper panel in Fig. 4.6). It is also interesting to note that the transition between these two branches moves to larger values of $d_{\rm BH}$ for smaller values of ϕ/D^2. On the other hand, the lower panel of Fig. 4.6 shows that the Brγ luminosity is a monotonic function of $R_{\rm out}$ and $d_{\rm BH}$. This is easily understandable from Eq. 4.6: as the Brγ luminosity is directly proportional to the number of recombinations (i.e., the right hand side of the equation), it is also $\propto R^2_{\rm out}$.

We must stress, again, that this is a very crude analytical estimate. We completely neglect the role of shielding due to the dense shocked material around the free-wind region; this can lead to substantially lower ionization in the free-wind region. Furthermore, the flux of ionizing photons on G2 will certainly not be isotropical, but dependent on the position of the different sources of UV photons (i.e., the stars). Moreover, the spherical approximation for the shape of the free-wind region does not hold close to pericenter, where the tidal and ram contributions to the pressure are making it highly asymmetric (see Sec. 4.1 and cha. Finally, other physical processes could be important as well, e.g. collisional ionization from the wind (as already shown by Scoville & Burkert, 2013).

Another issue is related to the assumption of having an equilibrium between ionizations and recombinations. However, as shown in Mapelli & Ripamonti (2015), the timescales for these two processes might be very different. In our case, the recombination timescale is

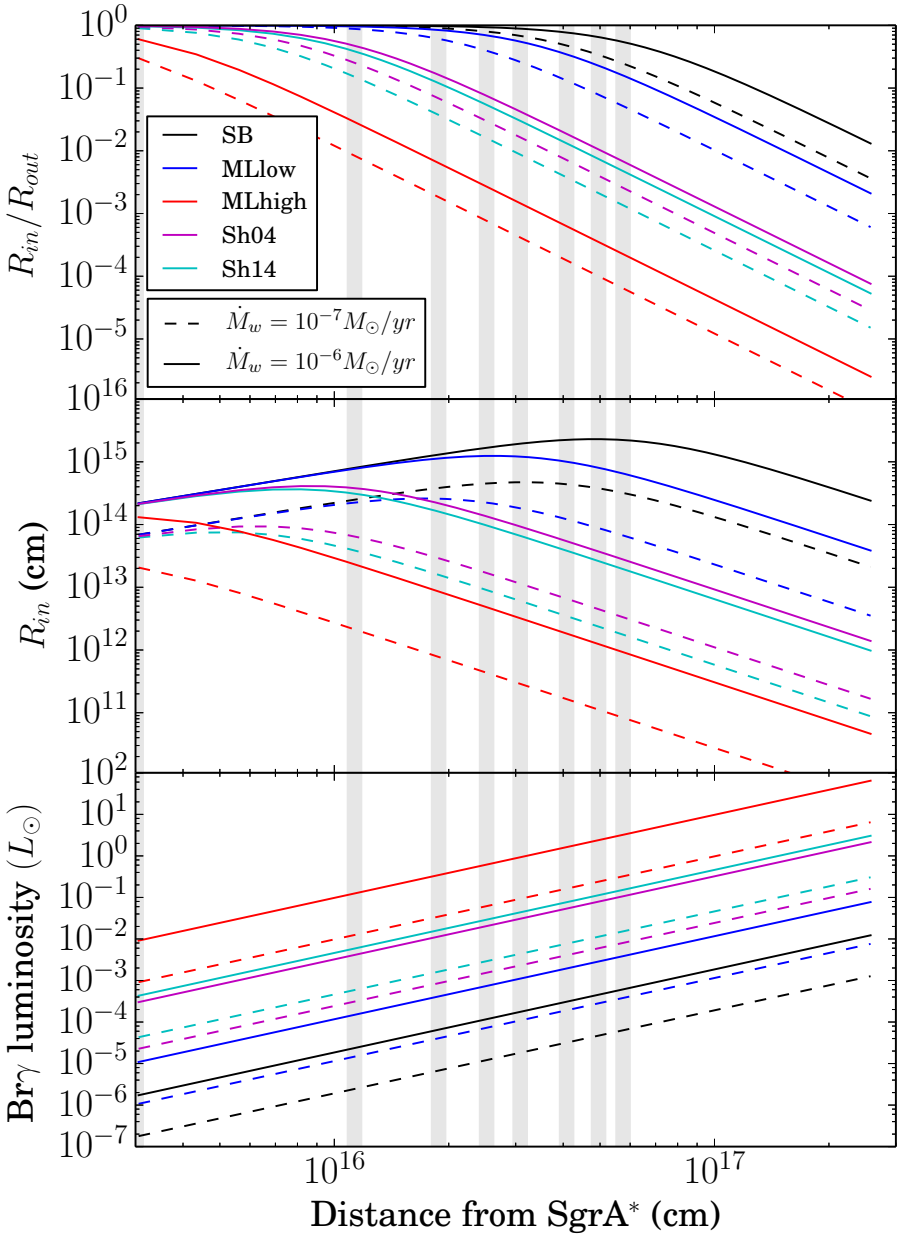

Figure 4.6: Results of our analytical calculation for the ionization of the free-wind region discussed in Sec. 4.2. The upper panel shows the ratio between the inner ($R_{\rm in}$) and outer ($R_{\rm out}$) radii of the ionized shell, while the central panel shows the absolute value of the inner radius. The luminosity of the spherical free-flowing ionized shell is plotted in the lower panel. The dashed and solid lines show the results for $\dot{M}_{\rm w} = 10^{-7}, 10^{-6}\ M_\odot\ {\rm yr}^{-1}$, respectively (the wind velocity is $v_{\rm w} = 50{\rm km\ s}^{-1}$ for both calculations). Different colors show the results for different assumptions on the flux of ionizing photons in the Galactic Center: $(\phi/D^2)_{\rm SB} = 1$, $(\phi/D^2)_{\rm MLlow} = 6.31$, $(\phi/D^2)_{\rm Sh04} = 131$, $(\phi/D^2)_{\rm Sh14} = 249$, $(\phi/D^2)_{\rm MLhigh} = 5560$.

$$t_{\rm rec}(r) = \frac{1}{\alpha_{\rm rec} n_{\rm i}(r)} \approx 5 \times 10^5 \frac{r_{14}^2 v_{\rm w,50}}{\dot{M}_{\rm w,-7}} \text{ s}, \tag{4.12}$$

where r_{14} is r in units of 10^{14} cm. The ionization timescale is

$$t_{\rm ion} = \frac{4\pi D^2}{\sigma_{\rm H} \phi} \approx 2 \times 10^5 \frac{D_{\rm pc}^2}{\phi_{50}} \text{ s}, \tag{4.13}$$

where $\sigma_{\rm H} \simeq 6.3 \times 10^{-18}$ cm^2 is the cross section for neutral hydrogen and photons with energy 13.6 eV. An equilibrium between ionizations and recombinations can be assumed if $t_{\rm rec} < t_{\rm ion}$, which does not always hold for our assumptions.

Hence, the main goal of the present paragraph is to show that the contribution of the free wind region is very sensitive to the actual ionization process and that the huge variety of assumptions in literature can provide extremely different results.

Chapter 5

2D high resolution simulations of the "compact source scenario"

In this chapter we will present a first set of 2D simulations of an outflow moving along G2's orbit. With this study, we investigated its structure and observational properties as a result of the interaction with a hot atmosphere and the extreme gravitational field of the SMBH in the Galactic Center. For this model, we have been inspired by the "compact source" scenario suggested and studied by other authors (see Sec. 2.2.2).

A 2D grid allows to study processes that cannot be captured in 1D (see Sec. 4.1), but still with considerably high resolutions and a uniform grid. They hence managed to give us a first estimate of the possible mass loss rate $\dot{M}_{\rm w}$ and velocity $v_{\rm w}$ that the outflow must have to reproduce some basic G2's observational properties, namely its size and luminosity. This work represented the first study attempting detailed hydrodynamical simulations for the compact source scenario and trying to span the wind's mass loss rate and velocity parameter space.

In section 5.1 we will give some details about the simulation setup. In subsection 5.2.1 we will present our standard model, discussing its evolution and main features and comparing it with the observations. In subsections 5.2.2 and 5.2.3 we will discuss how the results change when varying the outflow velocity and mass loss rate, respectively. A discussion can be found in section 5.3. The chapter is an adaptation of Ballone et al. (2013), published in *The Astrophysical Journal*.

5.1 Simulation setup

For the simulations discussed in this chapter, 2D cylindrical coordinates are adopted. This choice allowed us to reach relatively high resolution on a uniformly spaced grid. As we will show in Sec. 5.2.1, the structure of the emitting material is highly filamentary, which forced us to use resolutions that are roughly a factor of 10 higher compared with the 2D simulations for the diffuse cloud scenario in Schartmann et al. (2012). A 2D domain also

allowed us to simulate both the isotropic expansion of the wind and the motion of the source on its orbit, without the need of a more computationally expensive 3D simulation. The symmetry of the coordinates makes the dynamics of the outflow correct, through the right definition of $A_{\pm}$ and ΔV in Eq. 3.4 (this would not be the case, e.g., in 2D cartesian coordinates). In this case, reflective boundaries are required on the axis of symmetry, i.e., every quantity adjacent to it must be mirrored with respect to the axis (i.e., density and energy are copied; the velocity is copied, but with reversed sign). Unfortunately, this procedure also led us to slightly simplify our problem, assuming a zero angular momentum orbit. This restriction is not extremely severe, since the observed orbit has a very high eccentricity; $e \simeq 0.97 - 0.98$ (Gillessen et al., 2013a,b; Phifer et al., 2013). In the top panel of Fig. 5.1, we plot a comparison of the total orbital velocity for the observed and simulated orbits, showing that the two curves depart from each other just near apocenter, at distances larger than $\approx 1'' \approx 1.25 \times 10^{17}$ cm from the SMBH (the source in the simulated orbit starts at rest), where the ram pressure contribution is anyway insignificant. However, the observed and simulated orbits look very different (see Figure 5.1) when projected on the plane of the sky. The orbital time of the simulated orbit is roughly shifted by 1 yr compared with that of the observed orbit. For this reason, a strict comparison of times and projected quantities can be misleading. Therefore, we will often refer to distances to the SMBH rather than times, which are only roughly comparable to the observed times.

As also discussed in Sec. 4.1, the injection of the outflow was modeled following a "mechanical approach". This means that we fixed density and velocity in a small half-circular inner boundary, with origin on the cylindrical axis of symmetry and radius r_{inb}, so to satisfy Eq. 4.2.

Eq. 4.2, however, strictly holds as long as the sound speed of the injected material is negligible with respect to the wind velocity, which constrains the value of the temperature we can set in the input region. In all our models, we set the temperature to a constant value T_{inp} and an adiabatic index $\Gamma = 1$ is assumed. This choice is based on the assumption that the temperature of the wind material is given by photoionization equilibrium due to the surrounding young stars ($T_{inp} = 10^4$ K; e.g., Gillessen et al., 2012; Murray-Clay & Loeb, 2012; Schartmann et al., 2012) and by the fact that the shocked wind material is so dense and cools so fast that it can be treated as being isothermal (see Sec. 2.2 and, e.g., Burkert et al., 2012; Scoville & Burkert, 2013). So, we set $T_{inp} = 10^4$ K in all our simulations except for the lowest velocity (LV) model described in Subsection 5.2.2 (for which such a temperature would give a sound speed comparable to the wind velocity; however, see Sec. 5.3.1 for a discussion about this choice).

Simulations of the interaction of stellar winds with the surrounding medium are usually based on the "wind tunnel" approach, where the frame of reference is fixed on the outflow and the motion through the ambient medium is simulated by injecting inflow boundary conditions in the ghost cells on one side of the domain (see, e.g., Brighenti & D'Ercole, 1995; Meyer et al., 2014). However, in our case, G2 encounters extremely varying conditions along its orbit. Injecting inflow BCs that vary with time - particularly when the motion has a transition from subsonic to supersonic - is not possible, since this would lead to propagation of artificial (shock or sound) waves in the external medium. Hence, we fixed

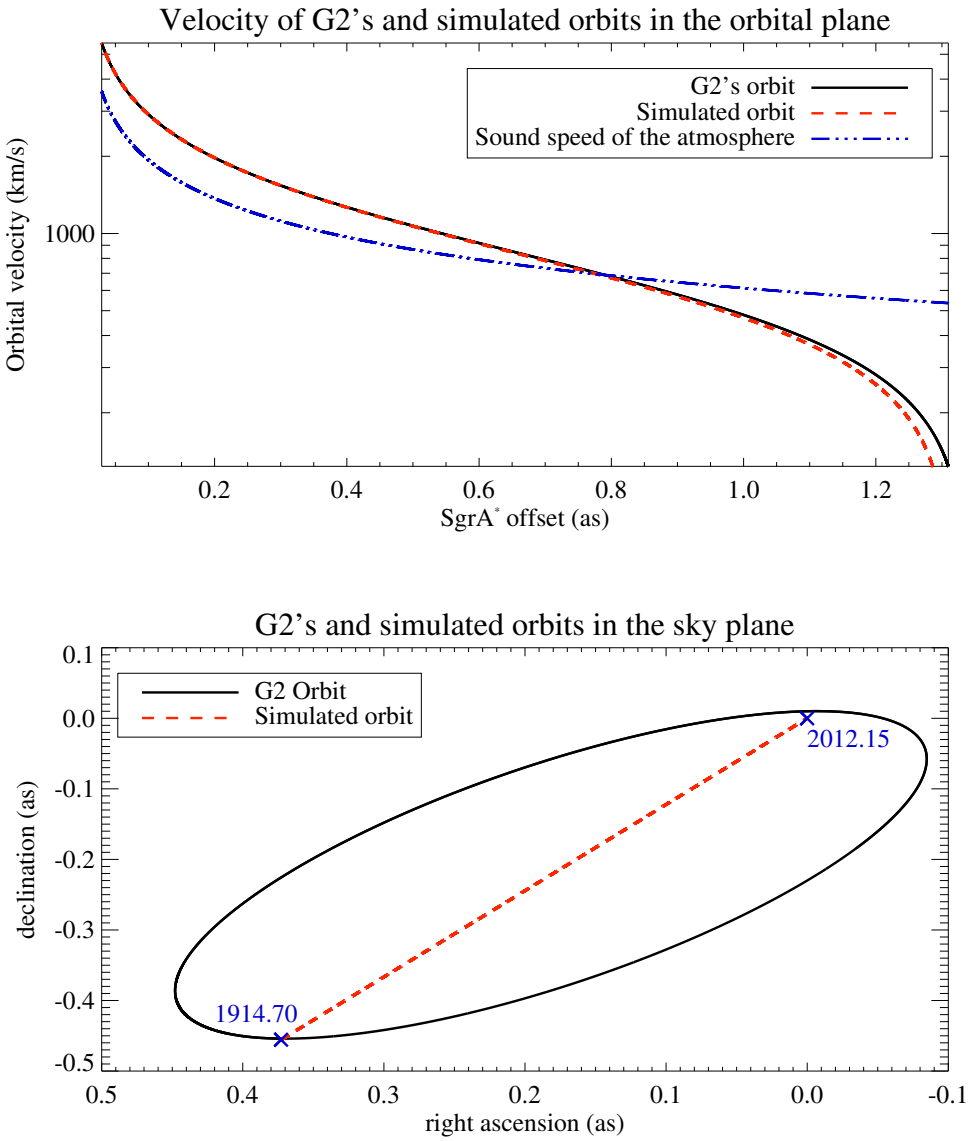

Figure 5.1: Comparison of G2's best-fit orbit (black solid line) and the simulated $e = 1$ orbit (red dashed line). The upper panel shows the evolution of the total velocity along the orbits. The blue dash-dotted line shows the sound speed of the atmosphere along the orbit. The lower panel shows the two orbits when projected on the sky plane. The blue crosses show the simulated orbit's apocenter and pericenter, with their relative orbital time.

the frame of reference on SgrA* and made the input region move along the axis of symmetry, calculating the location of the source at every timestep with a simple Runge-Kutta fourth order method. The outflow is started at G2's apocenter. The work presented in this chapter was carried out before the publication of the currently up-to-date orbital derivation (Gillessen et al., 2013b), hence we placed G2's apocenter at $(R, z) = (0, -1.64 \times 10^{17}$ cm). Assuming that the source starts blowing its wind at apocenter is somewhat arbitrary. However, following the original idea of Murray-Clay & Loeb (2012), if the object has been scattered on the observed orbit by one or more close encounters with stars in the clockwise disk (see Sec. 1.2.1 and 2.2.2), we can expect any pre-formed outflow to be disrupted and mostly stripped in these events.

The hot atmosphere is modeled following the density and temperature distribution in Eq. 2.7 and 2.8, also used by Burkert et al. (2012), Schartmann et al. (2012), Anninos et al. (2012) and De Colle et al. (2014). As discussed by Schartmann et al. (2012), this atmosphere is convectively unstable, so we followed the same numerical recipe to artificially stabilize it, with the help of a passive tracer tr advected with the wind material. A tracer allows to "paint" the gas in certain cells, so to further follow its specific dynamics and evolution. This is done through the addition of a variable tr to the array $\mathbf{U}$ (see Sec. 3.1) and to the solution of a further continuity equation, equivalent to the one for the density. Hence, the tracer is simply "advected" with the flow. In these simulations, we "painted" our injected outflow material, so to be able to distinguish it from the surrounding ambient medium. Every cell, where less than 0.01 % of the gas is made out of original cloud material, is reset to the initial condition of the atmosphere. As a result of this resetting, the formation of a bow-shock in the outer atmosphere is suppressed. However, any effect of this suppression on the wind material would not be severe. This bow shock in the atmosphere would be adiabatic and weak, with a Mach number of roughly $M \simeq 1.5$ (see Figure 5.1). The Rankine-Hugoniot conditions give an increase in density of a factor ≈ 1.7 and a same decrease in the velocity. Thus, the ram pressure in the shocked ambient medium would be just a factor ≈ 1.7 lower than the simulated one. The stagnation radius would instead not change, since the total pressure is conserved across the shock. For a further and more detailed discussion on the chosen atmosphere, we refer the reader to Burkert et al. (2012) and Schartmann et al. (2012).

Finally, we included the SMBH's gravitational field, through a $\nabla\phi$ source term, where ϕ is the simple gravitational potential generated by a Newtonian point source with mass $M_{\rm BH} = 4.31 \times 10^6$ M$_\odot$ (Gillessen et al., 2009a) at $Z, R = 0$. The gravity of the central object is not considered, since the Roche radius for a 1 $M_\odot$ star on G2's orbit is always at least a factor of three smaller than the stagnation radius given in Eq. 4.3 (see also Sec. 2.2), hence we do not expect any significant change of the structure of the wind shell due to the stellar gravity.

The hydrodynamical equations are solved using a piecewise parabolic method in space and a Runge-Kutta third order method in time. Fluxes are computed with the two-shock Riemann solver (Mignone et al., 2007).

Table 5.1 lists the different adopted parameters for all the models presented in this chapter.

	$\dot{M}_{\rm w}(M_\odot\ {\rm yr}^{-1})$	$v_{\rm w}$(km/s)	resolution	domain size (Z × R) (10^{16} cm)	n. of grid cells
standard model	8.8×10^{-8}	50	7.5×10^{12} cm 0.5 AU	$[-17.10:-0.30]\times[0:0.45]$	1.344×10^{7}
LV	8.8×10^{-8}	10	7.5×10^{12} cm 0.5 AU	$[-17.10:-0.30]\times[0:0.45]$	1.344×10^{7}
HV	8.8×10^{-8}	250	2×10^{13} cm 1.3 AU	$[-18.00:-0.15]\times[0:3.00]$	1.33875×10^{7}
LMDOT	1.76×10^{-8}	50	7.5×10^{12} cm 0.5 AU	$[-17.10:-0.30]\times[0:0.45]$	1.344×10^{7}
HMDOT	4.4×10^{-7}	50	10^{13} cm 0.7 AU	$[-18.00:-0.15]\times[0:1.00]$	1.785×10^{7}
LOWRES	8.8×10^{-8}	50	1.5×10^{13} cm 1.0 AU	$[-17.10:-0.30]\times[0:0.45]$	3.36×10^{6}

Table 5.1: Parameters of the two-dimensional simulated models.

5.2 Results

5.2.1 Standard model

Evolution of the wind

Our standard 2D model has $\dot{M}_{\rm w}=8.8\times10^{-8}M_\odot\ {\rm yr}^{-1}$ and $v_{\rm w}=50\ {\rm km\,s}^{-1}$. This value for the mass loss rate is intended to reproduce the cloud mass estimated by Gillessen et al. (2012). However, as we will show in the following, most of the luminosity of our winds comes from dense and filamentary material (see subsection 5.2.1). So, in this case, the mass estimate of these authors, based on a constant density over an ellipsoidal volume, does not hold anymore. In other words, given the complex gas distribution, properties and emissivities, in our wind models there is not a simple conversion between the total mass of the wind material and its luminosity. Anyway, the mass injected in the case of our standard model corresponds to the mass estimated by these authors.

In Fig. 5.2 we show the density distribution of the wind (in just a fraction of our total two-dimensional computational domain) for three different positions along the orbit of the source. In these images, three different regimes are clearly visible.

- In 1950 the wind is at a distance from the SMBH of ≈ 1.21 as $\approx 1.5\times10^{17}$ cm and in this part of the orbit the thermal pressure of the atmosphere is the main confinement affecting the outflow. Its structure is still almost spherical, with the *free-wind region* occupying most of the wind volume and the denser and very thin *shocked wind shell* that has already developed and turbulent Rayleigh-Taylor fingers departing from it.

- In 2003, at a distance of ≈ 0.43 as $\approx 5.4\times10^{16}$ cm, the ambient ram pressure has generated a long tail of lower density stripped material which is mixing with the atmosphere. The density of the shocked wind material is now higher due to the increase of the thermal and ram pressure of the atmosphere while approaching SgrA*. This ram pressure and the tidal force of SgrA* has also broken the spherical symmetry of the *free-wind region*: the ram pressure has compressed the front part leading to a smaller stagnation radius in the direction parallel to the motion (see Eq. 4.3).

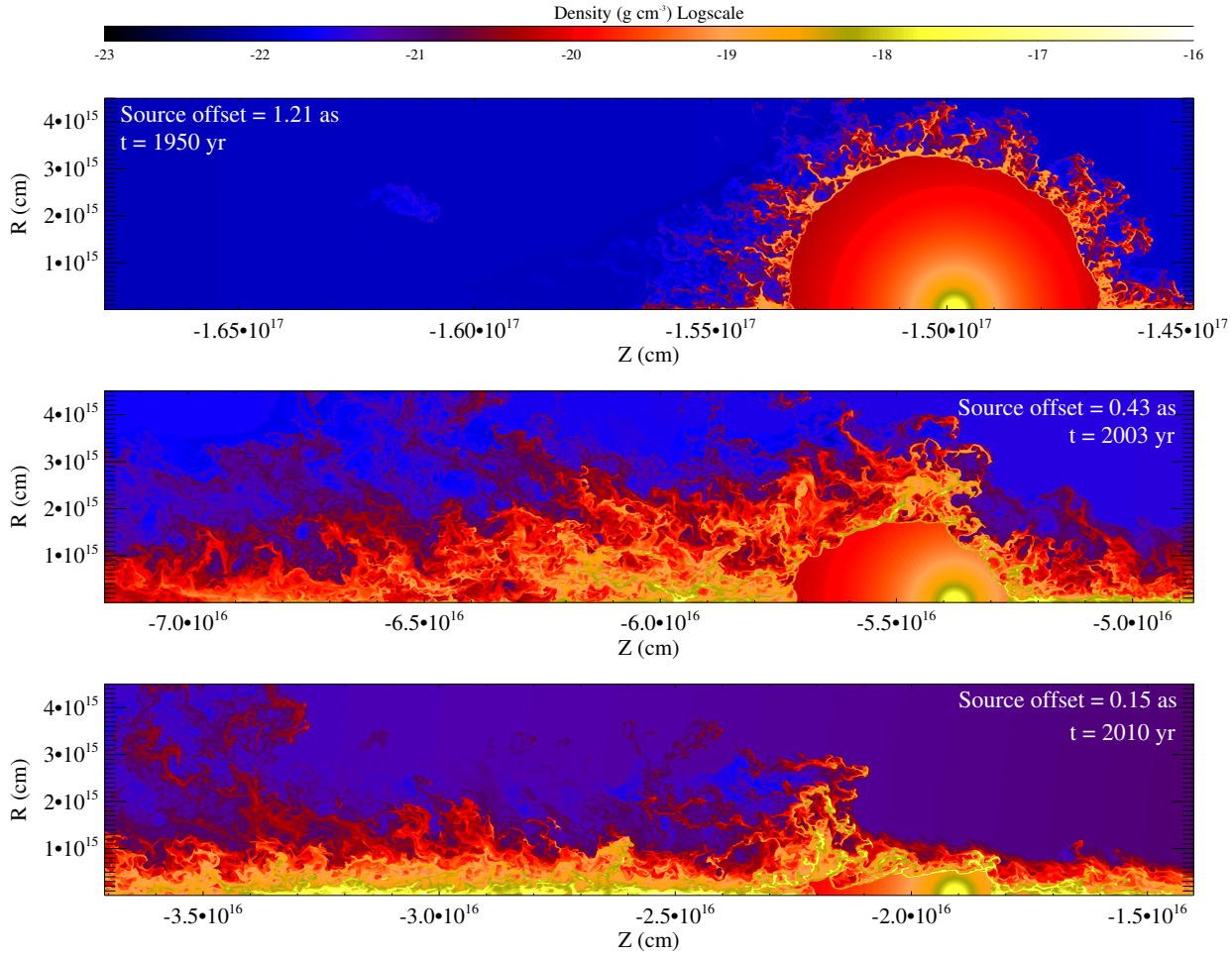

Figure 5.2: Density maps for our 2D standard model, for a distance of the source from SgrA* $= 1.21, 0.43$ and 0.15 as (from top to bottom).

- The 2010 snapshot (corresponding to a distance of ≈ 0.15 as $\approx 1.9 \times 10^{16}$ cm) shows that the *shocked wind* material has reached even higher densities and it has accumulated along the axis of symmetry due to the extremely high tidal stretching and compression in the direction perpendicular to the motion. A very tiny *free-wind region* is left at this time.

Comparison with observations

In Fig. 5.3 we plot the Brγ luminosity evolution along the orbit (upper panel, black solid line). To calculate it we used a functional form for the case B recombination Brγ emissivity

$$j_{\mathrm{Br}\gamma} = 3.44 \times 10^{-27} (T/10^4 \text{ K})^{-1.09} n_{\mathrm{p}} n_{\mathrm{e}} \text{ erg s}^{-1} \text{ cm}^{-3}, \tag{5.1}$$

(where T is the wind material temperature and n_{p} and n_{e} are the proton and electron number densities), obtained by extrapolating the values given on page 73 in Osterbrock & Ferland (2006) (see also Ferland, 1980; Hamann & Ferland, 1999, for similar functional forms). We then integrated it over all the wind material, i.e. over the grid cells with wind tracer $tr > 10^{-4}$ (the first cell in the R direction is excluded from this calculation, as explained and justified in Sec. 5.3.1). We took into account the different temperature the wind material has due to mixing with the atmosphere. When mixing with the hotter and less dense atmosphere, the wind material's emissivity significantly lowers. Assuming the former functional form is then giving much more realistic results. On the other hand, a limitation of this approach is that in our simulations the thermodynamics of the mixing is not modeled by detailed physics and it is simply given by hydrodynamical advection.

For the part of the orbit covered by the observations (indicated by the red diamonds), the luminosity ranges from a minimum value of $\simeq 2.59 \times 10^{30}$ erg/s $\simeq 0.3\ L_{\mathrm{Br}\gamma,\mathrm{G2}}$ to a maximum value of $\simeq 9.06 \times 10^{30}$ erg/s $\simeq 1.2\ L_{\mathrm{Br}\gamma,\mathrm{G2}}$. These values are comparable with the observations, even if the luminosity of our standard model increases toward pericenter, while the observed one has a constant value of $L_{\mathrm{Br}\gamma,\mathrm{G2}} \simeq 8 \times 10^{30}$ erg/s $\simeq 2 \times 10^{-3}\ L_{\odot}$ for all the period covered by the observations (Pfuhl et al., 2015).

One of the most interesting results is that - given our assumptions - most of the luminosity of the object results from *shocked wind* material (red dash-dotted line in the upper panel of Fig. 5.3), which has a very low volume filling factor (red area in the lower panel of Fig. 5.3). A significant contribution to the luminosity could actually come from the very inner part of the *free-wind* region, where the density scales with r^{-2}. In our simulations, this region corresponds to our input region, where the density is fixed to a constant value. However, given the uncertainties in the ionizing process, the amount of ionized emitting material in this region is still a matter of debate (see discussion in Sec. 4.2 and in Scoville & Burkert, 2013). In the protoplanetary disk model of Murray-Clay & Loeb (2012), these authors assume a different density distribution for the ionized material in the disk, leading to a peak of emission at the disk edge, between roughly 10 and 50 AU. That peak would be just a local and minor peak if the *shocked wind* material were taken into account. For a general wind solution, Scoville & Burkert (2013) also estimate that the cross section of the

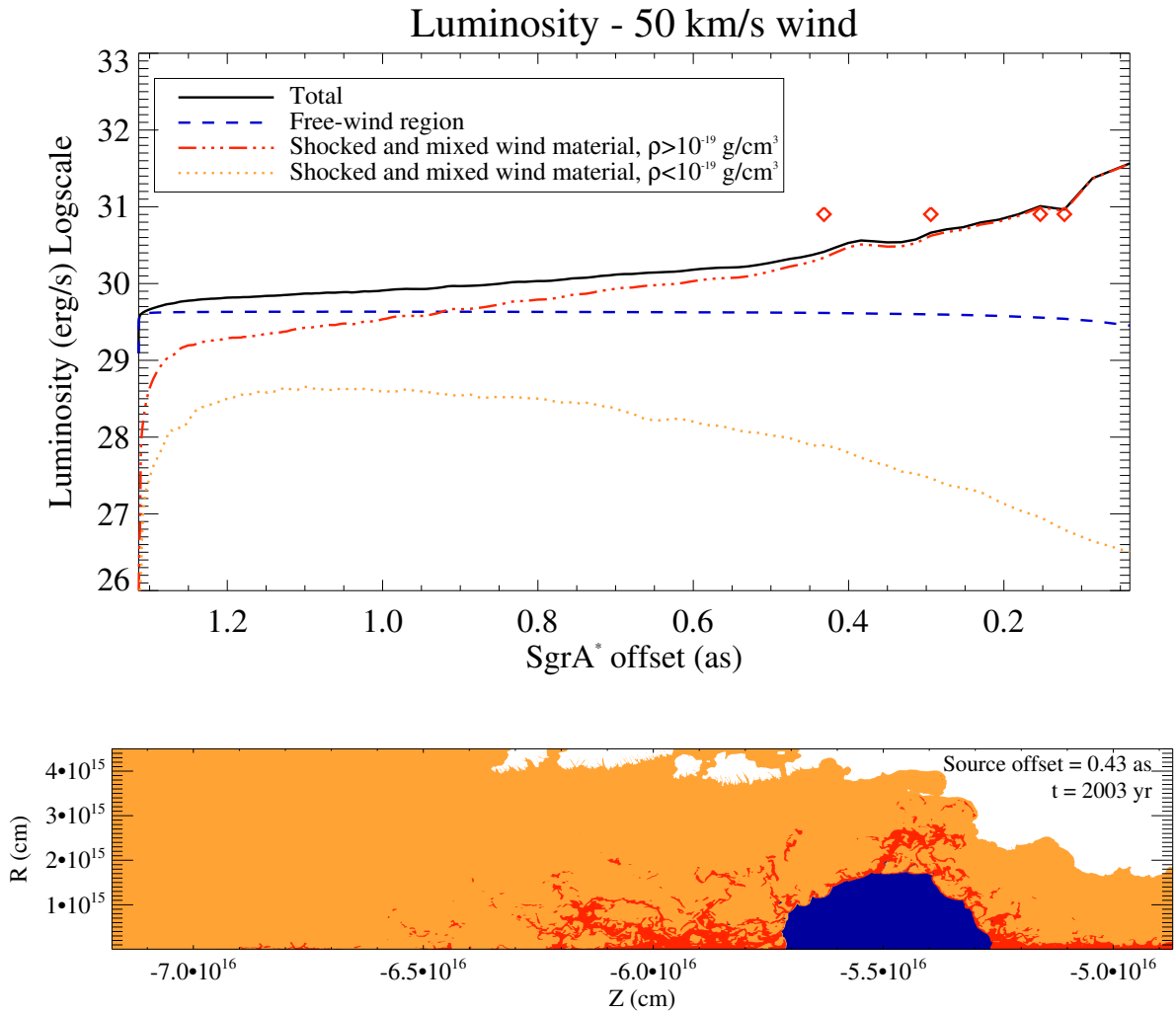

Figure 5.3: Upper panel: Brγ luminosity evolution for our 2D standard model with wind parameters $\dot{M}_{\rm w} = 8.8 \times 10^{-8}$ M$_\odot$ yr^{-1} and $v_{\rm w} = 50$ km/s. The black solid line shows the total luminosity, the blue dashed line shows the luminosity of the *free-wind region*, the red dash-dotted line shows the luminosity of the *shocked wind material* with densities higher than 10^{-19} g cm^{-3}, the orange dotted line shows the luminosity of the *shocked wind material* with densities lower than 10^{-19} g cm^{-3}. The red diamonds represent the observations. Lower panel: Wind material distribution for a distance of the source from SgrA* = 0.43 as. The colors are the same as in the upper panel.

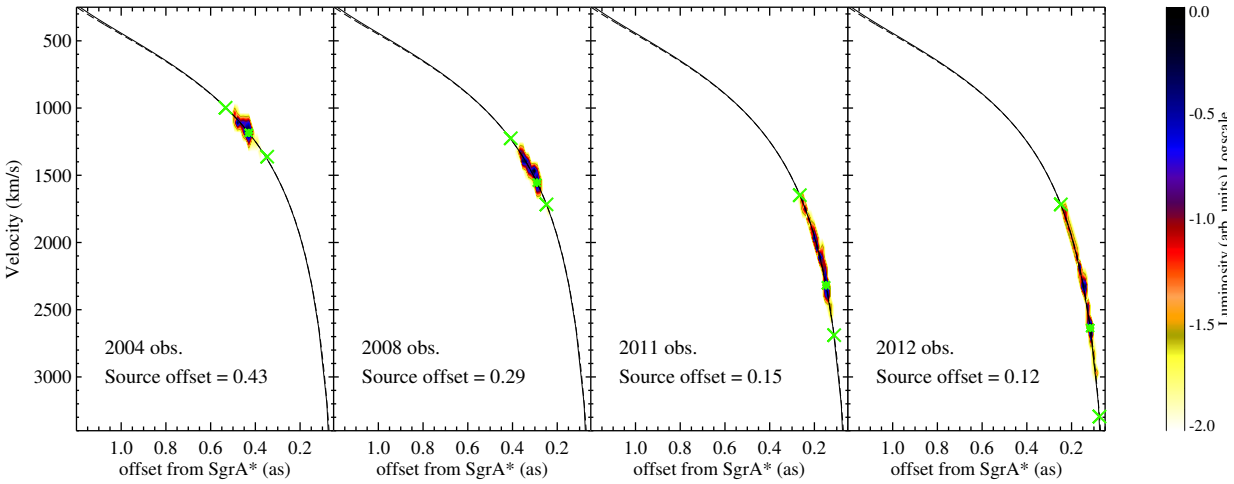

Figure 5.4: Position-velocity diagrams for our 2D standard model, for a distance of the source from SgrA* $= 0.43, 0.29, 0.15$ and 0.12 as. The green crosses show the G2 observed extremes, the green asterisk shows the position of the source in the diagram.

base of the wind (e.g., our wind input region) is too small to be ionized by the estimated flux of Lyman-α photons from the surrounding stars. On the other hand, our detailed simulations allowing for hydrodynamical instabilities and tidal stretching result in *shocked wind* material with a significantly larger cross section compared to the analytical estimates of Scoville & Burkert (2013).

Position-velocity diagrams for our standard model are shown in Fig. 5.4. As already discussed in Sec. 5.1, the observed and the simulated orbits are very different when projected on the sky plane. For this reason, we plot distance to the SMBH versus velocity along the direction of the motion, instead of position and velocity projected on the sky. In order to compare them to observations, we deproject the G2 observed extremes along the orbit at different times and put them on these plots (green crosses)[1]. As can be seen in Fig. 5.4, our standard model reproduces quite nicely the observed dynamical evolution of G2. Even if the match is not perfect, we will see in the next subsections that a slight variation of the parameters leads to significantly different sizes.

Finally, as visible in both Fig. 5.2 and Fig. 5.4, the source is never in the middle of the distribution, which shows that in the case of a compact source scenario, the stripping of the wind material and the tidal stretching of it can lead to a "dynamical decoupling" between the source and the extended emitting material, with the source being at late times much nearer the leading edge of the object. Hence, the orbit of the source itself can be slightly offset from the observed orbit, determined from the gas and dust emission (see also Chapter 6).

[1]More realistic PV diagrams will, however, be presented in chapters 6 and 7 for our 3D simulations

5.2.2 An outflow velocity study

We studied the effect of a variation of the wind velocity on the structure and observed properties of the wind. Keeping the mass loss rate fixed to the value of our standard model, we reduced and increased the wind velocity by a factor of 5, getting respectively the LV and the HV model (see Tab. 5.1).

In Fig. 5.5 and 5.6 we plot respectively the density maps and the position-velocity diagrams for a distance from SgrA* ≈ 0.15 as. The density of the *free-wind* region and, hence, of the *shocked wind* material is extremely different when changing the expansion velocity of the wind (see Eq. 4.1 and the discussion in subsection 5.2.3). As a consequence, the amount of stripped and mixed material is much larger when the wind velocity increases. Both of these phenomena lead to a change in the Brγ luminosity, as shown in Fig. 5.7. The slower 10 km/s LV model (dashed line) produces luminosities that are roughly one order of magnitude higher than those of our standard model (solid line). The faster 250 km/s HV model (dash-dotted line) has instead roughly two orders of magnitude lower luminosities. Significant differences are also visible in the position-velocity diagrams: the LV model is ≈ 0.05 as smaller than G2 (whose size is 0.15 as, at the considered position along the orbit) while the HV model has a much larger extension of ≈ 0.45 as, clearly exceeding G2's size. In terms of velocity dispersion, the HV model also shows a larger spread in velocity at given position, resulting from the higher wind velocity and from the higher turbulence of the stripped *shocked wind* material.

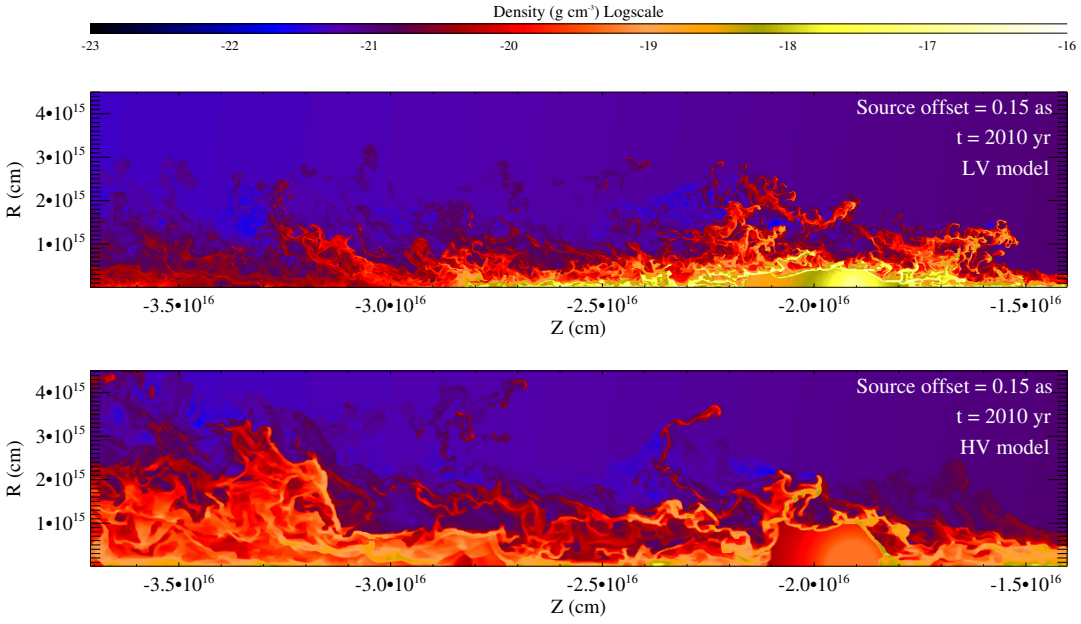

Figure 5.5: Density maps for the $v_w = 10$ km/s LV model (upper) and $v_w = 250$ km/s HV model (lower), for a distance of the source from SgrA* = 0.15 as.

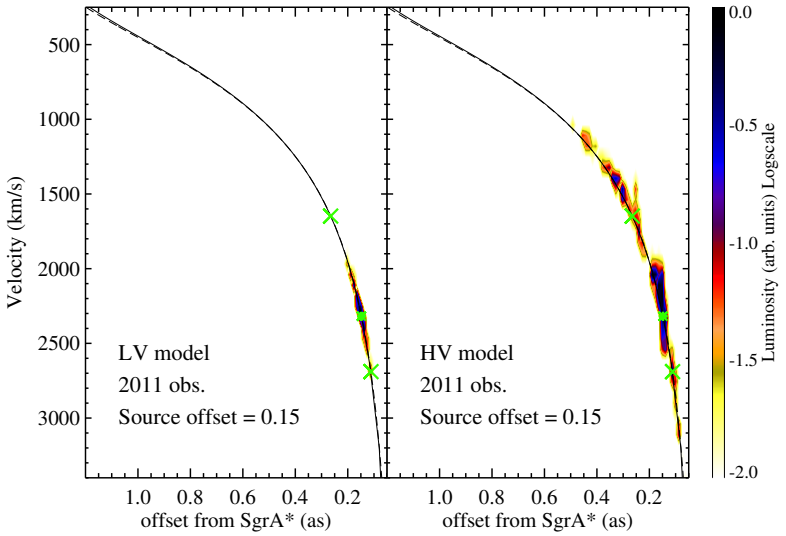

Figure 5.6: Position-velocity diagrams for the $v_{\rm w} = 10$ km/s LV model (left) and $v_{\rm w} = 250$ km/s HV model (right), for a distance of the source from SgrA* = 0.15 as. The green crosses show the G2 observed extremes, the green asterisk shows the position of the source in the diagram.

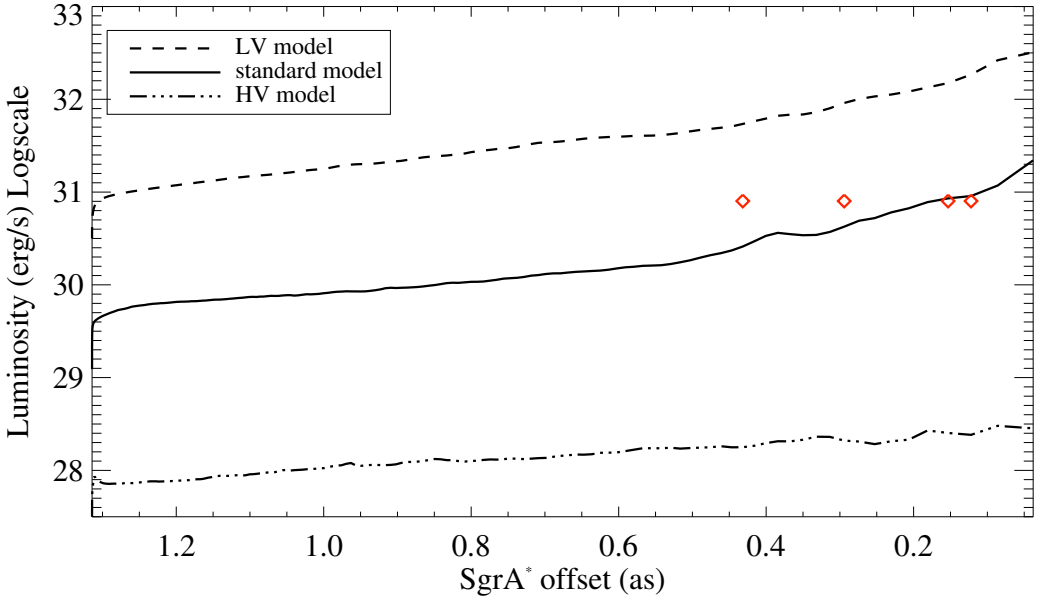

Figure 5.7: Brγ luminosity evolution for our wind velocity 2D study. The standard model luminosity evolution is also included for a comparison.

5.2.3 An outflow mass loss rate study

We have also studied the effect of a variation of the wind mass loss rate. In this case, we fixed the velocity to that of the standard model and reduced and increased the wind mass loss rate by a factor of 5, getting respectively the LMDOT model and the HMDOT model (see Tab. 5.1).

The density maps and the position-velocity diagrams for the two different $\dot{M}_{\rm w}$ models, at a distance from SgrA* ≈ 0.15 as, are shown respectively in Fig. 5.8 and Fig. 5.9. A first inspection of the density and luminosity distribution forces us to discuss the structure of the winds at late times. In fact, given Eq. 4.3, we expect the size of the *free-wind region* to be equal in the case of LV and LMDOT and similarly in the case of HV and HMDOT, given the same $\dot{M}_{\rm w} v_{\rm w}$. Fig. 5.10 shows that this is indeed true for earlier times and it provides a first qualitative explanation for the different sizes visible in Fig. 5.9, but the *stagnation radius* equation (Eq. 4.3) does not strictly apply at late times. The explanation for this behaviour is mainly given by considering the different impact of the ram pressure of the atmosphere, which depends on the densities of the different models. For different models, an equal $\dot{M}_{\rm w} v_{\rm w}$ means an equal wind ram pressure $\rho_{\rm w}(r) {v_{\rm w}}^2$. So, a factor of 5 lower velocity at constant $\dot{M}_{\rm w}$ implicitly implies a factor of 5 higher $\rho_{\rm w}(r)$ and vice versa. On the other hand, at constant $v_{\rm w}$, a factor 5 lower $\dot{M}_{\rm w}$ implies a factor 5 lower $\rho_{\rm w}(r)$ (and vice versa). The difference in density between LV and LMDOT (and HV and HMDOT) is then a factor 25. Obviously, this difference also affects the density

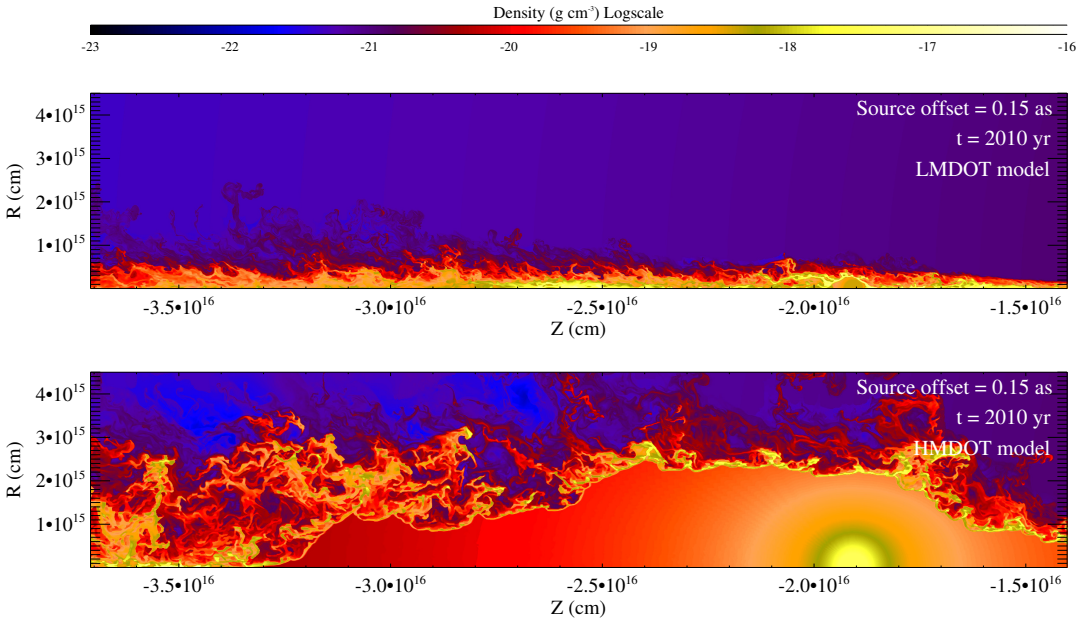

Figure 5.8: Density maps for the $\dot{M}_{\rm w} = 1.76 \times 10^{-8}$ M$_\odot$ yr^{-1} LMDOT model (upper) and the $\dot{M}_{\rm w} = 4.4 \times 10^{-7}$ M$_\odot$ yr^{-1} HMDOT model (lower), for a distance of the source from SgrA* = 0.15 as.

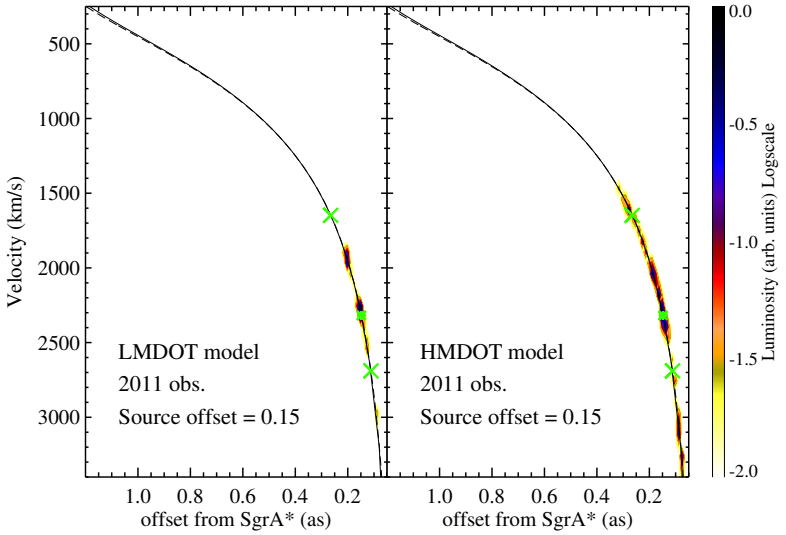

Figure 5.9: Position-velocity diagrams for the $\dot{M}_{\rm w} = 1.76 \times 10^{-8} {\rm M}_{\odot}$ yr^{-1} LMDOT model (left) and $\dot{M}_{\rm w} = 4.4 \times 10^{-7} {\rm M}_{\odot}$ yr^{-1} HMDOT model (right), for a distance of the source from SgrA* = 0.15 as. The green crosses show the G2 observed extremes, the green asterisk shows the position of the source in the diagram.

of *shocked wind* material. We can therefore distinguish two regimes and see that in the case of LMDOT and HV, given the global lower densities, the ram pressure stripping of the atmosphere acts much more efficiently, reducing the size of the free wind region at late times and accumulating backflowing stripped material behind the source. For LV and HMDOT, instead, the stripping is less efficient and the size of the *free-wind region* at late times is mainly given by the tidal stretching. In addition, Fig. 5.10 also shows that, for the same $\dot{M}_{\rm w} v_{\rm w}$, the higher velocity models (namely LMDOT and HV) have more elongated and turbulent RTI fingers, increasing the wind cross section. This phenomenon occurs because, at fixed wind ram pressure, faster winds have lower momentum, so they experience higher deceleration due to the external pressure, i.e. the higher the velocity of the wind, the more quickly is the *stagnation radius* reached. The typical timescale for the growth of RTI is inversely proportional to the square-root of the acceleration: this means that winds with higher velocities have more unstable shells.

The tidal stretching plays also a role in explaining the evolution of the luminosity. As visible in Fig. 5.11, the evolution depends on $\dot{M}_{\rm w}$, with the slope of $L_{\rm Br\gamma}$(t) increasing with decreasing mass loss rate: for the part of the orbit corresponding to the observations the luminosity increases by roughly a factor 2.6, 3.5 and 8.2 respectively in the case of the HMDOT, the standard and the LMDOT models. In the late phases, in fact, the tidal forces always compress and squeeze the wind towards the axis of the motion (that corresponds to the axis of symmetry of our cylindrical coordinates). In other words, in the proximity of the SMBH, the *stagnation radius* in the direction perpendicular to the orbital motion is

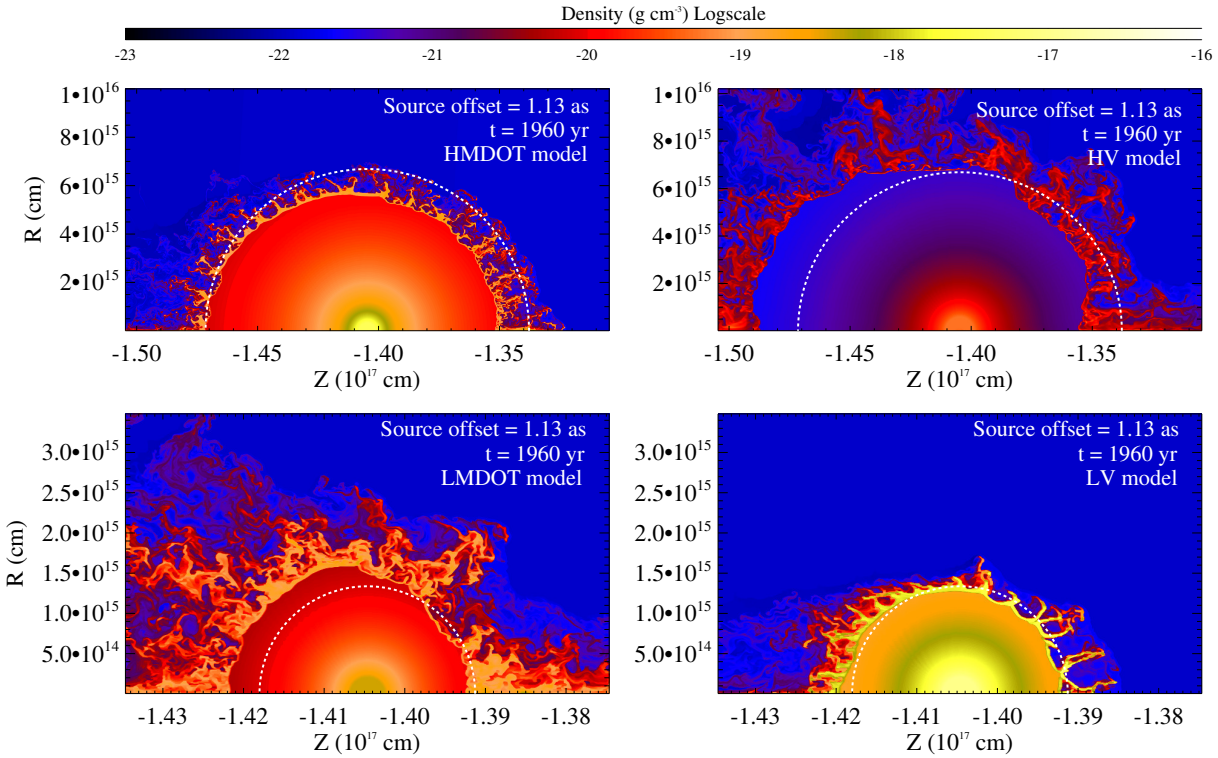

Figure 5.10: Density maps for the HMDOT and HV models (upper panels) and for the LMDOT and LV models (lower panels) , for a distance of the source from SgrA* = 1.13 as. The white dotted line denotes the expected theoretical size of the *stagnation radius* when taking into account only the thermal pressure of the atmosphere at that distance from SgrA*.

defined by the balance between the wind ram pressure and the pressure of the tidal forces. The decrease of the *stagnation radius* in this direction due to tidal compression will be evidently lower in the case of higher wind ram pressures. As a consequence, the increase of the density and luminosity of the *shocked wind* shell will also be different. This effect can be as well partially recovered in Fig. 5.7 for our velocity study.

5.3 Discussion

5.3.1 Numerical issues

It is well known that cylindrical coordinates lead to numerical artefacts near the axis of symmetry (see e.g. Vieser & Hensler, 2007; Kwak et al., 2011). In particular, in our case, all our models suffer from the formation of too elongated Rayleigh-Taylor fingers (emanating from the *shocked wind* shell) along this numerically critical part of the computational

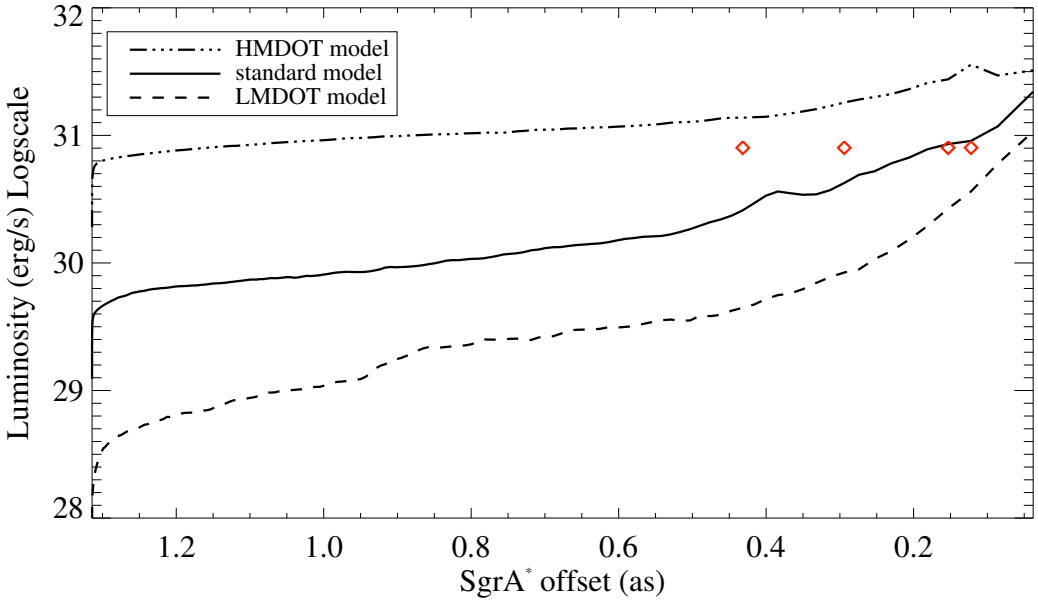

Figure 5.11: Brγ luminosity evolution for the $\dot{M}_{\rm w} = 1.76 \times 10^{-8}$ M$_\odot$ yr^{-1} LMDOT model and for the $\dot{M}_{\rm w} = 4.4 \times 10^{-7}$ M$_\odot$ yr^{-1} HMDOT model. The standard model luminosity evolution is also included for a comparison.

domain (for a similar behaviour, see, for example, the hydrodynamical simulations in Cox et al., 2012). This problem could affect our results mainly in the direction of the leading part of the wind, where the ram pressure of these fingers seems to be artificially too high, thus reducing effective compression and stripping there. Quantifying the exact impact of these artificial features on the global evolution is rather difficult, but we believe that, given their narrowness, they should not have a strong effect on the stripping of the wind at larger R positions. At the same time, considering their relatively small volume and mass (always less than 5% of the total volume and mass), these numerical features do not have a strong weight in the total luminosity. Only a very dim artificial component, corresponding to the leading part of the object, appears in the PV diagrams, e.g., in the PV diagram of the HV and LMDOT models (see Fig. 5.6 and 5.9). The cylindrical coordinates in combination with the reflective boundary at the axis of symmetry can lead to an artificial overcompression of the material in the first very few (1 or 2) cells at low R values. For this reason, we excluded the first cell in our calculation of the luminosity. This choice does not change significantly our results, but allows us to remove some artificial and transient peaks in the luminosity evolution.

The next two problems are related to the shell of *shocked wind* material. First of all, a too large size of the computational cells is expected to lead to a bad resolution of the very thin *shocked wind* material shell, particularly for the later phases, when the external

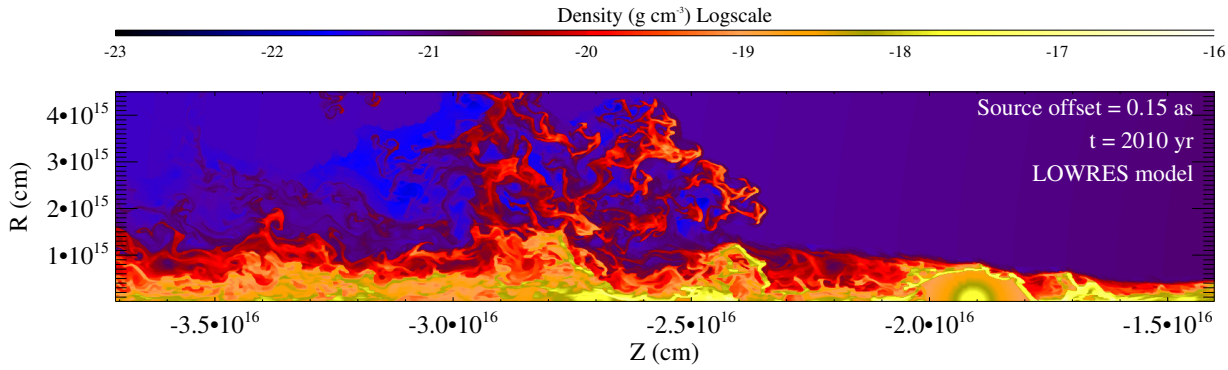

Figure 5.12: Density map for our 2D low resolution standard model, for a distance of the source from SgrA* = 0.15 as.

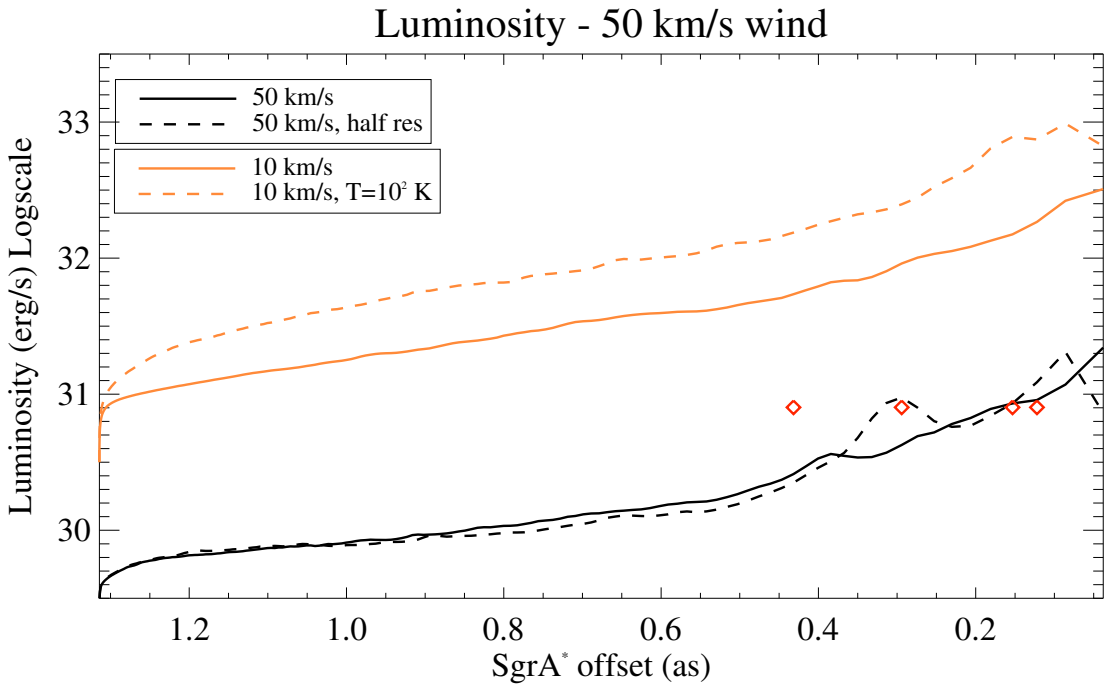

Figure 5.13: Brγ luminosity evolution for the tests discussed in Sec. 5.3.1. The solid black line shows our standard model, while the dashed black line shows its lower resolution counterpart. The solid orange line shows our LV model and the dashed orange line shows the same model with a temperature $T_{\rm in} = 10^2$ K. The red diamonds represent the observations.

ambient thermal and ram pressure increase. For this reason, we used a very high resolution

for our simulations (see Tab. 5.1). A further increase of it would have led to an extremely high computational cost for any model, but we anyway checked how the resolution can effect the results. We thus doubled the grid cell size in all directions and ran again our standard model at this lower resolution (LOWRES model, see Tab. 5.1). To first order, the matter distribution is very similar to that of the standard model, as can be seen in Fig. 5.12. Also the luminosity evolution is comparable (see Fig. 5.13, black dashed line).

The second problem is related to the temperature of the *shocked wind* shell. In the LV model the temperature of the wind is not set to 10^4 K (as in all the other models), but to 10^3 K. The reason for this choice is related to our mechanical modeling of the winds. In the case of the LV model, the velocity we set in the input region roughly corresponds to the sound speed of a 10^4 K gas. Setting such a temperature in the input region would mean that the injected thermal and ram pressure becomes comparable, which would lead to an over-injection of mass and velocity (see Sec. 5.1). However, a lower temperature in the wind material also leads to a lower thermal pressure in the shell of *shocked wind* material. This is a problem, because a lack of pressure support also produces slightly higher densities in this region and thus leads to higher luminosities (see Eq. 5.1). To get an idea of how this phenomenon can affect the resulting luminosities, we ran the LV model setting an even lower temperature of 10^2 K. The luminosity evolution is shown in Fig. 5.13: in this case, the luminosity is roughly a factor of 3 higher along most of the orbit. We therefore infer that the luminosity evolution of the LV model must be taken with care, since we cannot exclude systematically lower values in the case of a shell of temperature equal to 10^4 K.

5.4 Conclusions from the 2D simulations

Our simulations show that the presence of a surrounding high-temperature atmosphere (like that predicted by ADAF/RIAF solutions for the diffuse X-ray emission in the Galactic Center) could be very important when modeling any compact source scenario for G2. As already shown by Scoville & Burkert (2013), the free-streaming wind interacting with this hot atmosphere will be shocked. In the case of the so-called diffuse cloud scenario (see Sec. 2.2.1), the orbital evolution of the object before pericenter is, as a first approximation, ballistic. In the compact source scenario, instead, due to the high thermal pressure of the ambient medium confining the outflow, the size of the free streaming wind region is always small and constrained by the equilibrium between the external pressure and the wind ram pressure. Already at early stages, a very thin, dense, and Rayleigh-Taylor unstable shell of shocked wind material forms around the free-wind region. The structure of the studied winds is very different from that of typical stellar winds described by Weaver et al. (1977), where the shocked wind material forms a large shell with low density and a thinner, but dense, shell of swept and shocked ambient material propagates outwards (see also Sec. 4.1. For our parameters, a very weak bow shock is expected to form when the source of the wind reaches orbital velocities higher than the sound speed of the hot environment, i.e., in the late phases. Due to our numerical setup, this shell is not reproduced, but its contribution to the Brγ luminosity of G2 is negligible, as shown by Scoville & Burkert

(2013). Another interesting property of this scenario is that a dominant contribution to the total luminosity comes from the shocked wind material, which has a highly filamentary structure. The shocked wind shell is in fact strongly Rayleigh-Taylor unstable due to the wind expansion and it is hence forming elongated fingers. This fact is, along with the $1/r^2$ density distribution of the free-wind region, the main difference with respect to the diffuse cloud scenario, where the object has instead a more or less uniform density all over its volume. Distinct from the diffuse cloud scenario, at late phases the ram pressure of the atmosphere can have an important role in affecting the structure of the wind (via stripping of wind material), while, as in the diffuse cloud scenario, the dominant process at late phases is the squeezing and compression by the SMBH extreme tidal field of the object in the direction parallel to the motion. A simple decoupling of all these different effects is hard to perform in an analytical study.

The 2D model that best reproduces the observations has $\dot{M}_{\rm w} = 8.8 \times 10^{-8} M_{\odot}$ yr^{-1} and $v_{\rm w} = 50$ km s^{-1}. A slight variation of $\dot{M}_{\rm w}$ and $v_{\rm w}$ can quite significantly change the observed properties of the object. Roughly speaking, when fixing the mass loss rates, a higher velocity results in a lower luminosity and a larger size of the emitting material (and vice versa). At constant velocity, a higher mass loss rate instead leads to a higher luminosity and a larger size (and vice versa). Thus, a combination of observed size and luminosity can effectively constrain the wind parameters. The dependence of the luminosity and the size of the object on the wind parameters is also summarized in Figure 5.14.

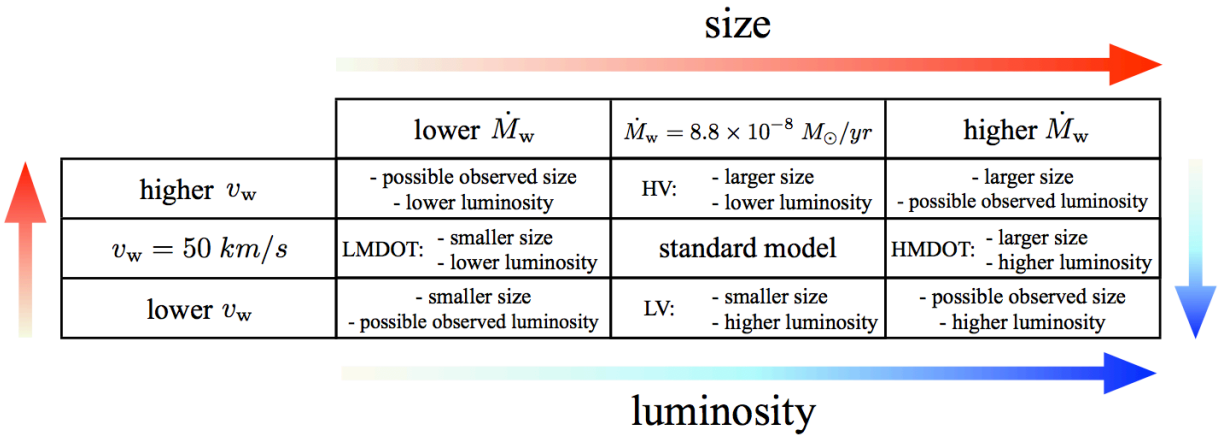

Figure 5.14: Dependence of the luminosity and the size of G2 on the wind parameters.

A possible candidate for G2's source, given our best parameters, could be a young T Tauri star, as already suggested by Scoville & Burkert (2013). These authors assumed $\dot{M}_{\rm w} = 4 \times 10^{-8} {\rm M}_{\odot}$ yr^{-1} and $v_{\rm w} = 100$ km s^{-1}. Our standard (and best) model has roughly a factor two higher mass loss rate and lower velocity. These values are a bit extreme, but still in the ranges of the observations ($\dot{M}_{\rm w} = [10^{-7}, 10^{-12}]$ M$_{\odot}$ yr^{-1} and $v_{\rm w} = [50, 300]$ km s^{-1}; White & Hillenbrand, 2004). T Tauri stars are young objects, with

ages between 10^5 and 10^7yr (see, e.g., D'Antona & Mazzitelli, 1994). This age is comparable with the age of the young stellar disk (Paumard et al., 2006; Bartko et al., 2009, see Sec. 1.2.1) where this star was born few Myr ago and subsequently scattered. A major caveat of this scenario is the geometry of the T Tauri outflows: there are several clues indicating that these outflows are bipolar winds or jets (e.g., Hartigan et al., 1995; White & Hillenbrand, 2004). We will briefly discuss this issue in chapters 6.

2D simulations with cylindrical coordinates can give a realistic evolution of the spherically expanding outflow. At the same time, they allow high resolutions, needed for the very filamentary nature of the shocked wind material. However, they suffer of some numerical artifacts (see Sec. 5.3.1), they do not allow the construction of realistic PV diagrams and the study of G2's evolution at its pericenter passage. Hence, we moved a step forward and repeated the current study in 3D cartesian coordinates, with the use of AMR (see chapter 6).

Chapter 6

3D AMR simulations of the "compact source scenario"

The purpose of this chapter is to present the 3D simulations for our outflow scenario, carried out on a Cartesian grid and making use of the AMR implementation of the code PLUTO. As already discussed, the main advantage of 3D simulations is in being able to simulate the actual Keplerian orbit of G2. This gives a more realistic evolution, it can reduce some numerical artifacts linked to 2D cylindrical coordinates and it allows the construction of mock PV diagrams for a comparison to the observed ones. However, due to the computational cost of 3D simulations, even with an adaptive refinement of the grid, lower resolutions can be reached. As a consequence, the present simulations do not allow us to strongly rely on the total Brγ luminosity as a good constrain for our models, as in the case of the 2D simulations of chapter 5. Thus, this study represents a step forward, but a correct interpretation of its output needs to be based on the results presented in chapter 5.

In Section 6.1 we will discuss few details about the setup of the 3D simulations. The results are presented in Section 6.2, where we compare them to the observations and we study the effect of the outflow parameters. Section 6.3 is dedicated to the numerical limitations, to compare our study with previous ones (including the simulations in Chapter 5) and to discuss the possible nature of the source. A quick summary can be found in Section 6.4. The present work is to be submitted to *Monthly Notices of the Royal Astronomical Society*.

6.1 Simulation setup

As anticipated, the present 3D simulations are performed by means of the AMR strategy, implemented in the code through the CHOMBO[1] library. Performing them with a uniform grid would have been computationally not feasible. For the refinement criterion, we chose the standard one in PLUTO, based on the second derivative error norm (Mignone et al.,

[1] https://seesar.lbl.gov/anag/chombo/

2012), and we applied it to the density. The criterion has been widely tested and it is able to resolve at the highest resolutions most of G2's material. The computational domain is Cartesian, with coordinates (x, y, z). This means that the input region is, this time, spherical. The outflow is again modeled in a "mechanical" way, where the velocity is set to the constant wind value $v_{\rm w}$ and the density $\rho_{\rm w}$ is set to satisfy Eq. 4.2 (this time over the whole input region and not only at its boundary). However, in order to reach a reasonable sampling of the input region, i.e. a good isotropy of the outflow, the radius of the input region is varying, in time, proportionally to the theoretical stagnation radius (see Eq. 4.3), with minimum and maximum allowed values equal to 2.10×10^{14} cm and 1.05×10^{15} cm, respectively. The temperature of the injected material is again set to $T_{\rm inp} = 10^4$ K and an adiabatic index $\Gamma = 1$ has been assumed (i.e., the equation of state is isothermal; see discussion in Sec. 5.1). Compared to the 2D simulations in chapter 5, the source's orbit is now a proper elliptical orbit and it has been updated to the one derived by Gillessen et al. (2013b) through Brγ observations. The full orbit has been previously integrated with a leapfrog method and, at every timestep, the source's positions and velocities are interpolated from the stored ones using a 1st order Newton polynomial formula. As in the previous 2D study - and differently than in De Colle et al. (2014) -, we decided to start the simulation (and the outflow) at apocenter. Again, the atmosphere has been modeled according to Eq. 2.7 and 2.8 and reset with the same strategy described in Sec. 5.1. We stress again that this is a very idealized model. Given the uncertainties in the actual distribution of the accretion flow around SgrA*, we still decided to keep it as idealized as possible, to be able to better understand 0th-order hydrodynamical effects on G2. The gravity of SgrA* is included again as a Newtonian point source with mass $M_{\rm BH} = 4.31 \times 10^6 M_\odot$ (Gillessen et al., 2009a) at $x, y, z = 0$.

A further 2D test run in cylindrical coordinates, with the same setup as in chapter 5 has also been performed for the sake of comparison. A list of the parameters of the simulations discussed in the present chapter can be found in Table 6.1.

	$\dot{M}_{\rm w}$ ($M_\odot$ yr^{-1})	$v_{\rm w}$ (km/s)	max resolution	grid type	domain size (x × y × z / R × z) (10^{16} cm)
standard model	5×10^{-7}	50	1.25×10^{14} cm 8.3 AU	3D cartesian (AMR)	$[-26.4 : 1.2] \times [-3.6 : 4.8] \times [-2.4 : 2.4]$
HV3D	5×10^{-7}	250	1.25×10^{14} cm 8.3 AU	3D cartesian (AMR)	$[-28.8 : 2.4] \times [-3.6 : 7.2] \times [-4.8 : 4.8]$
LMDOT3D	10^{-7}	50	1.25×10^{14} cm 8.3 AU	3D cartesian (AMR)	$[-26.4 : 1.2] \times [-3.6 : 4.8] \times [-2.4 : 2.4]$
HMDOT3D	2.5×10^{-6}	50	1.25×10^{14} cm 8.3 AU	3D cartesian (AMR)	$[-26.4 : 1.2] \times [-3.6 : 4.8] \times [-2.4 : 2.4]$
stLOWRES	5×10^{-7}	50	2.5×10^{14} cm 16.6 AU	3D cartesian (AMR)	$[-26.4 : 1.2] \times [-3.6 : 4.8] \times [-2.4 : 2.4]$
st2D	5×10^{-7}	50	1.25×10^{14} cm 8.8 AU	2D cylindrical (fixed grid)	$[0.0 : 1.8] \times [-28.8 : -3.0]$

Table 6.1: Parameters of the simulated 3D AMR models. A 2D test model is also included.

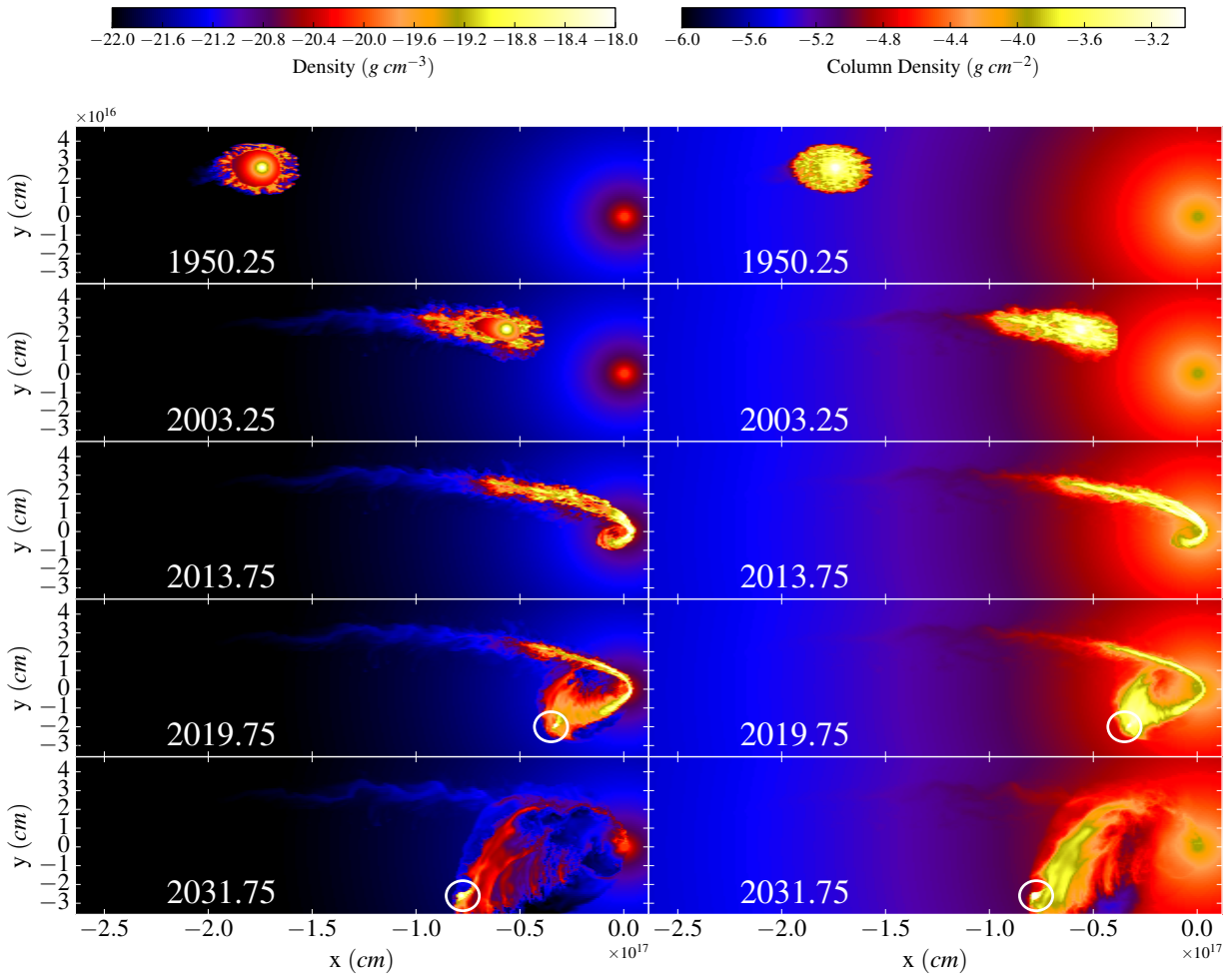

Figure 6.1: Density maps for the 3D standard model. Left panels show the density distribution in a slice at z=0. The right panels show the column density, i.e. the integral of the density along the z direction. The white circles show the outflow reforming after pericenter.

6.2 Results

6.2.1 The standard model

We adopt a mass loss rate of $\dot{M}_{\rm w} = 5 \times 10^{-7} {\rm M}_{\odot}\ {\rm yr}^{-1}$ and a wind velocity of $v_{\rm w} = 50\ {\rm km\,s}^{-1}$ for our standard model.

As shown in Fig. 6.1, the evolution of the density distribution in this 3D simulation is very similar to the one of the 2D simulations in chapter 5. The outflow is free-flowing until its ram pressure reaches the pressure of the external hot and dense atmosphere. Hence, it is composed of an inner part, whose density scales as $1/r^2$ (due to the continuity equation), that is surrounded by the part of the outflow that gets shocked by the impact with the atmosphere. This shocked material is highly Rayleigh-Taylor unstable. At the beginning, the outflowing material is still in a quasi-spherical configuration, since the isotropic thermal pressure of the atmosphere is still dominant compared to its anisotropic ram pressure. At later times, the free-wind region shrinks due to the increasing thermal pressure, the ram pressure makes it asymmetric and the stripped shocked material is forming a small tail trailing the source. Overall, though more filamentary, the distribution of the outflowing gas is on large scales very similar to the one in the "diffuse cloud" simulations of Schartmann et al. (2012), Anninos et al. (2012) and Schartmann et al. (2015), particularly right before and after pericenter, when the material is first reduced to a thin filament by the tidal force from the SMBH and then expands, strongly increasing its cross section.

Due to the asymmetry of the free-wind region and the formation of the small tail of stripped material, at the time of the observations, the central source is always in the leading part of G2. The immediate implication is that putting our input region on G2's orbit, as it is obtained from the observations, will never lead to a perfect match with the obervations. For this reason, a time shift between observations and simulations must be always applied when comparing them.

As expected, the simulation also shows that the emitting source becomes, at a certain point, distinguishable from the rest of G2. This might happen already around year 2019-2020, when the source creates a second peak in the density distribution (see circles in the lowermost panels of Fig. 6.1). This is a clear difference compared to the diffuse cloud simulations and the decoupling between the source and the previously emitted gas, after pericenter, could eventually be the smoking gun to understand the nature of G2.

6.2.2 Matching the PV diagrams

Compared to our 2D study, the 3D simulations now allow us to construct realistic PV diagrams, like the ones already presented in Schartmann et al. (2015). To do this, we first project every cell in our computational domain onto the sky plane, according to the last orbital elements derived by Gillessen et al. (2013b) for the Brγ observations. This is done through a transformation from (x, y, z, v_x, v_y, v_z) to $(ra, decl, losv)$ where ra, $decl$ and $losv$ are the right ascension, the declination and the line of sight (l.o.s.) velocity, respectively. We can, from this, create a 3D histogram of the Brγ luminosity, with bin size equal to 12.5

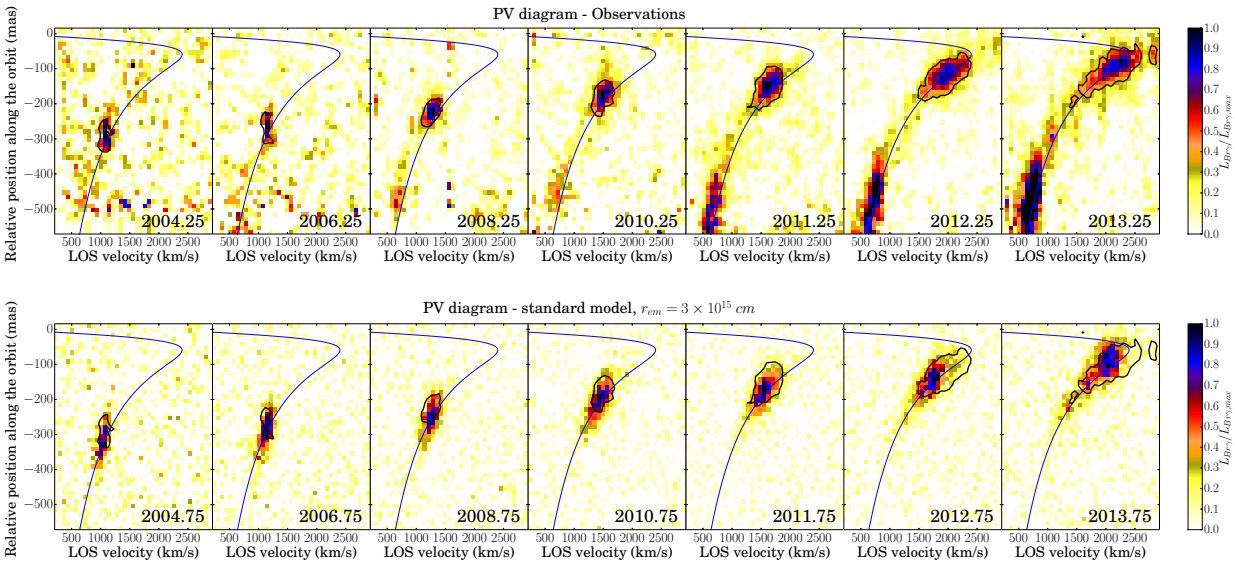

Figure 6.2: Position-Velocity diagrams for the 3D standard model. The upper panel shows the observations, while the lower one shows the case of $r_{\rm em} = 3 \times 10^{15}$ cm. The black contours show the position and extent of the observed G2.

mas for *ra* and *decl* and 69.6 km s^{-1} for *losv*. These values correspond to the size of the 3D pixels (or "voxels") of SINFONI's datacube. We then apply a smoothing in all directions with FWHM equal to 81 mas in right ascension and declination and to 120 km s^{-1} in l.o.s. velocity. These values correspond to the instrumental point spread function (PSF) and spectral resolution. At this point, every cell is spatially projected onto the derived orbit, using it as a curved slit in the $(ra, decl)$ space (a slit curved along G2's orbit has also been used for the construction of the observed PV diagrams; see Gillessen et al., 2013a). The former operation reduces the triplet $(ra, decl, losv)$ to a couple $(pos, losv)$ - where *pos* is the position on the orbit - and creates a 2D position-velocity histogram. Given the uncertainties in the luminosity discussed in Sec. 4.2 and 6.3.1, every PV diagram is then scaled to its maximum. Noise is finally extracted from the observed PV diagrams and added to the simulated ones.

Again, the luminosity is calculated using a functional form for the case B recombination Brγ emissivity, according to Eq. 5.1.

Given the big uncertainties in the amount of emission from the free flowing part of the outflow (see Sec. 4.2), we present here the effect on the Brγ luminosity of different contributions of this region. Namely, we calculate PV diagrams assuming that the free-wind region emits in Brγ up to a certain inner radius $r_{\rm em}$, where $r_{\rm em} = [3\times10^{14}, 10^{15}, 3\times10^{15}]$ cm. We also calculated PV diagrams for the shocked outflow material only (in the text we will denote this case with $r_{\rm em} = r_{\rm shock}$).

The results are shown in Fig. 6.2 and 6.3. As already mentioned in Sec. 6.2.1, a

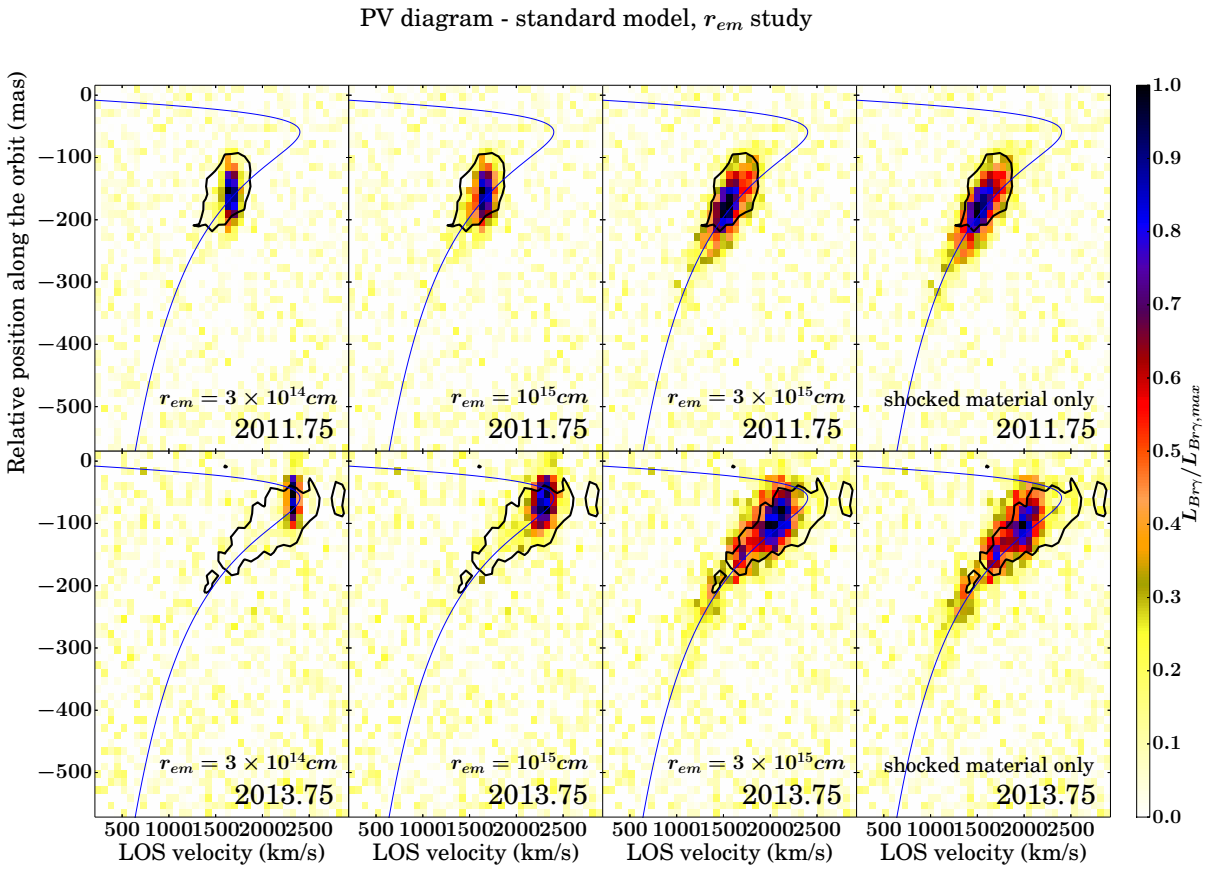

Figure 6.3: Position-Velocity diagrams for the standard model. The different panels show the simulated PV diagrams for different assumptions on the inner emitting radius $r_{\rm em}$. For every panel, the luminosity per bin is scaled to the maximum one. The upper and lower panels are obtained for a simulation year of 2011.75 and 2013.75, respectively. The black contours show the position and extent of the observed G2.

reasonable comparison needs a time-shift of roughly half a year with respect to the observations. When looking at the $r_{\rm em} = r_{\rm shock}, 3 \times 10^{15}$ cm cases, the simulated material has a qualitatively comparable extent, even though it fails to reproduce the high velocity material that seems to overshoot the orbit derived from observations, just before the pericenter passage. This is again due to the fact that, close to pericenter, the outflow material is asymmetrically distributed with respect to the source, with most of the material in a trailing tail. When going to smaller values of $r_{\rm em}$, the emitting region moves to slightly higher velocities and positions on the orbit, but it becomes smaller and smaller in the PV diagrams. This is a direct consequence of the location and of the important impact of the free-wind region on the outflow emission. In fact, given Eq. 4.2, the emission measure EM$\propto \int \rho_{\rm w} dV \propto r^{-1}$ is diverging for small distances from the source. As a result, the more

the inner part of the free-wind region is included, the more dominant the free-wind region, the smaller the emitting region visible in the PV diagrams. So, all in all, we conclude that a good match with the observations can be reached only if a tiny fraction of the free-wind region is actually emitting. This conclusion is general and can be also deduced from the parameter study in Sec. 6.2.3, where we show that G2 appears too small for every model, when $r_{\rm em} < 3 \times 10^{15}$ cm. A probably better result could also be reached with a slightly different (more eccentric) orbital solution. In fact, uncertainties in the observations seem to give enough room for this possibility. However, testing it directly with simulations is beyond the scope of the present work.

6.2.3 Parameter study

Following the same approach as for our 2D simulations, we decided to perform a parameter study, varying the mass-loss rate and the velocity of the outflow. We hence run models LMDOT3D and HMDOT3D with same velocity as the standard model's one, but with a factor of 5 smaller and larger mass-loss rate, respectively. Concerning the velocity, we chose

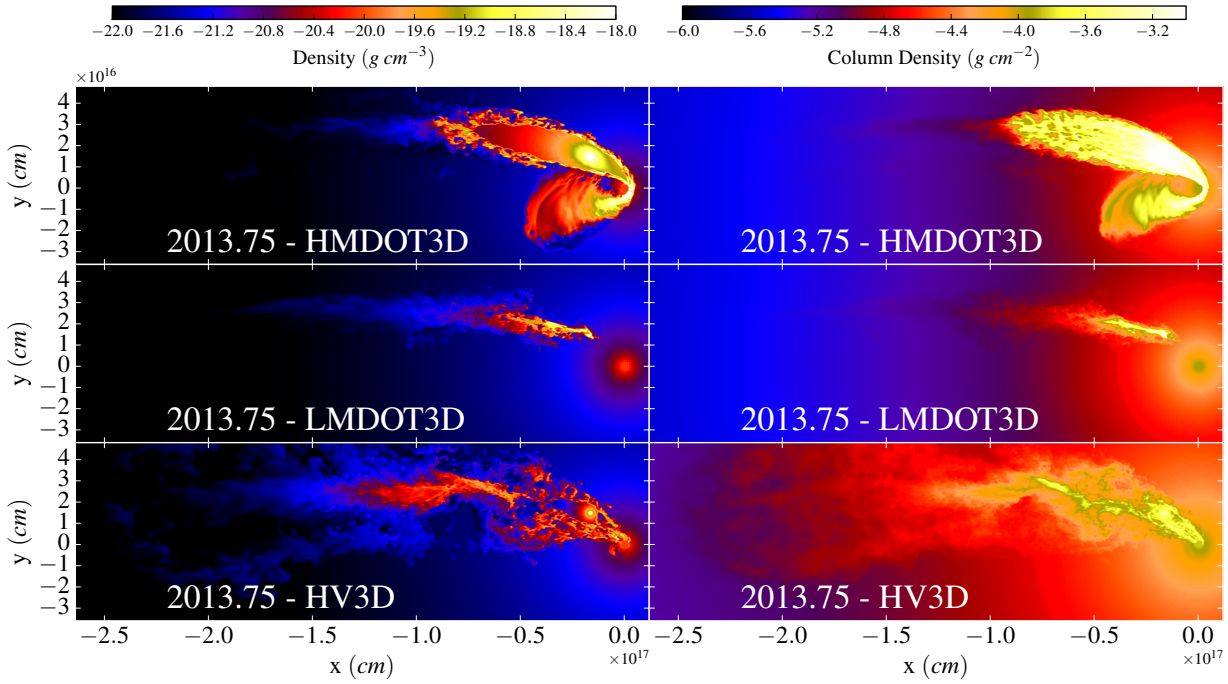

Figure 6.4: Density maps for the simulations of our 3D parameter study. Left panels show the density distribution in a slice at z=0. The right panels show the column density, i.e. the integral of the density along the z direction.

to run just the HV3D model, with wind velocity equal to $v_{\rm w} = 250$ km s^{-1} $= 5 \times v_{\rm w,standard}$. As already discussed in chapter 5, given the isothermal equation of state, a temperature of $T = 10^4$ K in the injected material brings the sound speed of the wind to $c_{\rm s,w} \approx 10$ km s^{-1}. As a consequence, for wind velocities too close to $c_{\rm s,w}$, the injected thermal and ram pressure become comparable, leading to too high mass loss rates and velocities. However, the 2D study has already shown that a lower outflow velocity has the effect of reducing G2's size (see Sec. 5.2.2 and Fig. 5.14).

Fig. 6.4 shows the density maps for the three models of the parameter study. As already described in Sec. 5.2.3, for LMDOT3D and HMDOT3D the outflow is too dense for the ram-pressure stripping to be efficient enough. Hence, the size of the outflow is mainly given by momentum equilibrium between the outflow and the external forces, namely the thermal and ram pressures of the atmosphere and the tidal force of the SMBH. This explains why LMDOT3D and HMDOT3D are respectively smaller and bigger than the standard model. In the HV3D case, the outflow is much less dense and the shocked material spreads out over a large volume. This enables the formation of a long cometary tail by efficient ram pressure stripping, as in the case of the model presented in chapter 7.

Fig. 6.5 shows the PV diagrams for our parameter study. In the case of model HMDOT3D, G2 looks too elongated when only the shocked wind material is considered, while a reasonable match to observations could eventually be reached in the case of $r_{\rm em} > 3 \times 10^{15}$ cm. Model LMDOT3D is instead producing a too compact emission for every assumption on $r_{\rm em}$. HV3D can instead result in a bimodal distribution in the PV diagrams, when looking at the emission of the shocked material only. However, for HV3D, the separation between the two simulated emission spots is not large enough to match the observed position of G2 and G2t on the orbit (see Fig. 6.2 and chapter 7).

When looking at the luminosity evolution in Fig. 6.6, while models LMDOT3D and HV3D have a too low luminosity (confirming the trends found with our 2D study), model HMDOT3D is matching the observations when the shocked-material only is considered, while it is a factor ≈ 2 too luminous when $r_{\rm em} = 3 \times 10^{15}$ cm is adopted. The first evident effect is that lower mass-loss rates or higher velocities produce globally lower luminosities. This is simply explained by Eq. 4.2 and 5.1, showing that the luminosity is proportional to the integral of $\rho_{\rm w}^2$. and that $\rho_{\rm w}$ is directly proportional to the mass-loss rate and inversely proportional to the outflow velocity. So, on a 0-th order, outflows with lower mass-loss rates and/or higher velocities are less dense and have a lower emission measure, and vice versa. For any fixed model, a varying contribution is also given by the free-wind region, depending on the choice of $r_{\rm em}$. This result, however, is in contradiction with what has been found by means of 2D simulations, where the shocked material was dominating the total luminosities close to pericenter. This is partially explained by the poor resolution of the present simulations, as discussed in Sec. 6.3.1. As a consequence, we conclude that the absolute values of the calculated luminosities must be taken as lower limits, while the PV diagrams are more solid and stable diagnostic tools.

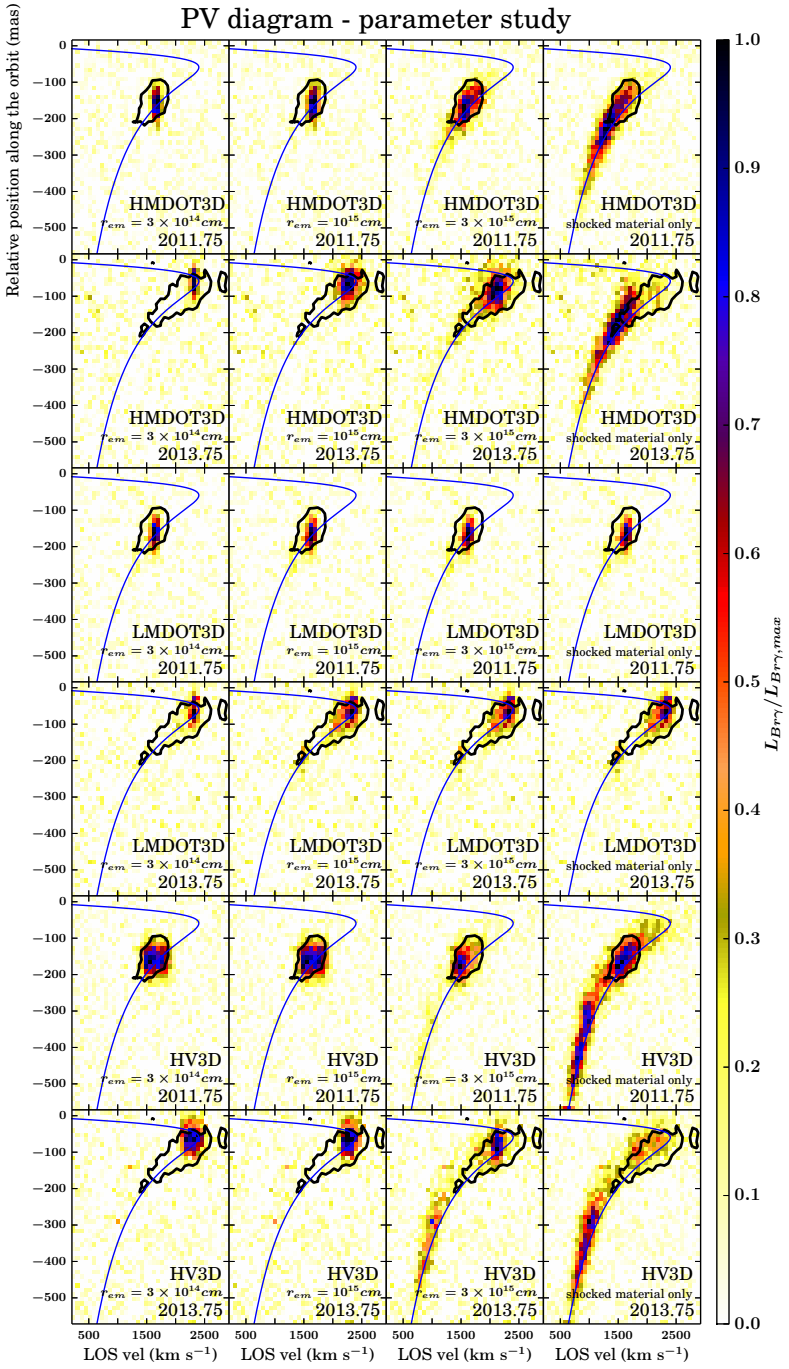

Figure 6.5: Position-Velocity diagrams for our 3D parameter study. The different panels show the simulated PV diagrams for different assumptions on the inner emitting radius $r_{\rm em}$. For every panel, the luminosity per bin is scaled to the maximum one. The black contours show the position and extent of the observed G2.

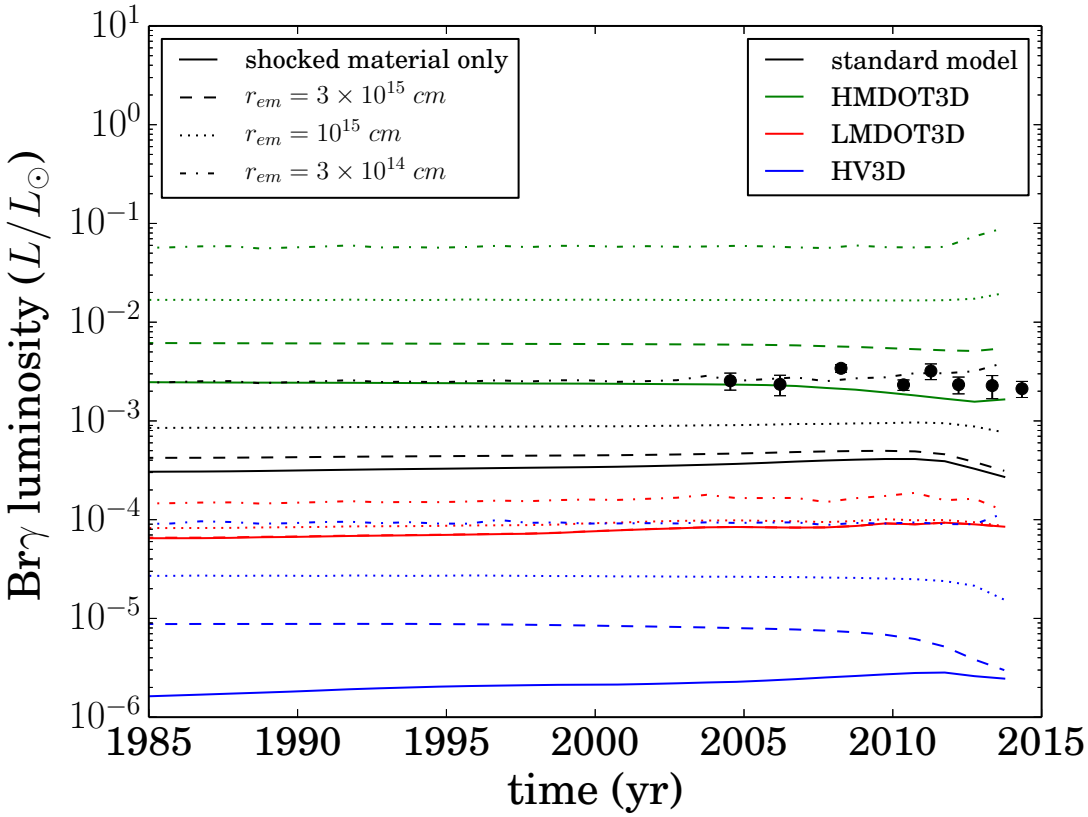

Figure 6.6: Luminosity comparison for our 3D simulations. The different colors show different models, the different linestyle refers to different assumptions for the inner emitting radius $r_{\rm em}$. The black points show the luminosities observed by Pfuhl et al. (2015).

6.3 Discussion

6.3.1 Resolution and numerical issues

As already mentioned in Sec. 6.2.3 (and considering the discussion in Sec. 4.2), the constraining power of the absolute value of the Brγ luminosity has to be reconsidered, after the systematic study of the present 3D simulations. First of all, the shocked material has a very filamentary nature; hence, if the shell and filaments are not properly resolved, the density of the shocked material is reduced significantly. Furthermore, as shown in Fig. 6.7 and 6.8, the shocked material is efficiently mixing with the atmosphere, moving to

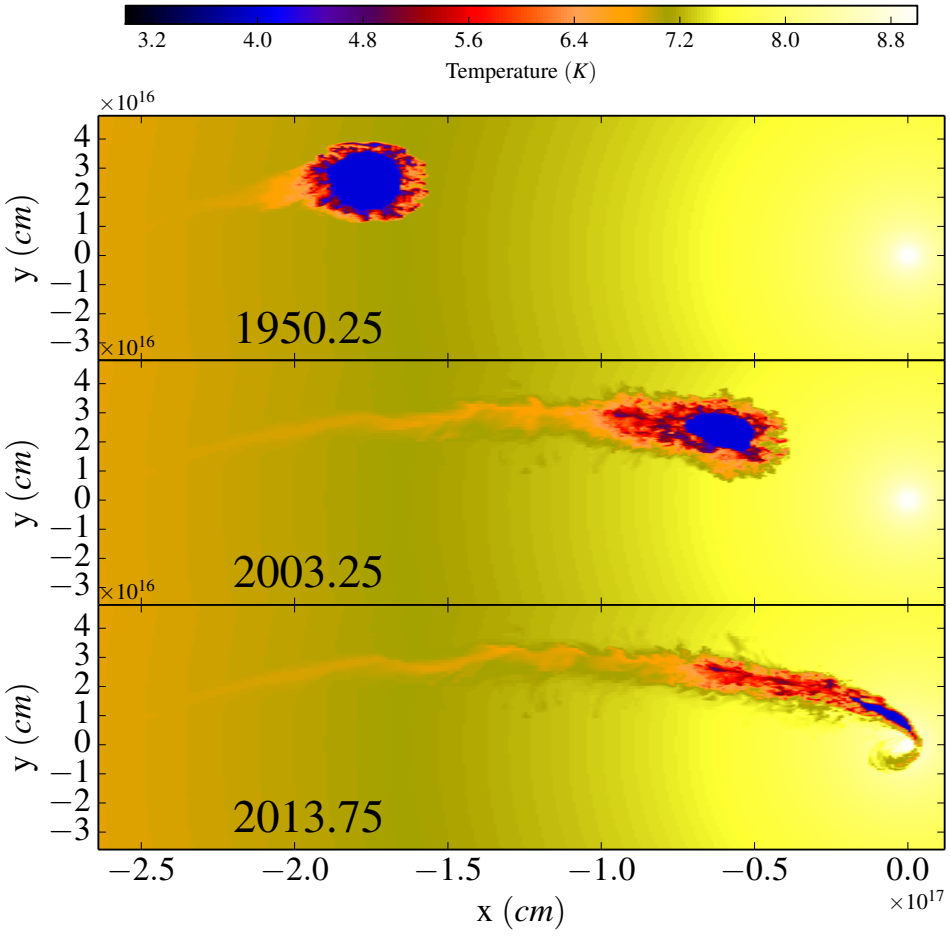

Figure 6.7: Temperature maps for the 3D standard model. The domain plotted is a slice at z=0.

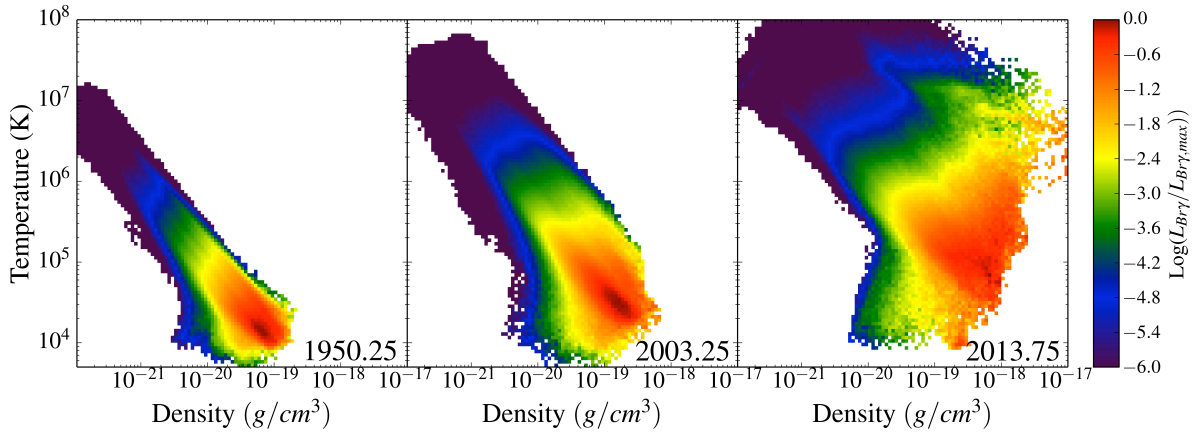

Figure 6.8: Phase plots for our 3D standard model. Only the shocked material is included.

lower densities and higher temperatures. In particular, as visible in Fig. 6.7, at early stages (e.g., in year 1950.25) the material closest to the free-wind region is at temperatures of around 10^4 K, i.e. the temperature of the injected material. However, the mixing becomes faster and faster as the source reaches its pericenter: in year 2013.75, most of the shocked material is immediately increasing its temperature and a relatively small fraction is at temperatures below 10^5 K. The evolution of the phase plots for the shocked material in Fig. 6.8 might be misleading, since the most luminous material is denser as the source approaches pericenter; however, this is due to the fact that the outflow moves faster and it encounters higher density/pressure material on its way to the black hole. So, it is compressed more and reaching higher densities, as it gets closer to SgrA* (see also Fig. 6.1). On the other hand, the inner atmosphere is also hotter, hence the mixing leads to a large spread of the shocked material in the density-temperature phase space. However, this mixing is somehow resolution dependent, since its nature is partly numerical (see chapter 3). This has already been shown in Schartmann et al. (2015) for the diffuse cloud scenario. In the case of the present outflow model, mixing and resolution are significant all along the orbital evolution, given the highly filamentary nature of the emitting material, and the effect of poor resolution is even less predictable. The upper panel of Fig. 6.9 shows histograms for the luminosity of our standard model as a function of the density of the emitting material, in year 2003.25 (i.e., the central panel of Fig. 6.8 collapsed along the temperature axis). The same histogram is plotted also for the simulation stLOWRES (the same as our standard model, but with half of the resolution) and for the simulation st2D (the same as the standard model, but in a 2D cylindrical fixed grid; see Table 6.1). The luminosity distribution peaks around densities of roughly 10^{-19} g cm^{-3} for the outflow parameters of these three simulations. Though small, some discrepancy occurs between the two 3D simulations at different resolutions, particularly close to the peak of the distribution.

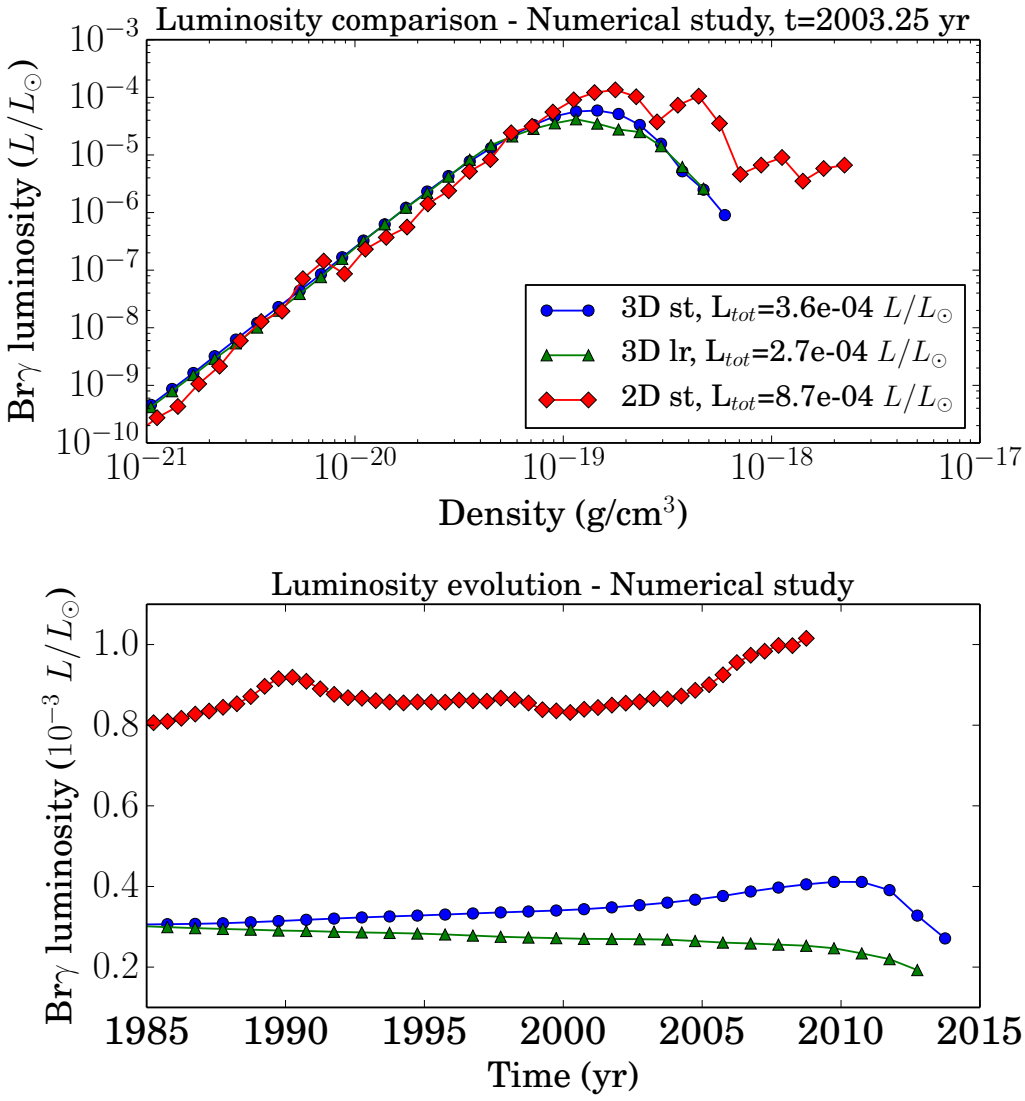

Figure 6.9: Luminosity comparison for our numerical study. Upper panel: contribution to the total luminosity by different density bins, in year 2003.25, for the standard model (blue circles), stLOWRES (green triangles) and st2D (red diamonds). Lower panel: luminosity evolution, close to pericenter, for the standard model, stLOWRES and st2D. Colors and symbols are the same as in the upper panel.

This is able to account for the difference in the luminosity evolution, close to pericenter (see the lower panel of Fig. 6.9), between our standard model and model stLOWRES. The effect of resolution on the luminosity evolution is similar to the one visible in the resolution study of Schartmann et al. (2015). A way more significant difference occurs, instead, between the luminosity curves of our standard model and its two-dimensional counterpart st2D. As already discussed in Ballone et al. (2013), simulations in 2D cylindrical coordinates suffer from some intrinsic numerical issues: in particular, the accumulation of material towards $R = 0$, due to the tidal field of the SMBH, is artificially enhanced by the cylindrical symmetry and by the necessary reflective boundary conditions close to the axis of symmetry (see Sec. 5.3.1). For this reason, in order to compare with our standard model, we removed all the material at $R < 1.25 \times 10^{14}$ cm. However, still a significant contribution to the luminosity of st2D comes from densities higher than 2×10^{-19} g cm^{-3}, while this is not the case for the 3D standard model. Hence, the artificial compression towards the axis of symmetry might have an effect on even larger distances from the axis. Furthermore, given the cylindrical symmetry, in the calculation of the luminosity the volume of every cell is obtained by a rotation of the cell around the z axis (i.e., every cell has to be thought as a 3D annulus). As a consequence, the dense Rayleigh-Taylor fingers forming immediately around the free-wind region might have a larger volume filling factor, compared to their 3D more realistic counterparts. All in all, there is a factor ≈ 2.5 difference between the standard model and st2D, which maybe forces us to carefully reconsider the luminosity curves obtained in our 2D study.

6.3.2 Comparison with previous works

There are some differences between the 2D simulations presented in chapter 5 and the present ones. The first one is that the orbit has been updated from the one derived by Gillessen et al. (2013a) to the most-recent one derived by Gillessen et al. (2013b). The most up-to-date orbit has an orbital time and an apocenter distance that are roughly a factor of two larger than the one of the previous 2D simulations. This had the unfortunate effect of increasing the computational domain and double the integration time of our simulations, making the new simulations even more computationally expensive than previously expected.

Further, compared to Ballone et al. (2013), the mass-loss rate of our standard model has increased by roughly a factor 5. This has been induced by the need of matching the PV diagrams shown in Fig. 6.2. In fact, the parameters of the best model in Ballone et al. (2013) are roughly corresponding to the LMDOT3D model described in Sec. 6.2.3, which is not able to match the size of G2 in the observed PV diagrams (see Fig. 6.5). The increase in the mass-loss rate of the best model is probably due to the more accurate comparison performed here, as well as to intrinsic differences between 2D and 3D simulations. Additionally, there are major differences in the absolute value of the luminosity, as discussed in Sec. 6.3.1, due to differences in the resolution and perhaps in intrinsic differences between 3D cartesian and 2D cylindrical coordinates.

The choice of starting the simulations at apocenter makes the present results also very

different from the ones in De Colle et al. (2014). In fact, the $\approx$ 200 yr evolution of our models (compared to the 3 and 20 yr chosen by De Colle et al., 2014) leads to a much more extended distribution of gas, as a result of the prolongated stripping of the RTI filaments of shocked wind. This larger filling volume is fundamental for matching the observed PV diagrams. However, no major instability forms in the simulations of De Colle et al. (2014), probably as a result of the too short evolution time of their models.

Major differences between our simulations and the ones in De Colle et al. (2014) also arise around pericenter, where the bow-shocks in their simulations - particularly those starting 3 years before pericenter - are becoming broader and underdense after the pericenter passage. This might be a consequence of their more sophisticated treatment of radiative cooling. The difference might also arise from the fact that, for those simulations, De Colle et al. (2014) did not artificially stabilize their atmosphere. This is allowing to compute the bow shock dynamics more properly, but it has the side effect of allowing the atmosphere to become convectively unstable (as clearly visible in Fig. 1 of De Colle et al., 2014).

Our work is also complementary to that by Zajaček et al. (2016). In this work, the evolution of the stellar wind shock is studied by means of the analytic solution of Wilkin (1996). Such estimates have the advantage of having a simple but "linear" description of the interaction between the wind and the surrounding atmosphere; however, they lack more complex hydrodynamic processes that already arise from our simulations, even with our relatively simple physical treatment.

We must also point out that, besides lacking the detailed procedure to mock the instrumental effect on the processing of the simulation, the mock Brγ maps and the PV diagrams shown in Ballone et al. (2013), Gillessen et al. (2013b) and De Colle et al. (2014) include all the outflow material present in the simulations. This choice is arbitrary, since it depends on how much of the free-wind region is actually resolved in the simulation, and can produce PV diagrams with Brγ fluxes that are spanning several order of magnitudes, in evident inconsistency with the observations (compare to the upper panel of Fig. 6.2). Furthermore, as discussed in Sec. 4.2 and further on, the Brγ luminosity of a $1/r^2$ density distribution depends on how much of it is actually ionized. Our more detailed post-processing of the simulation clearly shows that a more careful interpretation of the results must be applied, when dealing with this scenario.

Finally, even considering the weak constraining power of the Brγ luminosity, the present study shows that there should be a significant effect of the outflow parameters on the total luminosity of the shocked gas. Hence, the present standard model and the one in chapter 7 are mutually exclusive. The latter has the advantage of being able of reproducing both G2 and its tail G2t at the same time. The present standard model, on the other hand, is only able to reproduce G2, but it seems to have a Brγ luminosity that is closer to the observed one.

6.3.3 On the nature of the source

The best parameters found via 2D simulations were compatible to those of a T Tauri star. However, the parameters of the present 3D standard model ($\dot{M}_{\rm w} = 5 \times 10^{-7} {\rm M}_\odot$ yr^{-1} and $v_{\rm w} = 50$ km s^{-1}) are somehow at the extreme end of the observed ranges for T Tauri's winds, which are $\dot{M}_{\rm w} = [10^{-12}, 10^{-7}]$ M$_\odot$ yr^{-1} and $v_{\rm w} = [50, 300]$ km/s from the observations (White & Hillenbrand, 2004). Given the short evolution time of our models ($\approx$ 200 yr), the standard model parameters could still correspond to a phase of exceptionally higher mass-loss. Indeed, there is a well established correlation between mass accretion and outflow rates for T Tauri objects, possibly being the consequence of outflows launched from the proto-stellar accretion disk (e.g., White & Hillenbrand, 2004; Edwards et al., 2006). In such a crowded environment and given the high tidal field of the black hole, the accretion (and outflow) rates might be enhanced compared to the typical star forming regions. Extremely massive outflows have been discovered, as e.g. for the case of DG Tau (Günther et al., 2009a; White et al., 2014). This problem can also be partially "cured" by assuming that the outflow is biconical, i.e., it is not occupying the full solid angle. As widely shown in literature, this is indeed a much more realistic assumption for the outflows from this kind of young stellar objects. In this case, Eq. 4.9 becomes

$$R_{\rm out,conical} = \left[\frac{\dot{M}_{\rm w} v_{\rm w}}{4\pi(1 - cos\theta_{\rm open}) P_{\rm amb}} \right]^{1/2}, \tag{6.1}$$

where $\theta_{\rm open}$ is the half opening angle of the outflow. So, for the same value of $R_{\rm out}$, in the case of a biconical outflow, $\dot{M}_{\rm w}$ can be a factor $(1 - cos\theta_{\rm open})$ (i.e., up to a factor $\approx 10^{-2}$ for half opening angles as small as $\approx 10°$) smaller compared to the isotropic case tested here. As shown in Sec. 6.2.3, the stagnation radius is on a 0th order responsible for the size of the outflow; hence, to get sizes similar to the observed ones, lower mass-loss rates could be needed, compared to the ones found in our current simulations. However, the orientation of the biconical outflow with respect to the orbit is also likely effecting the distribution of the emitting material. This would add a further parameter to the present scenario and additional dedicated simulations would be needed to clarify this issue.

6.4 Conclusions from the 3D simulations

From the present 3D study (and considering the 2D study in chapter 5, we can draw the following strong conclusions:

1. relatively massive ($\dot{M}_{\rm w} = 5 \times 10^{-7}$ $M_\odot$ yr^{-1}) and slow, compared to main-sequence stars, (50km s^{-1}) outflows are needed to reproduce the emission properties of G2; this suggests that a possible source for G2 is a young stellar object, like a T Tauri star.

2. the appearence of such an outflow in the PV diagrams is strongly dependent on how much of its unperturbed region is actually emitting; if the material at distances

smaller than roughly 100 AU from the source dominates the emission, G2 would always look too compact - both in size and in velocity - compared to the observations.

3. a reasonable comparison to the current SINFONI observations can be obtained both by the diffuse cloud simulations in Schartmann et al. (2015) and by the present ones. However, we might be able to understand whether G2 is generated by a source or if it is a simple gas-dust diffuse cloud in the next 5-10 years. For the case of a compact source, we should then be able to observe a decoupling between the dust and gas components and a new and "fresh" G2 should reform around the dusty one, later on.

Inspired by model HV3D, we investigated the ability of a high velocity outflow to simultaneously reproduce G2 and its tail G2t. As discussed in sections 5.2.2, 6.2.3 and 6.3.2, high velocity outflows should produce too low luminosities. However, Sec. 6.3.1 also shows how the absolute value of the simulated luminosity might be a too weak parameter to rely on. HV3D, on the other hand, strikingly showed that high velocity models can produce a bimodal emission in the observed PV diagrams. In chapter 7 we will specifically focus on this possibility.

Chapter 7

An outflow to explain the G2+G2t complex

In this chapter we will present a short study of an a high velocity outflow to simultaneously explain G2 and G2t. The discussion of the results will require a more detailed focus on all the processes affecting the structure of the outflow, particularly those that could not be captured by the simple 1D simulations in Sec. 4.1. This is an adaptation of Ballone et al. (2016), published in *The Astrophysical Journal Letters*.

7.1 Simulation setup

The setup of the simulations presented in this chapter is essentially the same as the one presented in Sec. 6.1. In this case, the computational domain ranges from $(-3.0\times10^{17}; -7.2\times10^{16}; -7.2\times10^{16})$ cm to $(3.6\times10^{16}; 7.2\times10^{16}; 7.2\times10^{16})$ cm in (x,y,z) coordinates, with a finest resolution of $\Delta_{x,y,z,min} = 5\times10^{14}$ cm.

7.2 Results

7.2.1 The model

The model has mass-loss rate $\dot{M}_{\rm w} = 5\times10^{-7}\ M_{\odot}{\rm yr}^{-1}$ and velocity $v_{\rm w} = 400$ km s^{-1}. These values are roughly compatible with those of T Tauri stars (see Sec. 7.4). The left panel of Fig. 7.1 shows a density map in the orbital plane in the year 2012.75. The structure is, again, the same as for the models presented in chapter 5 and 6. The outflow is composed of a free-flowing region and of a very dense and narrow shell, highly prone to Rayleigh-Taylor instability (RTI). RTI leads to the formation of long fingers; those perpendicular to the orbital motion are easily stripped by the atmosphere's ram pressure. The stripped material, along with the shocked material that is naturally placed there, tends to accumulate in a following tail. This is a general result, in case of efficient ram pressure stripping (e.g., Pittard et al., 2005; Vieser & Hensler, 2007; Cooper et al., 2009; Banda-Barragán et al.,

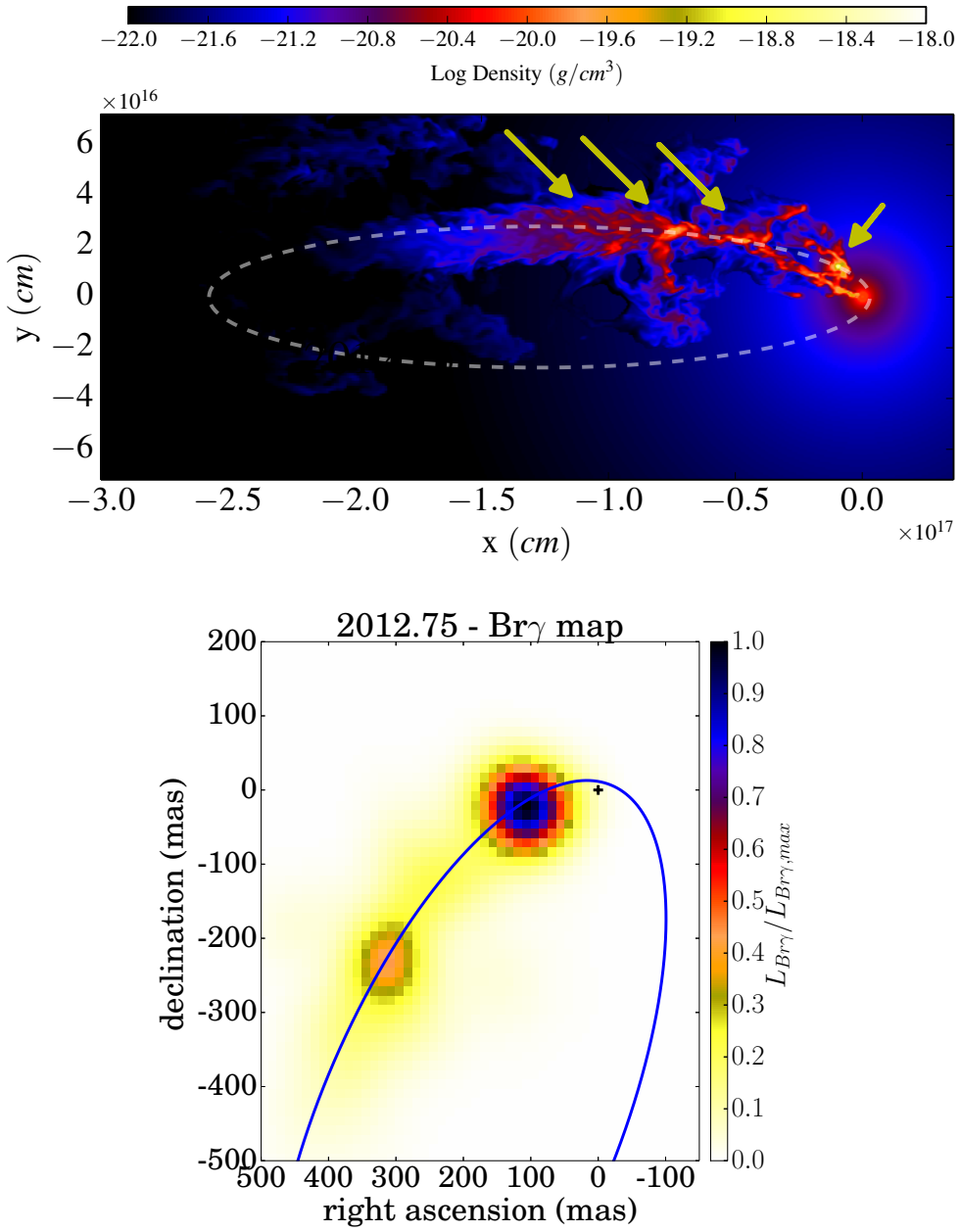

Figure 7.1: Upper panel: Density map for the hydrosimulation in year 2012.75, within the orbital plane $z = 0$. The transparent white dashed line marks G2's orbit. The short arrow points at the position of the bow shock, while the three long arrows show the position of the tail. Lower panel: Brγ map of the simulation in year 2012.75, projected on the plane of the sky. The blue solid line marks G2's orbit, the black plus sign shows the location of SgrA*. The interaction with the surrounding atmosphere leads to the formation of a two-component structure.

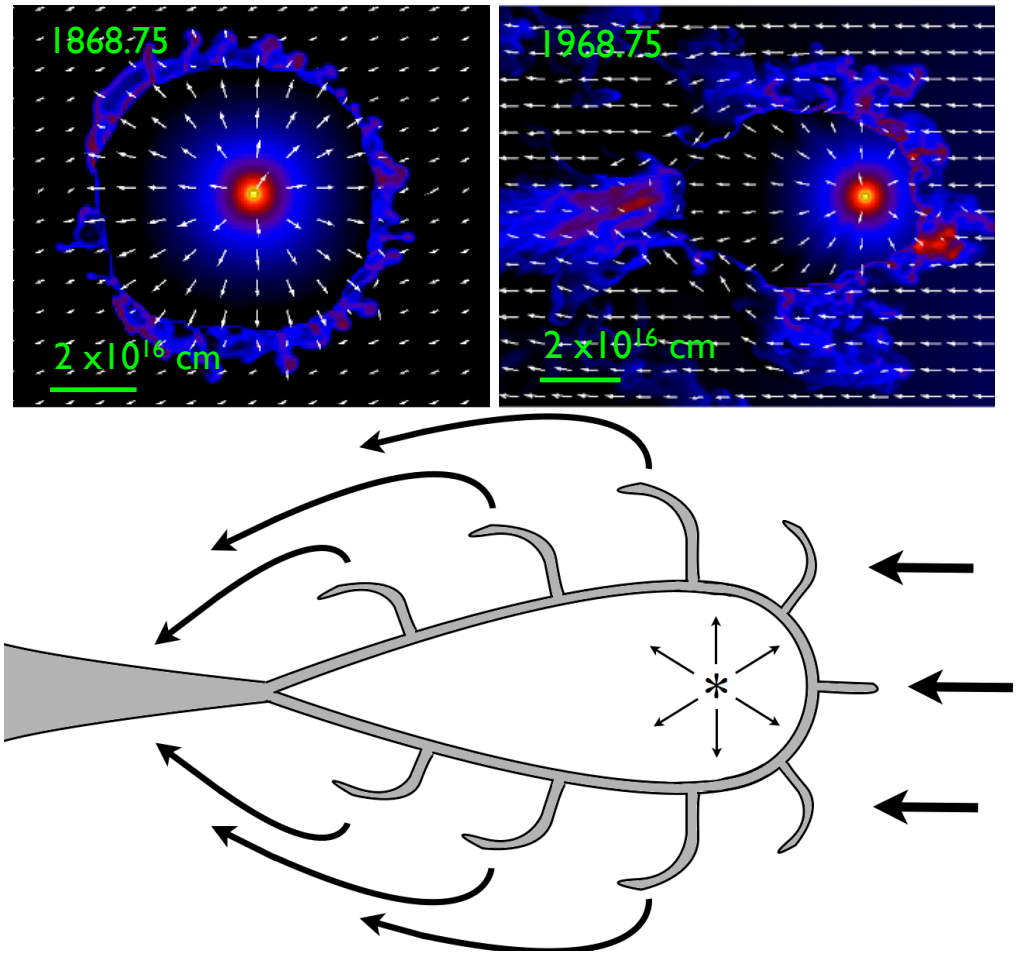

Figure 7.2: Upper panels: density cuts of our simulation, showing its evolution. The arrows (with arbitrary length) trace the velocity field, after a subtraction of the velocity of the source. The color bar is the same as in Fig. 7.1. Lower panel: sketch of the outflow's evolution at late time (see text).

2016; Christie et al., 2016) and it is visible in the density cuts and the sketch in Fig. 7.2. Only when the RTI and the successive stripping are efficient, the outflow results in a clear bimodal density distribution and Brγ map (Fig. 7.1): G2 is produced by the leading termination shock and G2t by the trailing one. Whereas the leading standoff distance is given by the ram pressure balance, the position of the trailing termination shock depends on the interplay between several physical processes.

- **The thermal pressure of the external medium:** deviating from the classical theory (Wilkin, 1996), the expansion of an (undisturbed) stellar wind in the backward direction into a high pressure environment stalls when the equilibrium of the winds

ram pressure and the atmosphere's thermal pressure is reached (see Sec. 4.1 and Christie et al., 2016).

- **The density of the shocked material:** for fixed $\dot{M}_{\rm w} v_{\rm w}$, faster outflows are less dense (see Eq. 4.2) and the same applies to the shocked material. Hence, $\rho_{\rm w}/\rho_{\rm at}$ is lower, the hydrodynamical instabilities grow faster and the deceleration of the shocked material by ram pressure is higher. The latter has a big role in the amount of material accumulating in the tail, while the former is effecting the position of the trailing termination shock (see Christie et al., 2016).

- **The strong gravity of the SMBH:** the tidal field is also an important ingredient in affecting the structure of the termination shock, this being defined by momentum balance; furthermore, the tidal force confines the stripped material towards the orbit.

- **The time-position dependence of the source velocity and of the atmosphere parameters:** the source moves on a very eccentric orbit and thereby encounters different densities and pressures of the external medium. As a result, the interaction outflow-atmosphere never occurs in a steady-state. E.g., close to apocenter the stripping and the tidal force are always less efficient. If the outflow starts too close to pericenter, the stripping will last for a shorter time and create a less elongated tail. Additionally, the termination shock might still be in an expansion phase (rather than readjust to smaller sizes, as expected for an increase of thermal and ram pressure). If the source has already completed one orbit and it is towards its second pericenter passage, the stripping might have formed a significantly longer tail right before and after the previous pericenter passage. However, the building up of the tail would occur during the whole orbital time ($\simeq 400$ yr) and, in such a timescale, the interaction with the external medium is expected to remove the tail's angular momentum and move it on a significantly different orbit.

As already underlined in the rest of this dissertation, this complexity clearly expresses the need for hydrodynamical simulations. We refer the reader to the parameter study in chapter 5 and 6, to understand how the termination shock can be effected by the combined processes discussed before, leading to different separations between the leading termination shock and the tail.

Further ingredients are missing in the present simulation. For example, magnetic fields can suppress the growth of instabilities and the mixing of the tail with the environment. Thermal conduction could instead lead to increased mixing. Resolution has also an effect in these terms. Finally, we must stress that the parameters producing our best model are dependent on the assumed atmosphere, but the latter is also very uncertain. Hence, some caution must be used in considering the constraining power of the present simulation. Still, this represents a needed first step in the investigation of such a scenario.

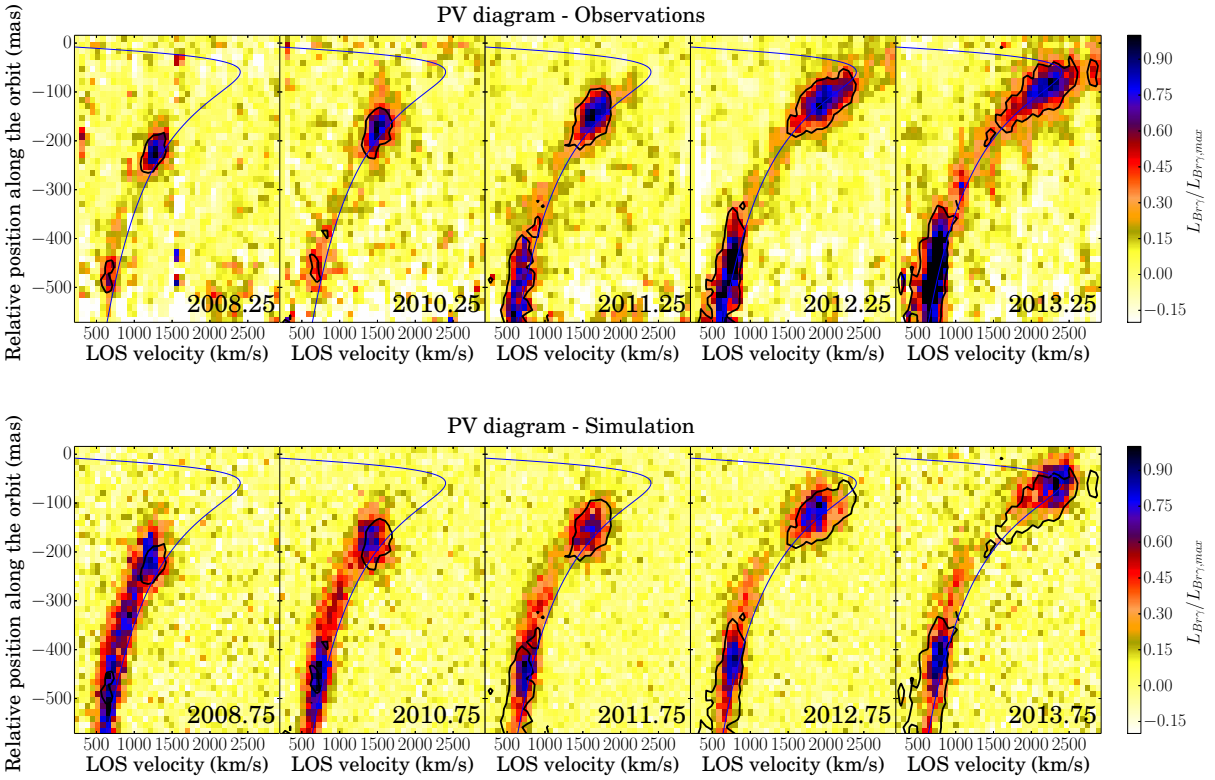

Figure 7.3: Series of observed (top) and simulated (bottom) PV diagrams from 2008 to 2013. The blue line represents G2's orbit as derived from observations, while the black (arbitrary) contours mark the observed positions of G2 and G2t. A time-shift of half a year is applied for the simulations (see text).

7.2.2 Comparison with the observations

The 3D simulation presented here allows us to construct realistic PV diagrams (see Schartmann et al., 2015, for a detailed description of the used method). In the case of an outflow scenario, the luminosity of the free-flowing region should diverge with decreasing distance r from the central source (cf. Eq. 4.1 and Eq. 5.1). In the high resolution 2D simulations of chapter 5, most of the luminosity comes from the shocked material, even when a small inner emitting radius for the free-flowing region is chosen. Additionally, the simple estimates in Sec. 4.2 and the results in chapter 6 show that the shocked shell might be very efficient in "shielding" the free-flowing region from ionizing photons coming from the massive stars around G2 and that only the outer parts of the free-flowing material are probably emitting. Hence, for this analysis, we just consider the Brγ emission from the shocked outflow material.

A series of observed and simulated PV diagrams is shown in Fig. 7.3. Given the

complexity of the outflow's structure, the very idealized nature of the simulation and the limited resolution, we restrict ourselves to a simple qualitative comparison. The major feature of the model is the ability to produce a bimodal emission in the PV diagrams, with the two peaks being located roughly at the correct position compared to observations. We find that we must apply a time-shift of half a year between the observations and the output of the simulation for the best match with the observations. This is due to the fact that part of G2's Brγ emission is produced by the bow shock surrounding the source in the front but also laterally, so that the source is not exactly placed in the middle of the emitting spot (see also Sec. 5.2.1 and 6.2.1). Given the estimated orbital time of ≈ 400 yr, this is a minor correction.

Another interesting feature is the presence of more tenuous material connecting G2 and G2t. This is produced by some of the shocked material on the back part of the free-flowing region, as well as by some of the trailing material, though with a smaller flux.

As a final remark, G2 appears brighter than G2t in simulated Brγ maps (see the right panel in Fig. 7.1), whereas this is not the case in the PV diagrams. This is partially due to the fact that the part of the orbit in which G2 sits has a very small slope in PV space. Hence, in PV diagrams, G2's luminosity is diluted over several velocity bins. G2t's luminosity is also lowered by mixing with the atmosphere, as discussed in the next section.

In conclusion, the simulation can reproduce quite well the two emitting spots and the separation between them. However, there exist differences between the observations and the simulations in the relative luminosity of G2 and G2t. We find that the simulated tail is brighter than observed at early times, while it is slightly underluminous at late times. These issues will be discussed in the next section.

7.3 How to reconcile the observed and the simulated PV diagrams?

Though the global structure of the G2+G2t complex is nicely reproduced by the simulation, a significant mismatch is present in terms of relative brightness of G2t with respect to G2 (see Fig. 7.3). According to the last observationally derived PV diagrams, G2t *appears* to be flaring up. In fact, a simple dynamical argument is sufficient to rule out the absence of G2t, in 2008 and 2010, from the region of the PV space at positions < 350 mas: G2t can not dynamically "enter" the PV diagrams in the short time interval between 2010 and 2011 observations. However, one of the main reasons for this mismatch might reside in the observational techniques used to extract PV diagrams. The position along the orbit is determined using a curved slit, currently following G2's best-fitting orbit (see Gillessen et al., 2013a; Schartmann et al., 2015, for details on the method). The obtained brightness of the tail depends on the chosen slit. For example, G2t's flaring could be explained by slightly different orbits of G2 and G2t (for an indication of this, see Fig. 3 in Pfuhl et al., 2015) and G2t might have been progressively "entering" the slit, particularly at late times. More extended observations and analysis are needed to determine the exact structure of

the tail and its connection to G2 (P. M. Plewa et al., 2016, in preparation). For our model, however, all the emitting material is projected onto the orbit by construction, so it will always fully appear in the simulated PV diagrams.

An explanation for the lower simulated emission of G2t at late times probably resides in the mixing between the outflow material and the atmosphere. The mixing of outflow material with the hot atmosphere decreases its density and increases its temperature, thus reducing its overall luminosity (see Sec. 6.3.1 and Schartmann et al., 2015, for a more detailed discussion on this issue). This effect is more severe for G2t, which is the result of the accumulation of stripped shocked material. However, mixing depends critically on various uncertain parameters, as discussed in Sec. 7.2.1.

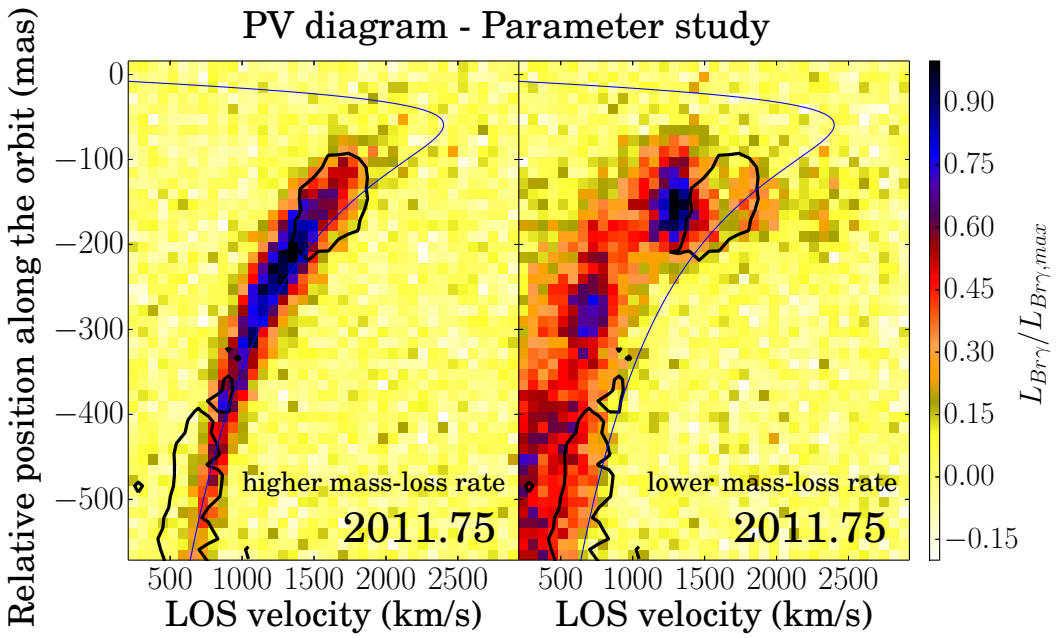

Figure 7.4: Simulated PV diagrams for the year 2011.75 for model A (left panel) and model B (right panel) of our parameter study. Neither is able to account for the observations.

7.4 Discussion

A small parameter study showed that the model presented here might be the best (and unique) model able to match the observations for our assumptions. In this parameter study we kept the quantity $\dot{M}_{\rm w} v_{\rm w}$ constant and we increased and decreased $\dot{M}_{\rm w}$, producing two models with $\dot{M}_{\rm w} = 2 \times 10^{-6}\ M_{\odot}{\rm yr}^{-1}$, $v_{\rm w} = 100$ km s^{-1} (model A) and $\dot{M}_{\rm w} = 2 \times 10^{-7}\ M_{\odot}{\rm yr}^{-1}$, $v_{\rm w} = 1000$ km s^{-1} (model B), respectively. PV diagrams for the year

2011.75 are shown in Fig. 7.4. In the case of model A, the free-flowing region is larger and stripping is not efficient enough to form a tail. Thus, the object appears larger in the PV diagrams, but no bimodal distribution of the emitting material occurs. For model B, the stripping of the shocked material is more significant and the size of the free-flowing region is reduced in the trailing side by the backflow. As a result, the separation between the head and the tail is not as a sharp as in our reference model and all the emitting material is shifted to lower velocities compared to the orbit derived for G2 and G2t. We then infer that only relatively small variations of the parameters, around our standard model, are allowed.

As in Scoville & Burkert (2013) and in the studies described in chapters 5 and 6, the most reasonable source associated with the obtained parameters ($\dot{M}_{\rm w} = 5 \times 10^{-7}\ M_{\odot}{\rm yr}^{-1}$, $v_{\rm w} = 400$ km s^{-1}) is a T Tauri star. Observations put the wind parameters for T Tauri objects in the ranges $\dot{M}_{\rm w} = [10^{-12}, 10^{-7}]\ M_{\odot}{\rm yr}^{-1}$ and $v_{\rm w} = [50, 300]$ km s^{-1} (White & Hillenbrand, 2004), placing our favorite model at the boundary of the distribution or even beyond. However, as discussed, many parameters of our model are uncertain and this can reflect on the outflow parameters. Exceptionally massive and fast outflows do anyway exist (as in the case of DG Tau; Günther et al., 2009b; White et al., 2014) and relatively high mass-loss rates are probably needed to reproduce the observed luminosity (and estimated mass) of G2. Hence, the most plausible candidate needed for such a scenario would be in any case a T Tauri star, since higher mass stars or different evolutionary states would result in extremely different outflow parameters or they would be detected by the current instruments.

7.5 Conclusions for the high velocity outflow scenario

The present model is for the first time able to reproduce both G2 and its trailing tail G2t in a detailed comparison with the observed PV diagrams. If the source is a T Tauri star, it could naturally explain the presence of dust embedded in G2. Furthermore, if the material launched in the outflow is also dusty, it would explain the more moderate MIR emissions seemingly associated to G2t (Pfuhl et al., 2015).

On the other hand, the present model neglects the discovery of the cloud G1, that seems to be associated with the former objects. We stress here that the connection between G1 and the G2+G2t complex is still very speculative and only future observations will clarify this point. Additionally, as discussed in Sec. 7.4, there are some issues in reconciling the parameters obtained to match the observed PV diagrams with the parameters of a physical T Tauri.

While there is still some tension with the observations, the present model is able to qualitatively (and, partially, quantitatively) reproduce G2 and G2t, offering a valuable potential explanation for these objects.

Chapter 8

Discussion and outlook

In this chapter we will try to put our work in a broader framework, discussing the limitations of an hydrodynamical study of G2 (Sec. 8.1), the possible nature of G2's source (Sec. 8.2) and the advantages and disadvantages of a "compact source" scenario, in comparison to the other currently available models, (Sec. 8.3). In Sec. 8.4 we will discuss the possible future studies that are immediately connected to the ones presented in this dissertation.

8.1 Validity of the hydrodynamical approach

As mentioned in chapter 3, studying the hydrodynamical evolution of G2 has been a natural choice, given its gaseous nature.

A major caveat for this and other studies of G2 is, however, the validity of the fluid approximation. The basic assumption to be made is that the gas behaves as a continuum and that its properties are well described by "statistical" quantities - such as density, temperature, etc. - over *control volumes* that can be considered small enough (infinitesimal) compared to any important scale Λ of the problem. The latter condition can be quantified by comparing Λ to the mean free path λ of the gas particles, i.e., $\lambda << \Lambda$. In this case, the gas is also called "collisional". The Coulomb mean free path is

$$\lambda \approx 10^{16} \left(\frac{T}{10^7 \text{ K}}\right)^2 \left(\frac{n}{100 \text{ cm}^{-3}}\right)^{-1} \text{ cm}, \tag{8.1}$$

where T and n are the temperature and number density of the gas, respectively.

If we evaluate it for the hot gas in the central pc of the Galactic Center, with $T \approx 10^7$ K and $n \approx 100$ cm^{-3} (see Sec 1.1.3), we realize that it is bigger than the radius of G2, i.e. $R_c \approx 10^{15}$ cm (see Sec. 2.2.1), and G2 should not "collide" with its environment in a hydrodynamical sense. The same caveat applies to many other astrophysical problems, such as jets interacting with the hot gas in the halo of elliptical galaxies, groups and clusters (e.g., McNamara & Nulsen, 2012), where the mean free path is usually larger than the typical widths of the observed jets, or for accretion flows (such as those mentioned in Sec. 1.3.2), where the mean free path might be larger than the Schwarzschild radius

or the physical size of the accreting object (e.g., Chandra et al., 2015). Even certain processes in the solar and stellar winds might encounter similar issues. In many cases, however, the fluid approximation is still used and the usual assumption for justifying the hydrodynamical approach is that small scale magnetic fields can make the plasma collisional on scales smaller than the Coulomb mean free path, i.e., on distances of the order of the gyroradius of the particles (Blandford & Rees, 1974; Dexter, 2011). Indeed, a hydrodynamical description of the previously mentioned problems is often very effective in explaining many observational evidences. For example, this might also be the case for the observed bow shocks from stars in the clockwise disk (see Sec. 1.2.1), that need an hydrodynamical interaction of their winds with the surrounding ionized and hot medium (see Sec. 1.1.2 and 1.1.3).

8.2 The nature of the source

As already mentioned in chapter 2, the spectral properties of G2 exclude its association with a massive star (such as the S-stars, see Sec. 1.2.2). At the same time, the mass loss rate needed to match the observed size of G2 in the PV diagrams is always $\dot{M}_{\rm w} \gtrsim 10^{-7} {\rm M}_{\odot}$ yr^{-1}, which is too high for typical winds of low-mass stars in their main sequence phase. Low-mass stars in their asymptotic giant branch or red giant phases might have comparable high mass loss rates (see, e.g., Lamers & Cassinelli, 1999; Whitelock et al., 2016). Stars in these phases have a giant envelope, that usually leads to outflow velocities of the order of their escape velocities, i.e., few tens of km/s. This is indeed the case of the models that best reproduce G2's size in the PV diagrams (see chapters 5 and 6). However, those stars would appear too bright in K_s band, compared to G2.

The most appealing possibility is that the source is instead a young star, such as a T Tauri. These objects are also producing winds, but they have much lower luminosities in K_s band (see discussion in Scoville & Burkert, 2013). Typical wind mass loss rates and velocities - as derived from observations - are $\dot{M}_{\rm w} = [10^{-12}, 10^{-7}]$ M$_{\odot}$ yr^{-1} and $v_{\rm w} = [50, 300]$ km/s (e.g., White & Hillenbrand, 2004). Our best parameters are a bit extreme, particularly in terms of our resulting mass-loss rate, but extremely massive T Tauri outflows have been discovered, as, e.g., for the case of DG Tau (Günther et al., 2009a; White et al., 2014). As already discussed in Sec. 6.3.3, the standard model parameters could still correspond to a phase of exceptionally higher mass-loss, particularly considering the short evolution time of our models ($\approx$ 200 yr). Indeed, there is a well established correlation between mass accretion and outflow rates for T Tauri objects, possibly being the consequence of outflows launched from the proto-stellar accretion disk (e.g., White & Hillenbrand, 2004; Edwards et al., 2006). The inner parsec of our Galaxy is an extremely crowded and complex environment (see chapter 1) and the supermassive black hole produces a strong tidal field; both might enhance the accretion (and outflow) rate, compared to typical star forming regions. The problem of very high derived mass loss rates can also be partially "cured" by assuming that the outflow is biconical, i.e., it is not occupying the full solid angle. In this case, $\dot{M}_{\rm w}$ can be a factor $(1 - \cos\theta_{\rm open})$ (i.e., up to a factor $\approx 10^{-2}$

for half opening angles as small as $\approx 10°$) smaller compared to the isotropic case tested here (see discussion in Sec. 6.3.3). Since the stagnation radius is on a 0th order responsible for the size of the outflow, lower mass-loss rates could lead to similar sizes of G2.

Interestingly, T Tauri stars have ages between 10^5 and 10^7 yr (see, e.g., D'Antona & Mazzitelli, 1994). These values are comparable with the age of the clockwise disk (2.5-8 Myr; see Sec. 1.2.1 and Paumard et al., 2006; Do et al., 2013; Lu et al., 2013). The disk and G2 have also a similar orbital plane and G2's apocenter is within the disk (see Sec. 2.1). This could indeed suggest that the source of G2 has formed there and has been successively scattered on the current G2's orbit by multiple encounters with other stars in the disk, as already suggested by Murray-Clay & Loeb (2012).

8.3 Advantages and disadvantages of a compact source scenario and comparison to other models

As shown by the present study, the compact source scenario is a highly parametric model, which makes the results strongly dependent on the assumptions made. Its intrinsic properties also make its study numerically challenging. Occam's razor would then suggest us that a diffuse cloud scenario (as the one originally proposed by Gillessen et al., 2012, see Sec. 2.2.1) is to be preferred. However, more parameters can always offer more possibilities to reconcile the model and the observations.

For example, Pfuhl et al. (2015) showed that the total mass of the dust embedded in G2 is probably too low to make this component dynamically important. On the other hand, Witzel et al. (2014) showed that the dust stays compact even close to pericenter, compared to its gaseous counterpart. It is not clear why this should happen in a diffuse cloud scenario. An outflow nature for G2 has the advantage of explaining both the extended (in position and velocity) nature of the gas component and the compactness of the dusty emission, if the latter is associated to a central young stellar object.

Another open question is related to the high eccentricity of G2's orbit. This could be well explained by a formation of G2 in colliding winds in the disk, if G2 is a clump of diffuse gas (Burkert et al., 2012; Schartmann et al., 2015; Calderón et al., 2016). Compared to stars, gas can more easily lose angular momentum (and energy) and the collision of stellar winds represents a very effective process, in this sense. However, the inner parsec is also very crowded with young stars and the S-stars can have similar orbital semi-major axes and can reach similarly high eccentricities.

A connection to a star could then be possible. The binary merger model of Witzel et al. (2014) could explain the dust properties and the high eccentricity of G2 (as later shown by Prodan et al., 2015; Stephan et al., 2016), but so far neglected the existence of a significant gaseous component associated with it. Outflow models are often invoked to explain the latter (see Sec. 2.2.2), but often they rely on - sometimes, too simple - analytical estimates. Despite the many limitations discussed in this and previous chapters, we believe that our study represents the most complete attempt to include the several

(often non-linear) processes involved in a compact source scenario and to compare to the observed properties of G2, e.g., by means of accurate mock PV diagrams.

Concerning the possible connection of G2 to G2t and G1 (see Sec. 2.1), we believe that the currently most powerful model is the one by Guillochon et al. (2014a), invoking the tidal disruption of the outer envelope of a giant star by the tidal field of SgrA*. Hydrodynamical simulations of these tidal disruptions of stars by SMBHs indeed show that these events might lead to the formation of a bound debris, streaming towards the SMBH on highly eccentric orbits (see also Guillochon et al., 2014b). A fragmentation of this streamer might have led to G1, G2 and G2t. The formation of multiple clumps in colliding winds is also a possible explanation (see above). On the other hand, the connection between G1 and the G2+G2t complex is still very speculative, since their orbit does not coincide perfectly and some loss of energy and angular momentum must occur - mainly at pericenter -, due to the interaction of these clumps and the surrounding atmosphere (Pfuhl et al., 2015; McCourt et al., 2015; Madigan et al., 2016). Only additional observations will clarify this point. However, in chapter 7, we provided a different scenario, showing that G2 and G2t could be produced by a relatively high velocity outflow.

The state-of-the-art models on G2's nature are all able to reproduce some of G2's properties, but also show limitations or are unable to explain other observables. Additionally, the pericenter evolution of G2 in simulations for the diffuse cloud scenario (Schartmann et al., 2012; Anninos et al., 2012; Schartmann et al., 2015) and in our simulations look very similar and the comparison to mock PV diagrams (see chapter 6 and Schartmann et al., 2015) show that both models might be reconciled with observations. Hence, no final conclusion can be drawn, yet. The smoking gun for understanding whether a source is embedded in G2 could come in the next 5-10 years, when a decoupling between it and the previously outflowing gas might happen after pericenter, due to the increased cross section of the latter. At that point, the hydrodynamical drag force of the accretion flow would act on G2, but not on its central source, leading to the decoupling.

8.4 Outlook

Many physical aspects of our model can still be investigated and further improvements of the current simulations can be carried out. For example, the too high number of poorly constrained parameters forced us to test only one specific density and temperature distributions for the accretion flow surrounding G2 (see Eq. 2.7 and 2.8). However, both the normalization and the slope of the density and temperature profiles of G2's environment might be slightly different and have an effect on the results. For example, the slope of the density profile β is nowadays still uncertain and theoretical predictions fix a range of possible values of [-3/2;-1/2]. In particular, $\beta = -3/2$ roughly describes Bondi and some ADAF solutions (see, e.g., Narayan et al., 1995); $\beta = -1$ is motivated by simulations (e.g., McKinney et al., 2012; Narayan et al., 2012c) and by some RIAF modelling of the observations (e.g., Yuan et al., 2003); $\beta = -1/2$ is predicted by CDAF models (Quataert & Gruzinov, 2000) and by some modelling of recent X-ray observations (Wang et al., 2013).

A set of simulations can allow to check how significantly the current best parameters are responding to variations of density and temperature of the surrounding medium and to shed light on the properties of the accretion flow. Such study might be particularly interesting, considering that the properties of the accretion flow are very poorly constrained at distances from SgrA* of the order of G2's pericenter. A further step would be implementing a "live" atmosphere that is evolving during the simulation. The current profiles are convectively unstable and need to be reset at every timestep to keep the result under control (see Sec. 5.1). However, accretion flows have, by definition, some inflow motion towards the central SMBH, and they might have some rotation due to non-zero angular momentum. This might certainly have an effect on G2's evolution, particularly around its pericenter passage (as shown by McCourt & Madigan, 2016; Madigan et al., 2016)[1]. Furthermore, magnetic fields in our region of interest might be dynamically important (see Sec. 1.1.4) and play an important role in G2's evolution (Shcherbakov, 2014; McCourt et al., 2015). The major problem, in this case, is that the geometry of the magnetic field around and inside G2 might be extremely complex, thus introducing a further high degree of parametrization in any model involving it. A more realistic modelling of G2's emission properties might, instead, be produced by coupling PLUTO to an external code/module performing detailed radiative transfer, either - and ideally - during the simulation or in post-processing. Biconical outflows could also be tested.

In section 4.1, we also showed how different the structure of winds in the Galactic Center can be, compared to that of winds interacting with a typical interstellar medium (see also Christie et al., 2016). The study of winds from the S-stars by means of hydrodynamical simulations has never been attempted, until the recent study by Lützgendorf et al. (2016). Our setup can be easily adapted to study the evolution of S-stars. A first work could focus, again, on the properties of the accretion flow at around 1000 R_S from SgrA*. Nayakshin (2005) and Giannios & Sironi (2013) have pointed out that X-ray emission is expected to be produced by S2's wind interacting with the accretion flow, at pericenter passage. According to their analytical estimates, the X-ray luminosity is going to significantly depend on the density of the accretion flow and specifically on the slope of its radial profile β. Similar findings were also recently obtained by Ginsburg et al. (2016), Crumley & Kumar (2013) and Zajaček et al. (2016) for radio frequencies. Interestingly, Genzel et al. (2003b) and Gillessen et al. (2009a) showed that S2's luminosity in K_s and L' bands might have increased during its last pericenter passage in year 2002. As we already clarified for G2's case, analytical estimates need several simplifications and they are often unable to capture the complexity of this problem. A more accurate modeling of the interaction between S2's wind and the external accretion flow can be performed by our setup. Such a study might even be more effective than for the equivalent G2's case mentioned before, since:

- S2 is certainly a star, while G2's nature is still a matter of debate;
- S2's orbit is known with very high precision, due to the long monitoring of the object;

[1]However, a possible intermediate and simpler solution might be giving a non-zero velocity field to the idealized atmosphere.

- as mentioned in Sec. 1.2.2, Martins et al. (2008) have performed a dedicated study of the spectrum of S2, that allowed a reliable derivation of its wind parameters, while these are free parameters in the case of G2.

Furthermore, S2 has an orbital period that is 25 times smaller than that of G2, significantly reducing the computational cost needed to follow a full orbit of the object. A detailed post-processing of such a simulation would provide a much more realistic prediction - compared to the previously mentioned analytical studies. The next S2's pericenter passage will occur in early 2018. Hence, this study can help to plan future observational campaigns, which will allow to discriminate between different models for the accretion flow.

A simulation of the full S-star cluster can also be performed in the same manner. As mentioned in Sec. 1.3.2, estimates seem to indicate a continuous and surprising decrease (of up to 3 orders of magnitude) of the accretion rate from the outer to the inner rims of the S-star cluster. Here, feedback from the S-star cluster itself might play a crucial role in quenching the accretion and perhaps even drive outflows or, conversely, in feeding SgrA* (for the latter case, see, e.g., Loeb, 2004). Interestingly, the number of discovered S-stars is roughly 100 (and more will probably be discovered in the next years). Martins et al. (2008) estimated a mass-loss rate for S2 of $\lesssim 3 \times 10^{-7} M_{\odot}$ yr^{-1}. The wind parameters for each S-star are currently not known, but even assuming an average mass-loss rate for each S-star of one order of magnitude smaller (i.e., $3 \times 10^{-8} M_{\odot}$ yr^{-1}), the total mass-outflow rate for the whole cluster turns out to be $\approx 3 \times 10^{-6} M_{\odot}$ yr^{-1}, which is comparable with the previously acknowledged estimates of the accretion rate generated by the more massive O/WR stars in the outer disk (see Sec. 1.3.2). Of course, such a crude estimate (a similar one can be found in Yusef-Zadeh et al., 2016) tells nothing about the (thermo)dynamical properties of the mass injected by the S-stars, but it shows that the mass-injection rate inside the Bondi radius is significant enough to be worth additional study. As already mentioned, Lützgendorf et al. (2016) already performed a similar simulation of the stellar winds from 27 S-stars on their observed orbits, using SPH techniques. However, SPH simulations have several well-known caveats. SPH produces artificial clumping of the gas (e.g., Hobbs et al., 2013). Due to its high numerical viscosity, it prevents hydrodynamical mixing, particularly in the presence of strong thermodynamic gradients (as expected for both, the stellar winds' structure and the hot gas bubble in the Galactic Center) and it suppresses the proper development of hydrodynamical instabilities which are the origin of turbulence, expected to play an important role in the Galactic Center gas component (e.g., Burkert et al., 2012). Additionally, - being based on particles - these SPH simulations did not have the resolution for a proper temporal and spatial sampling of the mass-injection for very small wind mass-loss rates, as in the case of the one derived for S2. This alone justifies the need of a complementary study, using a grid AMR approach. Finally, the orbits of more than 40 S-stars are currently known and new detections and more precise orbital derivation are expected, thanks to the new VLTI NIR instrument GRAVITY (see Sec. 1.3.1). A more complete sample of S-stars could then be used. This study would allow us to find answers to the following open questions:

- **What is the thermodynamical state of the gas in the inner 10^5 R_S of the**

Milky Way? How much of the gas injected by the winds from the S-stars is in a hot ($T > 10^6$ K) state and how much is instead colder and denser ($T < 10^6$ K)? What is the distribution and the dynamical state of such a cold phase? Is the cold gas structured in sheets, filaments, clumps? Can the cooling and collision of the S-stars' winds eventually form G2-like clumps?

- **How are winds from the S-star cluster affecting the accretion onto SgrA*?** Are they adding mass to (and/or remove angular momentum from) the accretion flow from larger radii (positive feedback)? Are they preventing part of this material from getting close to the SMBH (negative feedback)? Or are they having both a positive and negative feedback? Does the complex wind interaction lead to a global equilibrium state or to a periodically changing or even chaotic dynamical evolution of the gas in the Galactic Center and of the accretion onto the SMBH? Can the S-star winds trigger outflows and are these significant enough to affect the large scale galactic environment?

- **How do the S-stars' winds affect the orbit and evolution of G2-like clumps?** How long can these clumps travel on the same ballistic orbit, when winds form the S-stars are considered? Can the interaction with one or more stellar wind explain the different orbits of G1 and G2, if these two clumps have a common origin?

Chapter 9

Summary

The work presented in this dissertation focuses on a "compact source" scenario for the cloud G2.

G2 has been discovered by Gillessen et al. (2012) at few thousands Schwarzschild radii from the supermassive black hole (SMBH) in the center of our Galaxy (often named SgrA*), in a very crowded environment populated by many young stars and by a highly multiphase interstellar medium (see Chapter 1). The cloud shows a compact dust emission and a gaseous component that has instead shown increasing spatial extent and a brodening in the velocity space. G2 has been approaching and passing its pericenter in year 2014 and its position-velocity diagrams are probably reflecting its stretching by the tidal field of SgrA* (see Sec. 2.1). The object is also connected to further gas following it on the same orbit (G2t) and perhaps to a similar precursor (G1) that has passed pericenter roughly 13 years before G2.

Much effort has been put in understanding the nature, origin and evolution of G2, but the community is still divided into two main interpretations: G2 could be a diffuse cloud or it could be related to a central compact object (see Sec. 2.2). The latter scenario has led to many models involving an outflow from a central source, moving on G2's observed orbit.

Though based on previous ideas, our study represents the first attempt in trying to capture the evolution of such an outflow and its interaction with the surrounding accretion flow onto SgrA*, by means of hydrodynamic simulations. Although numerical hydrodynamics come with a certain number of caveats (see, for example, the discussion in Sec. 8.1) and technical issues, they allow to include several non-linear processes involved in G2's evolution and to perform detailed comparison with observations that are often not possible through analytical estimates. For these simulations we used the grid code PLUTO, described in Mignone et al. (2007) and Mignone et al. (2012) and, partially, in Chapter 3.

A first study was conducted with 1D simulations in spherical coordinates (see Sec. 4.1). This work allowed us to understand that the structure of outflows interacting with high pressure external media - such as the hot accretion flow onto SgrA*, surrounding G2 - is very different from that of stellar winds expanding in a typical interstellar medium. The former are extremely confined by the ambient pressure and their shocked part is forming

a very thin, dense shell that can cool very efficiently, while the latter usually get shocked in large bubbles of hot plasma.

Successive 2D simulations in cylindrical coordinates (see Chapter 5) allowed us to include additional physics, such as the motion of the source on G2's orbit and the gravitational field of the SMBH. Compared to the previous 1D simulations, this work showed that the evolution of G2 along its orbit is affected by many combined effects. For example, the dense shocked material is highly Rayleigh-Taylor unstable, hence having a very filamentary distribution. These filaments are stripped by the ram pressure of the external atmosphere and tend to form dense tails, trailing the outflow. As in the case of simulations for the diffuse cloud scenario (Schartmann et al., 2012; Anninos et al., 2012; Schartmann et al., 2015), close to pericenter G2 is "squeezed" by the tidal force of SgrA* and becomes a long and thin "spaghetto". A first preliminary comparison to the observed Brγ luminosity and to the extension in the position-velocity space showed that the needed outflow has to have a relatively high mass-loss rate ($\dot{M}_\mathrm{w} \approx 10^{-7} \mathrm{M}_\odot\ \mathrm{yr}^{-1}$) and low velocity ($v_\mathrm{w} = 50\ \mathrm{km\,s}^{-1}$).

The last step consisted in moving to 3D Cartesian coordinates, with the help of PLUTO's AMR implementation. These further simulations allowed to actually put G2 on the observed Keplerian elliptical orbit and to actually simulate the pericenter passage of G2 (which was not possible with 2D cylindrical coordinates). These also allowed the construction of more realistic mock PV diagrams, that were directly compared with the observed ones obtained by (Gillessen et al., 2012, 2013a,b). Such comparison confirmed the need of a massive outflow (though it revised the best matching mass-loss rate to $\dot{M}_\mathrm{w} \approx 5 \times 10^{-7} \mathrm{M}_\odot\ \mathrm{yr}^{-1}$) and showed that a slow outflow (with, again, $v_\mathrm{w} = 50\ \mathrm{km\,s}^{-1}$) could match G2's properties (see Chapter 6), while a fast outflow ($v_\mathrm{w} = 400\ \mathrm{km\,s}^{-1}$) could maybe explain the connection between G2 and its tail G2t. 3D simulations also showed that the appearence of such an outflow in the PV diagrams is strongly dependent on how much of its unperturbed region is actually emitting.

From our parameter studies, we infer that a possible source for G2 is a young stellar object, like a T Tauri star (as previously suggested by Scoville & Burkert, 2013, see Sec. 8.2). This could also explain the compactness of G2's dust component, if this is associated with such a dusty source.

Although our model is able to account for many of G2's properties, the complementary study by Schartmann et al. (2015) for the diffuse cloud scenario is, in many respects, as effective and the degeneracy between the two possible scenarios can not be removed, yet (see Sec. 8.3). Further observations are needed, but our 3D simulations show that in 5-10 years a decoupling between the central source and the previously emitted material should occur and a new G2 should reform around the dusty one, later on. This might finally allow us to distinguish between these two main hypotheses.

Bibliography

Abarca, D., Sądowski, A., & Sironi, L. 2014, MNRAS, 440, 1125

Abbott, B. P., Abbott, R., Abbott, T. D., et al. 2016a, Physical Review Letters, 116, 241103

—. 2016b, Physical Review Letters, 116, 061102

Alig, C., Burkert, A., Johansson, P. H., & Schartmann, M. 2011, MNRAS, 412, 469

Alig, C., Schartmann, M., Burkert, A., & Dolag, K. 2013, ArXiv e-prints, arXiv:1305.2953

Anninos, P., Fragile, P. C., Wilson, J., & Murray, S. D. 2012, ApJ, 759, 132

Baganoff, F. K., Maeda, Y., Morris, M., et al. 2003, ApJ, 591, 891

Ball, D., Özel, F., Psaltis, D., & Chan, C.-k. 2016, ApJ, 826, 77

Ballone, A., Schartmann, M., Burkert, A., et al. 2013, ApJ, 776, 13

—. 2016, ApJ, 819, L28

Banda-Barragán, W. E., Parkin, E. R., Federrath, C., Crocker, R. M., & Bicknell, G. V. 2016, MNRAS, 455, 1309

Baranov, V. B., Krasnobaev, K. V., & Kulikovskii, A. G. 1971, Soviet Physics Doklady, 15, 791

Bartko, H., Martins, F., Fritz, T. K., et al. 2009, ApJ, 697, 1741

Bartko, H., Martins, F., Trippe, S., et al. 2010, ApJ, 708, 834

Bartos, I., Haiman, Z., Kocsis, B., & Márka, S. 2013, Physical Review Letters, 110, 221102

Bicknell, G. V., & Li, J. 2001, PASA, 18, 431

Blandford, R. D., & Begelman, M. C. 1999, MNRAS, 303, L1

Blandford, R. D., & Rees, M. J. 1974, MNRAS, 169, 395

Boehle, A., Ghez, A. M., Schödel, R., et al. 2016, ArXiv e-prints, arXiv:1607.05726

Böker, T., Laine, S., van der Marel, R. P., et al. 2002, AJ, 123, 1389

Bonnell, I. A., & Rice, W. K. M. 2008, Science, 321, 1060

Borkar, A., Eckart, A., Straubmeier, C., et al. 2016, MNRAS, 458, 2336

Bower, G. C., Wright, M. C. H., Falcke, H., & Backer, D. C. 2003, ApJ, 588, 331

Bower, G. C., Markoff, S., Dexter, J., et al. 2015, ApJ, 802, 69

Bozza, V., & Mancini, L. 2009, ApJ, 696, 701

Brighenti, F., & D'Ercole, A. 1995, MNRAS, 273, 443

Broderick, A. E., & Loeb, A. 2005, MNRAS, 363, 353

Broderick, A. E., Loeb, A., & Narayan, R. 2009, ApJ, 701, 1357

Broderick, A. E., & Narayan, R. 2006, ApJ, 638, L21

Burkert, A., Schartmann, M., Alig, C., et al. 2012, ApJ, 750, 58

Calderón, D., Ballone, A., Cuadra, J., et al. 2016, MNRAS, 455, 4388

Chan, C.-k., Psaltis, D., Özel, F., et al. 2015a, ApJ, 812, 103

Chan, C.-K., Psaltis, D., Özel, F., Narayan, R., & Saḍowski, A. 2015b, ApJ, 799, 1

Chandler, C. J., & Sjouwerman, L. O. 2014, The Astronomer's Telegram, 6247, 1

Chandra, M., Gammie, C. F., Foucart, F., & Quataert, E. 2015, ApJ, 810, 162

Charney, J. G., Fjörtoft, R., & von Neumann, J. 1950, Tellus, 2, 237

Christie, I. M., Petropoulou, M., Mimica, P., & Giannios, D. 2016, MNRAS, arXiv:1601.07432

Christopher, M. H., Scoville, N. Z., Stolovy, S. R., & Yun, M. S. 2005, ApJ, 622, 346

Clavel, M., Terrier, R., Goldwurm, A., et al. 2013, A&A, 558, A32

Clénet, Y., Rouan, D., Gratadour, D., et al. 2005, A&A, 439, L9

—. 2004a, å, 424, L21

Clénet, Y., Rouan, D., Gendron, E., et al. 2004b, A&A, 417, L15

Coker, R. F., & Melia, F. 1997, ApJ, 488, L149

Cooper, J. L., Bicknell, G. V., Sutherland, R. S., & Bland-Hawthorn, J. 2009, ApJ, 703, 330

Côté, P., Piatek, S., Ferrarese, L., et al. 2006, ApJS, 165, 57

Courant, R., Friedrichs, K., & Lewy, H. 1967, IBM Journal of Research and Development, 11, 215

Cowie, L. L., & McKee, C. F. 1977, ApJ, 211, 135

Cox, N. L. J., Kerschbaum, F., van Marle, A.-J., et al. 2012, A&A, 537, A35

Crank, J., Nicolson, P., & Hartree, D. R. 1947, Proceedings of the Cambridge Philosophical Society, 43, 50

Croton, D. J., Springel, V., White, S. D. M., et al. 2006, MNRAS, 365, 11

Crumley, P., & Kumar, P. 2013, MNRAS, 436, 1955

Cuadra, J., Nayakshin, S., & Martins, F. 2008, MNRAS, 383, 458

Cuadra, J., Nayakshin, S., Springel, V., & Di Matteo, T. 2006, MNRAS, 366, 358

Cuadra, J., Nayakshin, S., & Sunyaev, R. 2003, A&A, 411, 405

D'Antona, F., & Mazzitelli, I. 1994, ApJS, 90, 467

Davidson, J. A., Werner, M. W., Wu, X., et al. 1992, ApJ, 387, 189

De Colle, F., Raga, A. C., Contreras-Torres, F. F., & Toledo-Roy, J. C. 2014, ApJ, 789, L33

de la Fuente Marcos, R., & de la Fuente Marcos, C. 2013, MNRAS, 435, L19

Dexter, J. 2011, Radiative Models of Sagittarius A* and M87 from Relativistic MHD Simulations. Dissertation, University of Washington, Washington. http://hdl.handle.net/1773/17085

Dexter, J., Agol, E., Fragile, P. C., & McKinney, J. C. 2010, ApJ, 717, 1092

Dibi, S., Drappeau, S., Fragile, P. C., Markoff, S., & Dexter, J. 2012, MNRAS, 426, 1928

Dibi, S., Markoff, S., Belmont, R., et al. 2016, MNRAS, 461, 552

Do, T., Ghez, A. M., Morris, M. R., et al. 2009, ApJ, 691, 1021

Do, T., Lu, J. R., Ghez, A. M., et al. 2013, ApJ, 764, 154

Dodds-Eden, K., Sharma, P., Quataert, E., et al. 2010, ApJ, 725, 450

Dodds-Eden, K., Gillessen, S., Fritz, T. K., et al. 2011, ApJ, 728, 37

Doeleman, S. 2010, in 10th European VLBI Network Symposium and EVN Users Meeting: VLBI and the New Generation of Radio Arrays, 53

Done, C., Gierliński, M., & Kubota, A. 2007, A&A Rev., 15, 1

Drappeau, S., Dibi, S., Dexter, J., Markoff, S., & Fragile, P. C. 2013, MNRAS, 431, 2872

Eatough, R. P., Falcke, H., Karuppusamy, R., et al. 2013, Nature, 501, 391

Eckart, A., & Genzel, R. 1997, MNRAS, 284, 576

Eckart, A., Schödel, R., Meyer, L., et al. 2006, A&A, 455, 1

Eckart, A., Mužić, K., Yazici, S., et al. 2013, A&A, 551, A18

Edwards, S., Fischer, W., Hillenbrand, L., & Kwan, J. 2006, ApJ, 646, 319

Eisenhauer, F., Genzel, R., Alexander, T., et al. 2005, ApJ, 628, 246

Ekers, R. D., van Gorkom, J. H., Schwarz, U. J., & Goss, W. M. 1983, A&A, 122, 143

Falcke, H., Körding, E., & Markoff, S. 2004, A&A, 414, 895

Falcke, H., & Markoff, S. 2000, A&A, 362, 113

Falcke, H., & Melia, F. 1997, ApJ, 479, 740

Falle, S. A. E. G. 1975, A&A, 43, 323

Ferland, G. J. 1980, PASP, 92, 596

Ferrarese, L., & Merritt, D. 2000, ApJ, 539, L9

Ferrière, K. 2009, A&A, 505, 1183

Fierlinger, K. M., Burkert, A., Ntormousi, E., et al. 2016, MNRAS, 456, 710

Fragile, P. C., Anninos, P., & Murray, S. D. 2014, in IAU Symposium, Vol. 303, The Galactic Center: Feeding and Feedback in a Normal Galactic Nucleus, ed. L. O. Sjouwerman, C. C. Lang, & J. Ott, 318–319

Fujii, M., Iwasawa, M., Funato, Y., & Makino, J. 2008, ApJ, 686, 1082

—. 2010, ApJ, 716, L80

Gatley, I., Jones, T. J., Hyland, A. R., et al. 1986, MNRAS, 222, 299

Gebhardt, K., Bender, R., Bower, G., et al. 2000, ApJ, 539, L13

Genzel, R., Eckart, A., Ott, T., & Eisenhauer, F. 1997, MNRAS, 291, 219

Genzel, R., Eisenhauer, F., & Gillessen, S. 2010, Reviews of Modern Physics, 82, 3121

Genzel, R., Pichon, C., Eckart, A., Gerhard, O. E., & Ott, T. 2000, MNRAS, 317, 348

Genzel, R., Schödel, R., Ott, T., et al. 2003a, Nature, 425, 934

Genzel, R., Thatte, N., Krabbe, A., Kroker, H., & Tacconi-Garman, L. E. 1996, ApJ, 472, 153

Genzel, R., Schödel, R., Ott, T., et al. 2003b, ApJ, 594, 812

Gerhard, O. 2001, ApJ, 546, L39

Gezari, D. Y., Shu, P., Lamb, G., et al. 1985, ApJ, 299, 1007

Ghez, A. M., Klein, B. L., Morris, M., & Becklin, E. E. 1998, ApJ, 509, 678

Ghez, A. M., Salim, S., Hornstein, S. D., et al. 2005a, ApJ, 620, 744

Ghez, A. M., Duchêne, G., Matthews, K., et al. 2003, ApJ, 586, L127

Ghez, A. M., Wright, S. A., Matthews, K., et al. 2004, ApJ, 601, L159

Ghez, A. M., Hornstein, S. D., Lu, J. R., et al. 2005b, ApJ, 635, 1087

Ghez, A. M., Salim, S., Weinberg, N. N., et al. 2008, ApJ, 689, 1044

Giannios, D., & Sironi, L. 2013, MNRAS, 433, L25

Gillessen, S., Eisenhauer, F., Trippe, S., et al. 2009a, ApJ, 692, 1075

—. 2009b, ApJ, 692, 1075

Gillessen, S., Genzel, R., Fritz, T. K., et al. 2012, Nature, 481, 51

—. 2013a, ApJ, 763, 78

—. 2013b, ApJ, 774, 44

Ginsburg, I., Wang, X., Loeb, A., & Cohen, O. 2016, MNRAS, 455, L21

Goicoechea, J. R., Etxaluze, M., Cernicharo, J., et al. 2013, ApJ, 769, L13

Graham, A. W., & Spitler, L. R. 2009, MNRAS, 397, 2148

Guesten, R., Genzel, R., Wright, M. C. H., et al. 1987, ApJ, 318, 124

Guillochon, J., Loeb, A., MacLeod, M., & Ramirez-Ruiz, E. 2014a, ApJ, 786, L12

Guillochon, J., Manukian, H., & Ramirez-Ruiz, E. 2014b, ApJ, 783, 23

Günther, H. M., Matt, S. P., & Li, Z.-Y. 2009a, A&A, 493, 579

—. 2009b, A&A, 493, 579

Haggard, D., Baganoff, F. K., Rea, N., et al. 2014, The Astronomer's Telegram, 6242, 1

Haller, J. W., Rieke, M. J., Rieke, G. H., et al. 1996, ApJ, 456, 194

Hamann, F., & Ferland, G. 1999, ARA&A, 37, 487

Hamers, A. S., & Portegies Zwart, S. F. 2015, MNRAS, 446, 710

Hartigan, P., Edwards, S., & Ghandour, L. 1995, ApJ, 452, 736

Hobbs, A., & Nayakshin, S. 2009, MNRAS, 394, 191

Hobbs, A., Read, J., Power, C., & Cole, D. 2013, MNRAS, 434, 1849

Irons, W. T., Lacy, J. H., & Richter, M. J. 2012, ApJ, 755, 90

Jackson, J. M., Geis, N., Genzel, R., et al. 1993, ApJ, 402, 173

Kerr, R. P. 1963, Physical Review Letters, 11, 237

Kim, S. S., Figer, D. F., & Morris, M. 2004, ApJ, 607, L123

King, A. 2003, ApJ, 596, L27

Koo, B.-C., & McKee, C. F. 1992, ApJ, 388, 103

Kormendy, J., & Ho, L. C. 2013, ARA&A, 51, 511

Kostić, U., Čadež, A., Calvani, M., & Gomboc, A. 2009, A&A, 496, 307

Kozai, Y. 1962, AJ, 67, 591

Krabbe, A., Genzel, R., Eckart, A., et al. 1995, ApJ, 447, L95

Kunneriath, D., Eckart, A., Vogel, S. N., et al. 2012, A&A, 538, A127

Kwak, K., Henley, D. B., & Shelton, R. L. 2011, ApJ, 739, 30

Lacy, J. H., Townes, C. H., Geballe, T. R., & Hollenbach, D. J. 1980, ApJ, 241, 132

Lacy, J. H., Townes, C. H., & Hollenbach, D. J. 1982, ApJ, 262, 120

Lamers, H. J. G. L. M., & Cassinelli, J. P. 1999, Introduction to Stellar Winds, 452

Laor, A. 2001, ApJ, 553, 677

Lau, R. M., Herter, T. L., Morris, M. R., Becklin, E. E., & Adams, J. D. 2013, ApJ, 775, 37

Levin, Y., & Beloborodov, A. M. 2003, ApJ, 590, L33

Li, Y.-P., Yuan, F., Yuan, Q., et al. 2015, ApJ, 810, 19

Lidov, M. L. 1962, Planet. Space Sci., 9, 719

Liu, H. B., Ho, P. T. P., Wright, M. C. H., et al. 2013, ApJ, 770, 44

Liu, H. B., Hsieh, P.-Y., Ho, P. T. P., et al. 2012, ApJ, 756, 195

Lo, K. Y., & Claussen, M. J. 1983, Nature, 306, 647

Loeb, A. 2004, MNRAS, 350, 725

Lu, J. R., Do, T., Ghez, A. M., et al. 2013, ApJ, 764, 155

Lu, J. R., Ghez, A. M., Hornstein, S. D., et al. 2009, ApJ, 690, 1463

Lucas, W. E., Bonnell, I. A., Davies, M. B., & Rice, W. K. M. 2013, MNRAS, 433, 353

Lützgendorf, N., Helm, E. v. d., Pelupessy, F. I., & Portegies Zwart, S. 2016, MNRAS, 456, 3645

Lynden-Bell, D. 1969, Nature, 223, 690

Madigan, A.-M., McCourt, M., & O'Leary, R. 2016, ArXiv e-prints, arXiv:1602.02760

Magorrian, J., Tremaine, S., Richstone, D., et al. 1998, AJ, 115, 2285

Mapelli, M., & Gualandris, A. 2016, in Lecture Notes in Physics, Berlin Springer Verlag, Vol. 905, Lecture Notes in Physics, Berlin Springer Verlag, ed. F. Haardt, V. Gorini, U. Moschella, A. Treves, & M. Colpi, 205

Mapelli, M., Hayfield, T., Mayer, L., & Wadsley, J. 2008, ArXiv e-prints, arXiv:0805.0185

—. 2012, ApJ, 749, 168

Mapelli, M., & Ripamonti, E. 2015, ApJ, 806, 197

Markoff, S., Falcke, H., Yuan, F., & Biermann, P. L. 2001, A&A, 379, L13

Marr, J. M., Wright, M. C. H., & Backer, D. C. 1993, ApJ, 411, 667

Marrone, D. P., Moran, J. M., Zhao, J.-H., & Rao, R. 2006, Journal of Physics Conference Series, 54, 354

Martín, S., Martín-Pintado, J., Montero-Castaño, M., Ho, P. T. P., & Blundell, R. 2012, A&A, 539, A29

Martins, F., Genzel, R., Hillier, D. J., et al. 2007, A&A, 468, 233

Martins, F., Gillessen, S., Eisenhauer, F., et al. 2008, ApJ, 672, L119

Martins, F., Trippe, S., Paumard, T., et al. 2006, ApJ, 649, L103

McCourt, M., & Madigan, A.-M. 2016, MNRAS, 455, 2187

McCourt, M., O'Leary, R. M., Madigan, A.-M., & Quataert, E. 2015, MNRAS, 449, 2

McKinney, J. C., Tchekhovskoy, A., & Blandford, R. D. 2012, MNRAS, 423, 3083

McMillan, S. L. W., & Portegies Zwart, S. F. 2003, ApJ, 596, 314

McNamara, B. R., & Nulsen, P. E. J. 2012, New Journal of Physics, 14, 055023

Melia, F., Liu, S., & Coker, R. 2001, ApJ, 553, 146

Merloni, A., Heinz, S., & di Matteo, T. 2003, MNRAS, 345, 1057

Meyer, D. M.-A., Mackey, J., Langer, N., et al. 2014, MNRAS, 444, 2754

Meyer, F., & Meyer-Hofmeister, E. 2012, A&A, 546, L2

Meyer, L., Ghez, A. M., Schödel, R., et al. 2012, Science, 338, 84

Mezger, P. G., Zylka, R., Salter, C. J., et al. 1989, A&A, 209, 337

Mignone, A., Bodo, G., Massaglia, S., et al. 2007, ApJS, 170, 228

Mignone, A., Zanni, C., Tzeferacos, P., et al. 2012, ApJS, 198, 7

Miralda-Escudé, J. 2012, ApJ, 756, 86

Montero-Castaño, M., Herrnstein, R. M., & Ho, P. T. P. 2009, ApJ, 695, 1477

Montgomery, C., Orchiston, W., & Whittingham, I. 2009, Journal of Astronomical History and Heritage, 12, 90

Morris, M. 2006, Journal of Physics Conference Series, 54, 1

Morris, M., & Serabyn, E. 1996, ARA&A, 34, 645

Morris, M. R. 2014, ArXiv e-prints, arXiv:1406.7859

Mościbrodzka, M., Das, T. K., & Czerny, B. 2006, MNRAS, 370, 219

Mościbrodzka, M., & Falcke, H. 2013, A&A, 559, L3

Mościbrodzka, M., Falcke, H., Shiokawa, H., & Gammie, C. F. 2014, A&A, 570, A7

Mościbrodzka, M., Gammie, C. F., Dolence, J. C., Shiokawa, H., & Leung, P. K. 2009, ApJ, 706, 497

Moser, L., Sánchez-Monge, Á., Eckart, A., et al. 2016, ArXiv e-prints, arXiv:1603.00801

Mossoux, E., Grosso, N., Bushouse, H., et al. 2016, A&A, 589, A116

Muno, M. P., Baganoff, F. K., Bautz, M. W., et al. 2004, ApJ, 613, 326

Murray-Clay, R. A., & Loeb, A. 2012, Nature Communications, 3, doi:10.1038/ncomms2044

Narayan, R., Özel, F., & Sironi, L. 2012a, ApJ, 757, L20

—. 2012b, ApJ, 757, L20

Narayan, R., SĄ dowski, A., Penna, R. F., & Kulkarni, A. K. 2012c, MNRAS, 426, 3241

Narayan, R., Yi, I., & Mahadevan, R. 1995, Nature, 374, 623

Nayakshin, S. 2005, A&A, 429, L33

—. 2006, MNRAS, 372, 143

Nayakshin, S., Cuadra, J., & Springel, V. 2007, MNRAS, 379, 21

Newman, E. T., Couch, E., Chinnapared, K., et al. 1965, Journal of Mathematical Physics, 6, 918

Nowak, M. A., Neilsen, J., Markoff, S. B., et al. 2012, ApJ, 759, 95

Oka, T., Nagai, M., Kamegai, K., & Tanaka, K. 2011, ApJ, 732, 120

Orosz, J. A., McClintock, J. E., Aufdenberg, J. P., et al. 2011, ApJ, 742, 84

Osterbrock, D. E., & Ferland, G. J. 2006, Astrophysics of gaseous nebulae and active galactic nuclei

Özel, F., Psaltis, D., & Narayan, R. 2000, ApJ, 541, 234

Parker, E. N. 1963, Interplanetary dynamical processes.

Paumard, T., Maillard, J.-P., & Morris, M. 2004, A&A, 426, 81

Paumard, T., Genzel, R., Martins, F., et al. 2006, ApJ, 643, 1011

Peng, C. Y. 2007, ApJ, 671, 1098

Perez, K., Hailey, C. J., Bauer, F. E., et al. 2015, Nature, 520, 646

Peterson, B. M. 2014, Space Science Reviews, 183, 253

Pfuhl, O., Alexander, T., Gillessen, S., et al. 2014, ApJ, 782, 101

Pfuhl, O., Gillessen, S., Eisenhauer, F., et al. 2015, ApJ, 798, 111

Phifer, K., Do, T., Meyer, L., et al. 2013, ArXiv e-prints, arXiv:1304.5280

Pittard, J. M., Dyson, J. E., Falle, S. A. E. G., & Hartquist, T. W. 2005, MNRAS, 361, 1077

Ponti, G., Terrier, R., Goldwurm, A., Belanger, G., & Trap, G. 2010, ApJ, 714, 732

Ponti, G., De Marco, B., Morris, M. R., et al. 2015, MNRAS, 454, 1525

Prodan, S., Antonini, F., & Perets, H. B. 2015, ApJ, 799, 118

Quataert, E. 2004, ApJ, 613, 322

Quataert, E., & Gruzinov, A. 2000, ApJ, 545, 842

Quirk, J. J. 1994, International Journal for Numerical Methods in Fluids, 18, 555

Reissner, H. 1916, Annalen der Physik, 355, 106

Requena-Torres, M. A., Güsten, R., Weiß, A., et al. 2012, A&A, 542, L21

Ressler, S. M., Tchekhovskoy, A., Quataert, E., Chandra, M., & Gammie, C. F. 2015, MNRAS, 454, 1848

Revnivtsev, M. G., Churazov, E. M., Sazonov, S. Y., et al. 2004, A&A, 425, L49

Roberts, D. A., Yusef-Zadeh, F., & Goss, W. M. 1996, ApJ, 459, 627

Rockefeller, G., Fryer, C. L., Melia, F., & Warren, M. S. 2004, ApJ, 604, 662

Różańska, A., Czerny, B., Kunneriath, D., et al. 2014, MNRAS, 445, 4385

Rozyczka, M. 1985, A&A, 143, 59

Russell, C. M. P., Wang, Q. D., & Cuadra, J. 2016, ArXiv e-prints, arXiv:1607.01562

Saitoh, T. R., Makino, J., Asaki, Y., et al. 2014, PASJ, 66, 1

Salpeter, E. E. 1964, ApJ, 140, 796

Sanchez-Bermudez, J., Schödel, R., Alberdi, A., et al. 2014, A&A, 567, A21

Sądowski, A., Narayan, R., Sironi, L., & Özel, F. 2013a, MNRAS, 433, 2165

Sądowski, A., Sironi, L., Abarca, D., et al. 2013b, MNRAS, 432, 478

Schartmann, M., Burkert, A., Alig, C., et al. 2012, ApJ, 755, 155

Schartmann, M., Ballone, A., Burkert, A., et al. 2015, ApJ, 811, 155

Schödel, R., Ott, T., Genzel, R., et al. 2003, ApJ, 596, 1015

Schwarzschild, K. 1916, Sitzungsberichte der Königlich Preußischen Akademie der Wissenschaften (Berlin), 1916, Seite 189-196

Scoville, N., & Burkert, A. 2013, ApJ, 768, 108

Serabyn, E., & Lacy, J. H. 1985, ApJ, 293, 445

Shakura, N. I., & Sunyaev, R. A. 1973, A&A, 24, 337

Shcherbakov, R. V. 2014, ApJ, 783, 31

Shukla, H., Yun, M. S., & Scoville, N. Z. 2004, ApJ, 616, 231

Silk, J., & Rees, M. J. 1998, A&A, 331, L1

Stephan, A. P., Naoz, S., Ghez, A. M., et al. 2016, MNRAS, 460, 3494

Sutherland, R. S., & Dopita, M. A. 1993, ApJS, 88, 253

Tagger, M., & Melia, F. 2006, ApJ, 636, L33

Tanner, A., Ghez, A. M., Morris, M. R., & Christou, J. C. 2005, ApJ, 624, 742

Tanner, A., Figer, D. F., Najarro, F., et al. 2006, ApJ, 641, 891

Teyssier, R. 2015, ARA&A, 53, 325

Toro, E. F. 1997, Riemann solvers and numerical methods for fluid dynamics : a practical introduction (Berlin, New York: Springer)

Trani, A. A., Mapelli, M., Bressan, A., et al. 2016, ApJ, 818, 29

Trap, G., Goldwurm, A., Dodds-Eden, K., et al. 2011, A&A, 528, A140

Tsuboi, M., Kitamura, Y., Miyoshi, M., et al. 2016, PASJ, 68, L7

Valencia-S., M., Eckart, A., Zajaček, M., et al. 2015, ApJ, 800, 125

van Marle, A. J., Langer, N., Achterberg, A., & García-Segura, G. 2006, A&A, 460, 105

Vieser, W., & Hensler, G. 2007, A&A, 472, 141

Vishniac, E. T. 1994, ApJ, 428, 186

Vollmer, B., & Duschl, W. J. 2002, A&A, 388, 128

Wang, Q. D., Nowak, M. A., Markoff, S. B., et al. 2013, Science, 341, 981

Weaver, R., McCray, R., Castor, J., Shapiro, P., & Moore, R. 1977, ApJ, 218, 377

White, M. C., McGregor, P. J., Bicknell, G. V., Salmeron, R., & Beck, T. L. 2014, MNRAS, 441, 1681

White, R. J., & Hillenbrand, L. A. 2004, ApJ, 616, 998

Whitelock, P. A., Boyer, M., Höfner, S., Wittkowski, M., & Zijlstra, A. A. 2016, ArXiv e-prints, arXiv:1609.07954

Wilkin, F. P. 1996, ApJ, 459, L31

Witzel, G., Eckart, A., Bremer, M., et al. 2012, ApJS, 203, 18

Witzel, G., Ghez, A. M., Morris, M. R., et al. 2014, ApJ, 796, L8

Wollman, E. R., Geballe, T. R., Lacy, J. H., Townes, C. H., & Rank, D. M. 1977, ApJ, 218, L103

Xu, Y.-D., Narayan, R., Quataert, E., Yuan, F., & Baganoff, F. K. 2006, ApJ, 640, 319

Yelda, S., Ghez, A. M., Lu, J. R., et al. 2014, ApJ, 783, 131

Yuan, F., Markoff, S., & Falcke, H. 2002, A&A, 383, 854

Yuan, F., & Narayan, R. 2014, ARA&A, 52, 529

Yuan, F., Quataert, E., & Narayan, R. 2003, ApJ, 598, 301

—. 2004, ApJ, 606, 894

Yuan, Q., & Wang, Q. D. 2016, MNRAS, 456, 1438

Yusef-Zadeh, F., Braatz, J., Wardle, M., & Roberts, D. 2008, ApJ, 683, L147

Yusef-Zadeh, F., Bushouse, H., Schödel, R., et al. 2015, ApJ, 809, 10

Yusef-Zadeh, F., Wardle, M., Bushouse, H., Dowell, C. D., & Roberts, D. A. 2010, ApJ, 724, L9

Yusef-Zadeh, F., Wardle, M., Schödel, R., et al. 2016, ApJ, 819, 60

Yusef-Zadeh, F., Royster, M., Wardle, M., et al. 2013, ApJ, 767, L32

Zajaček, M., Eckart, A., Karas, V., et al. 2016, MNRAS, 455, 1257

Zajaček, M., Karas, V., & Eckart, A. 2014, A&A, 565, A17

Zhang, F., Lu, Y., & Yu, Q. 2015, ApJ, 809, 127

Zhao, J.-H., Blundell, R., Moran, J. M., et al. 2010, ApJ, 723, 1097

Zhao, J.-H., Morris, M. R., Goss, W. M., & An, T. 2009, ApJ, 699, 186

Zubovas, K., Nayakshin, S., & Markoff, S. 2012, MNRAS, 421, 1315

Zucker, S., Alexander, T., Gillessen, S., Eisenhauer, F., & Genzel, R. 2006, ApJ, 639, L21

Acknowledgments

Though his name does not appear in the first pages of this Dissertation, I would first of all like to thank Dr. Marc Schartmann, for continuously and endlessly guiding, supporting and teaching me throughout these years and for his trust, humbleness and friendship.

My second thank obviously goes to my supervisor Prof. Dr. Andreas Burkert: I feel that working with him, particularly at this early stage of my career, has been a privilege. Interacting with him has always been stimulating and inspiring, not only from a scientific point of view.

I also thank the Galactic Center group at MPE, particularly Dr. Stefan Gillessen, for sharing their amazing results and for our collaboration. This work has definitely benefitted from it.

A great thank goes to Prof. Dr. Jorge Cuadra and Diego Calderón Espinoza for our work together, for their friendship and for hosting me in Santiago (and not only there!!!) for a whole month.

Before more personal mentions, I would also thank Prof. Dr. Michela Mapelli for giving me the opportunity to work with her as a postdoc, after this period spent in Munich.

I definitely thank my officemates. Above all, Manuel, who started his PhD with me and always accompanied me in this journey. The "travel" together was a lot of fun and you often managed to enrich it with humanity and optimism. I certainly have to mention Bhaskar for all the discussions, both the serious and the superficial ones. I thank Go and Guang-Xing for many reasons, but especially for bringing us two lovely kids. Many other colleagues have come and go (even through the office) and made my everyday life more interesting and happy: thanks particularly to Fabian, Jaime, Martha, Jiamin, Salvador, Torben, Matias, Simone, Jens, Michela, Fabrizio, Claudio, Michael, Alice, Elena, but many others could be mentioned too. I wish you good luck with everything and I hope to meet you all again, sooner or later.

A special place in my acknowledgments goes to Andrea, Lucrezia, Giulia, Matteo e Simone, my intimate Italian circle. You have been both friends and colleagues (except for Lucrezia...) and I could always find, in you, the chance to share the everyday struggle with work and study, but also to relax, discuss personal matters and enjoy my stay talking, playing, visiting new places, eating good (or not so good) food.

The other special place is occupied by my mediterranean circle Ilias, Lena, Nico, Eva, Jaime (here he is, again!), Sandra, Chryssa, Elina and Thomas, you have been a necessary escape from the previously mentioned everyday struggle and study, with you I got the

chance to meet very good, honest and loyal friends, with whom I shared many special experiences and PARTIES!!! I am looking forward to seeing Dorothea growing up and... maybe other babies coming?

Outside Munich, but definitely necessary for my personal and academic growth, I have to thank Maurizio Proia, since he is the one who inspired me in the choice of my academic path, and my Bachelor's and Master's supervisor Prof. Dr. Fabrizio Brighenti, for teaching me the foundations of my current expertise.

I also thank all the other good friends that I met along the way - before, during and after -, since many of them really participated to my personal growth.

At the end, the greatest thank goes to the most important people in my life, my parents and my grandparents. It's mainly because of you, if I reached this goal in my life and if I have become what I am.